CR-134124

FINAL REPORT
TO
NASA - L.B.JOHNSON SPACECRAFT CENTER
Thermal Technology Branch, Houston, Texas 77058

Contract No. NAS 9-13058

Contract Monitor: C. Scott/E53

CATALYSIS STUDY FOR SPACE SHUTTLE VEHICLE THERMAL PROTECTION SYSTEMS

Principal Investigator: D.E. Rosner
Co-Principal Investigators: W.N. Delgass
P.C. Nordine

Report Prepared by: J. Breen
R. Cibrian
~~W.N. Delgass~~
M.G. Krishnan
~~P.C. Nordine~~
~~D.E. Rosner~~

October 4, 1973
YALE UNIVERSITY
Department of Engineering and Applied Science
Mason Laboratory, New Haven, Connecticut 06520

(NASA-CR-134124) CATALYSIS STUDY FOR SPACE SHUTTLE VEHICLE THERMAL PROTECTION SYSTEMS Final Report (Yale Univ.) 148 p HC $[illegible].50 CSCL 22B

N74-12498

G3/31 Unclas 22760

ABSTRACT

Exploitation of the aerodynamic heating reductions attending the use of Space Shuttle Orbiter vehicle surfaces which are non-catalytic to O-atom and N-atom recombination requires an improved knowledge of the chemical and physical factors governing the corresponding reaction probabilities γ_O and γ_N on these surfaces at elevated temperatures. Described herein are the results of an experimental program including: (i) development of a laboratory flow reactor technique for measuring γ_O and γ_N on candidate materials at surface temperatures, T_w in the nominal range 1000-2000K, (ii) measurements of γ_O and γ_N above 1000K for both the glass coating of a reusable surface insulation (RSI) material and the siliconized surface of a reinforced pyrolyzed plastic (RPP) material intended for leading edge service, (iii) corresponding measurement of the ablation behavior of the coated RPP material at $T_w \leq 2150K$, (iv) X-ray photoelectron spectral studies of the chemical constituents on these surfaces before and after dissociated gas exposure, (v) scanning electron micrograph examination of as-received and reacted specimens, and (vi) development and exploitation of a method of predicting the aerodynamic heating consequences of these $\gamma_O(T_w)$ and $\gamma_N(T_w)$ measurements for critical locations on a radiation cooled Orbiter vehicle. It was concluded that while presently tested materials exhibited considerable high temperature atom recombination activity, the potential for achieving lower γ without sacrificing high emittance exists. γ-reductions would be especially advantageous for regions of the vehicle exposed to appreciable N-atom concentrations.

Catalysis Study for Space Shuttle Vehicle Thermal Protection Systems Materials

TABLE OF CONTENTS

Section Title — Page

FIGURE CAPTIONS 4

1. INTRODUCTION 7

2. FLOW REACTOR γ-EXPERIMENTS 10
    - 2.1 Apparatus and Experimental Techniques 10
        - 2.1.1 Apparatus 10
        - 2.1.2 Experimental Techniques 12
    - 2.2 Data Reduction Procedure 15
        - 2.2.1 Level 1 Inference of γ 16
        - 2.2.2 Level 2 Inference of γ 17
    - 2.3 Atom Recombination Coefficient Results for Quartz Nickel, RSI and RPP 23
        - 2.3.1 Atom Recombination on Quartz 23
        - 2.3.2 Atom Recombination on Nickel 30
        - 2.3.3 Atom Recombination on RPP 32
        - 2.3.4 Atom Recombination on RSI 36

3. MASS LOSS EXPERIMENTS - LEADING EDGE MATERIAL 39
    - 3.1 Technique 40
    - 3.2 Results 42
    - 3.3 Implications 53

4. SURFACE CHARACTERIZATION STUDIES 56
    - 4.1 X-ray Photoelectron Spectroscopy 56
        - 4.1.1 Technique 56
        - 4.1.2 Results and Discussion of XPS Experiments 61
        - 4.1.3 Conclusions and Implications of XPS Experiments 79
    - 4.2 Scanning Electron Microscopy 81
        - 4.2.1 Technique 81
        - 4.2.2 Results of Scanning Electron Microscopy 82
        - 4.2.3 Conclusions and Implications 87

5. AERODYNAMIC HEATING OF HYPERSONIC GLIDE VEHICLES 88
    - 5.1 Method: Predicting Radiation Equilibrium Surface Temperatures for Candidate Thermal Protection System Materials 88
        - 5.1.1 Equilibrium Stagnation State Conditions 94
        - 5.1.2 Thermodynamic and Transport Laws and Data 95
        - 5.1.3 Incomplete O_2 and/or N_2 Dissociation in the Low Density Shock Layer 96
        - 5.1.4 Numerical Methods and Computational Efficiency 101
    - 5.2 Implications of γ-Results 103
    - 5.3 Previously Unconsidered Chemical Events Which Could Modify the Rate of Energy Transfer to the Vehicle Surface 110
        - 5.3.1 Role of Surface-Catalyzed Production of Excited Molecules 111

Section Title | Page

5.3.2 Influence of Bimolecular Exchange Reactions on Energy Transfer to Solids in Dissociated Air 115
5.4 The Disparity between γ Inferred from Duct Reactor Tests and γ Inferred from Arc Jet Tests 121

6. CONCLUSIONS AND RECOMMENDATIONS 123

6.1 Conclusions 123
6.2 Recommendations 127

7. REFERENCES 129

8. NOMENCLATURE 133

APPENDIX 2.2 DETAILS OF DUCT REACTOR DATA REDUCTION PROCEDURE 139

APPENDIX 2.3 ON THE USE OF Al_2O_3 ADDITIONS TO RPP COATINGS 142

APPENDIX 5.1 CONVERSION OF γ_i TO RECOMBINATION RATE CONSTANT ("VELOCITY") 147

ACKNOWLEDGEMENTS

The one year technical effort summarized in this report would not have been possible without the cooperation of the individuals and organizations cited here. It is therefore a pleasure to acknowledge: C. Scott (NASA-LBJ Space Craft Center) for providing background information and data on the Space Shuttle Orbiter aerodynamic heating problem; E. Brosious (Yale University Physics Dept.) for his glassblowing; M.E. Washburn (Norton Co.) for providing calibration samples of silicon nitride and silicon oxynitride; F. Wong (State Univ. New York - Stony Brook, Class of 1974) for his assistance in the aerodynamic heating computations reported in Sections 5.2, 5.3; the Chemistry Department, Yale University for permitting use of the Hewlett-Packard ESCA Spectrometer, on which nearly all of the measurements reported in Section 4 were made and K. Clarke for typing and assistance in assembling our quarterly progress and final reports.

FIGURE CAPTIONS

Fig. No.	Caption
2.1-1	Schematic of duct atom recombination reactor
2.2-1	Computed profiles of atom concentration, pressure and gas temperature in duct atom recombination reactor; N-atom/RPP run; T_w = 1120K
2.3-1	Temperature dependence of O-atom recombination on quartz; Present work
2.3-2	Temperature dependence of N-atom recombination on quartz; Present work
2.3-3	O-atom and N-atom recombination coefficients on the LTV-RPP material; ○, γ_O-values; □, O-atom reaction probability: ◐ γ_N-values; typical experimental conditions for O-atom runs: argon flow:260 cc·atm/min, O_2 flow: 115 cc·atm/min, upstream pressure at room temperature: 1.4 torr; gas flow velocity in Reactor Section II: 2500 cm/sec; typical experimental conditions for N-atom runs: argon flow rate: 250 cc·atm/min, N_2 flow rate: 450 cc·atm/min, upstream pressure at room temperature: 20 torr, gas flow velocity in Reactor Section II: 2700 cm/sec.
2.3-4	O-atom and N-atom recombination coefficients on the RSI coating material. For O-atom data: open symbols are measurements taken while the wall temperature was increasing, closed symbols are measurements taken when the wall temperature was decreasing; ○, measurements on the first cycle; □, measurements on the second cycle △, measurements on the third cycle. Typical experimental conditions for O-atom experiments: argon flow: 390 cc·atm/mi O_2 flow rate: 70 cc·atm/min; upstream pressure at room temperature: 1.6 torr; gas flow velocity in reactor Section II: 2350 cm/sec. Typical experimental conditions for N-atom data: argon flow rate: 302 cc·atm/min, N_2 flow rate: 305 cc·atm/min; upstream pressure at room temperature: 1.6 torr; gas flow velocity in reactor Section II: 2600 cm/sec
3.1-1	Schematic of transonic atom flow reactor used for RPP mass loss experiments

FIGURE CAPTIONS (continued)

Fig. No	Caption
3.2-1	RPP coating recession rate; circles: $p_{O_2} = 0.012$ torr; Squares: $p_{O_2} = 0.055$ torr. Open symbols denote 25% dissociated gas mixture: filled symbols denote molecular reactants; dashed line is from Rosner and Allendorf (1970a) for the β-SiC/O reaction at $p_O = 10^{-2}$ torr.
3.2-2	RPP coating recession rate in a dissociated O_2/N_2 mixture. Dashed line is rate in absence of nitrogen
3.2-3	Dependence of oxidation probability of silicon carbide RPP coating on reciprocal temperature. ▲, ■ = 0.11 torr; △, □ = 0.025 torr; ■, □ = O_2; ▲, △ = O_2/O
3.2-4	RPP coating recession rates in stagnation arc jet tests. ○ "Phase 1" coating; + = "Phase 2" coating.
3.2-5	Photomicrographs of RPP specimens after reaction with oxygen. a : T = 1618K; b : T = 1826K; c : T = 2013K; d = specimen before reaction
3.3-1	Vapor-condensed phase equilibrium pressures in the SiC-SiO_2-O_2 system.
4.1-1	Schematic of the X-ray photo-electron spectroscopy experiment and data analysis.
4.1-2	Inelastic mean free path of emitted photo-electrons for various sample materials
4.1-3	XPS spectra of RPP coating of (a) γ-sample after exposure to <u>N</u> + <u>O</u> atoms at 1673K and (b) mass loss sample after exposure to <u>O</u> atoms at 1722K.
4.2-1	RSI (Lockheed 0042) heated to 1100K in oxygen environment
4.2-2	RSI (Lockheed 0042). Plasma arc jet tested at 1260°K. (Specimen #7, Table 4.1-2)
4.2-3	RPP fresh coating
4.2-4	RPP coating after exposure to oxygen molecules at 1618°K. The top left is the product film
4.2-5	Photomicrograph of RPP coating after exposure to <u>O</u> atoms at 1720°K. Note the solidified molten layers at the sides of the sample
4.2-6	RPP coating after exposure to <u>O</u> atoms at 1830°K. Note the spherical nature of the particles

FIGURE CAPTIONS(continued)

Fig. No.	Caption
4.2-7	RPP coating after exposure to $\underline{O}$ atom at 1930K
4.2-8	RPP coating after exposure to $\underline{N}$ atoms at 1830K. Note the denseness of the surface and the fewer number of cracks.
5.1-1	Atom concentration and gas temperature profiles in the stagnation region shock layer of a hypersonic, blunt-nosed body.
5.1-2	Approach to dissociation equilibrium in the shock layer of a hypersonic vehicle; flight velocity = 26 kfps; nose radius = 1 ft.; wall temperature = 1500K; comparison of prediction methods of Inger (1966) and Tong (1965).
5.2-1	Dependence of radiation equilibrium temperature on atom recombination coefficient for a 1 ft. nose radius body (3-dir under conditions of peak aerodynamic heating.
5.2-2	Predicted surface temperature vs. time during the re-entry of a 2 ft. nose radius Orbiter vehicle with RPP nose cap.
5.2-3	Predicted surface temperature vs. time during re-entry for a 1 ft. nose radius, unswept 2-dimensional leading edge of RPP material; $F_{Dam,i}$-limiting cases
5.2-4	Predicted surface temperature vs. time during re-entry for a 1 ft nose radius, unswept 2-dimensional leading edge of RPP material; $F_{Dam,i}$ calculated using the modified Tong (1965) correlation.
5.3-1	Bimolecular N-atom reactions within the boundary layer
5.3-2	Energy transfer effects of bimolecular gas phase N-atom reactions under conditions of peak aerodynamic heating.

1. INTRODUCTION

In an early series of papers on the aerodynamic heating of Earth re-entry vehicles [see, eg. Goulard (1958), Scala (1958), Rosner (1963, 1964a,b,c), Chung and Anderson (1961), Hartunian and Thompson (1963)] it was pointed out that significant reductions in peak heat transfer rates (ca. 3-4 fold) and radiation equilibrium temperatures [$T_w(\gamma=1) - T_w(\gamma=0) \approx 600K$] could be achieved for vehicles with appreciable aerodynamic lift[+], provided materials could be found with low atom recombination coefficients, γ. Indeed, it was concluded that "a low atom recombination coefficient γ for high temperature ceramics , cermets or refractory metal coatings could play a role comparable to high emittance in contributing to the success of an overall design" [Rosner (1964a)]. In the intervening years the focus of attention temporarily shifted off glide re-entry vehicles, and, in those cases where radiation cooling was significant, attention was confined to emittance control additives and oxidation protection. However, with the emergence of the NASA Space Shuttle mission it is essential to consider proposed orbiter vehicle thermal protection system (TPS) materials from the point of view of their catalytic activity for exothermically combining incident O-atoms and N-atoms. This is because the required insulation weight could be reduced appreciably if the attributes of low γ and high total emittance could be combined in the Orbiter TPS coatings[*]. Unfortunately, for the reasons outlined below, available literature and test

---

[+] Vehicles with little or no aerodynamic lift, depending on their ballistic parameter, decelerate at lower altitudes, causing appreciable atom recombination to occur in the denser gas boundary layer adjacent to the solid surface. The abovementioned predictions of significantly reduced heat transfer rate to noncatalytic surfaces for chemically "frozen" dissociated gas boundary layers have been verified in a number of laboratory studies - see eg. Deriugin <u>et al</u>. (1964), Carden (1966), Winkler and Griffin (1961), Pope (1968), Busing (1964), Anderson (1973).

[*] Orbiter re-use capability and large payload capacity are central to the economic viability of the Space Shuttle. Reduced outer surface temperatures due to low γ would favorably influence both of these factors.

procedures fail to provide the guidance and data required to fully exploit this phenomenon to optimize the Orbiter thermal protection system. First, available kinetic data on O and N atom recombination on refractory nonmetals do not extend to the high surface temperatures (> 1200K) anticipated during Orbiter re-entry. Second, available γ-data are limited to materials chemically far simpler than those likely to be employed on the Orbiter TPS. Third, owing in part to inadequate surface characterization for the materials which have been studied, there is little understanding of the subtle chemical and physical factors required to achieve low recombination efficiencies in newly formulated TPS coatings. Finally, currently used arc jet test procedures probably do not faithfully simulate the non-equilibrium O and N atom concentrations likely to be achieved in flight.

This report describes the results of a one-year, interdisciplinary research program initiated at Yale University by the NASA-Manned Spacecraft Center to develop the procedures and know-how necessary to assess and exploit low atom recombination probability in the design of the thermal protection systems for future lifting hypersonic re-entry vehicles of the Space Shuttle Orbiter type. The program was nominally divided into the four phases indicated below:

Program Phase	Report Section
A. Duct flow reactor measurements of γ for O and N atom recombination	2
B. Mass loss (ablation) experiments at high surface temperatures in O and N atom streams	3
C. Chemical and physical characterization of thermal protection system (TPS) materials coatings by X-ray photoelectron spectroscopy (XPS) and scanning electron microscopy (SEM)	4
D. Role of heterogeneous atom recombination in determining the temperature-time heating of the vehicle surface	5

A critical review and evaluation of alternate techniques and past measurements of O-atom and N-atom recombination coefficients was included in our first quarterly report (QPR-1) and will not be repeated here. Similarly, readers interested in a basic review of the XPS technique, and a summary of recent applications to chemically characterize solid surfaces are referred to QPR 1 and Carlson (1972). While our main concern has been with the development of generally applicable procedures (to provide the basis for future measurements, as required) our attention has been focused here primarily on two types of candidate Space Shuttle materials: a reusable surface insulation (RSI) coating and the siliconzied surface of a reinforced pyrolyzed plastic (RPP) leading edge/nose cap material. Thus, the illustrative kinetic and surface-characterization data reported in Sections 2-4 pertain to these materials. Section 5 contains the procedure we have devoloped for predicting the aerodynamic heating consequences of $\gamma_0(T_w)$-data, and gives illustrative results based on our γ-measurements on thin, flat specimens of the RPP (leading edge and nose cap) material up to 1710K (the approximate onset of appreciable mass loss). Also included in Section 5 is a summary discussion of (i) the energy transfer consequences of recombining O or N atoms to excited product molecules[+] and (ii) bimolecular exchange reactions capable of converting 2N into N_2 within the gas phase boundary layer. Section 6 is devoted to a summary of the principal conclusions we have reached, and our assessment of those areas in need of further work. Based on this preliminary study, the duct reactor and XPS techniques developed and illustrated herein, can play a valuable role indeed in future materials optimization research for hypersonic glide vehicles.

[+] For a more detailed account of our analysis of excited molecule formation/desorption/quenching, see Rosner and Feng (1973)

2. FLOW REACTOR γ -EXPERIMENTS

2.1 Apparatus and Experimental Techniques

2.1.1 Apparatus

A low pressure, fast flow duct atom recombination reactor has been constructed using the design criteria that were discussed in Section 3.3 of QPR 1. The reaction chamber is shown in Fig. 2.1-1 and consists of three sections. Section I and III of the reactor are constructed from quartz and each section consists of two lengths of 2.5 and 1.7cm i.d. cylindrical tubing, and a piece of square quartz tubing[+]. Section II of the reactor is a square duct constructed from sample material. The sample duct fits snugly along the outside of the square quartz pieces of Sections I and III, and the length of Section II may be varied by changing the distance between Section I and Section III.

Samples are heated by radiation from an inductively heated graphite susceptor. The cylindrical graphite susceptor, in which a square hole has been milled, provides a means of support for the flat samples strips from which the square sample duct is constructed. Strips of type 204 G.E. quartz sheet are inserted in the square hole in the susceptor between the graphite and the sample material[*]. This quartz insert provides a surface of low catalytic activity for atoms that diffuse through the cracks along the edges of the sample material, as well as reducing contamination of the sample by the graphite. Four to six layers of 0.001" thick tantalum foil are wrapped around the outside of the graphite susceptor in order to improve the heating efficiency. A 5kw, Lepel High Frequency Induction Heating Unit, Model No. T-5-3-KC is used to heat the susceptor.

[+] The square quartz tubing has 1.00 cm long inner sides and 0.15 cm thick walls

[*] Type 204 G.E. quartz sheet is reported to withstand temperatures up to 1533K for periods of time up to 2 months. For γ measurements on the LTV RPP material the quartz sheet was not used.

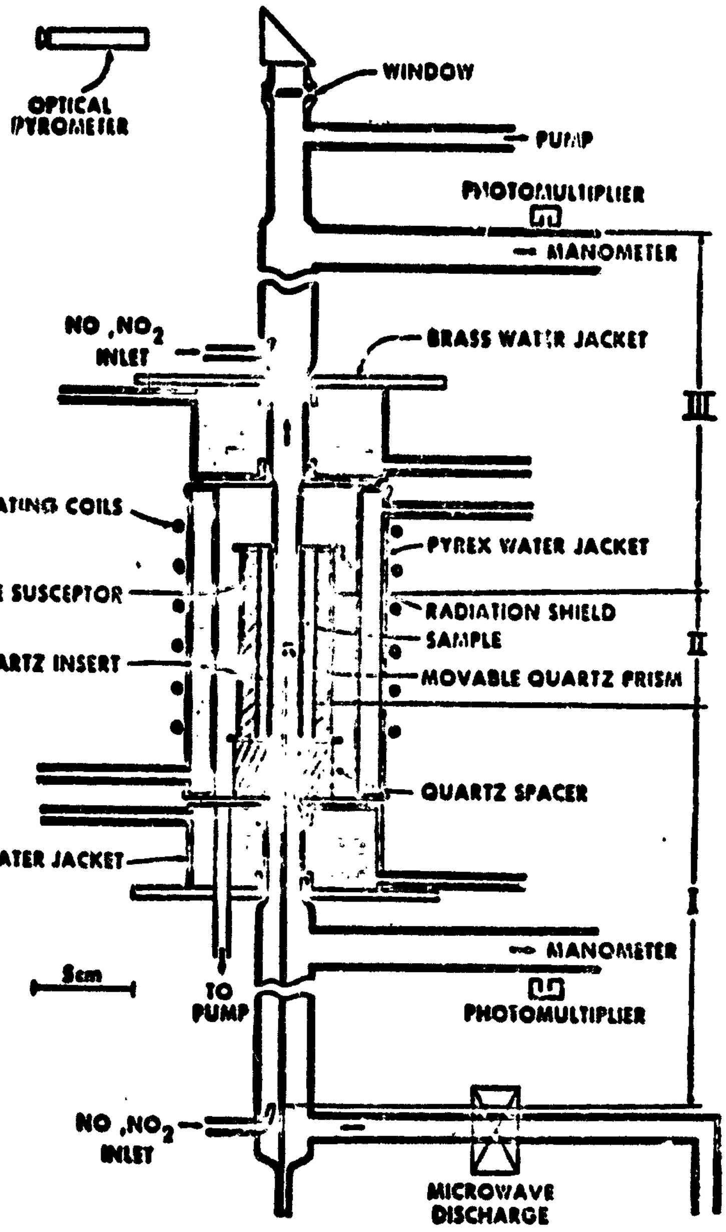

2.1-1 Schematic of duct atom recombination reactor

Temperature measurements are made using an optical pyrometer which views the reactor wall with the aid of a movable quartz prism, which is withdrawn during recombination coefficient measurements.

The walls of the reactor are cooled by the use of water jackets which surround the smaller pieces of cylindrical quartz tubing of Sections I and III. In addition, the pyrex cylinder which surrounds the graphite susceptor is water cooled.

Gas flows are regulated by calibrated critical velocity orifices, which are capable of yielding accurate gas flow rates for argon, nitrogen, oxygen, nitric oxide and nitrogen dioxide. The critical velocity orifice used to measure the NO_2 flow rate is submerged in a constant temperature water bath in order to reduce errors caused by the temperature dependent $2NO_2 \rightleftharpoons N_2O_4$ equilibrium. Argon (99. 995%), oxygen (99.6%), nitrogen (99.99%), nitric oxide (99.8%) and nitrogen dioxide (99.5%) are used without further purification.

The pressure in the reactor is measured both upstream and downstream by a single, differential oil[+] manometer connected to the titration observation side arms by a 3-way high vacuum stopcock.

2.1.2 Experimental Techniques

Oxygen and nitrogen atom concentrations are measured using the well known NO and NO_2 chemiluminescent titration reactions [Kaufman (1958) and (1961), Clyne and Thrush (1962) and Kistiakowsky and Volpi (1957)]. NO or NO_2 can be added either upstream or downstream and the intensity of the subsequent chemiluminescence is measured using an EMI Model No. 9558 photomultiplier[*]. The error in atom concentration measurements caused by the combination of finite titration

---

[*] The photomultiplier is equipped with a 5300 Å interference filter that has a bandwidth of 10 Å .

[+] Degassed, Norton DC 705 Diffusion Pump Oil is used for the manometer fluid reaction rates and the limited observation time was minimized by making the distance between the titration inlet and the observation side arm 10 cm. Under normal experimental conditions the titration reaction is at least 99% complete at this distance. The presence of of observation side arms permit use of the titration reaction when the atom concentration is exceptionally low or the flow velocity is extremely high.

Nitrogen/oxygen atom mixtures are produced by titrating upstream of Sec II a fraction of the initial nitrogen atom concentration with NO. In this mixture, N atoms are still titrated downstream with NO via the very fast reaction.

$$N + NO = N_2 + O$$

with the appearance of the greenish-yellow chemiluminescence , produced in the reaction

$$O + NO = NO_2 + h\nu$$

indicating the titration endpoint. A number of investigators [Mentijn *et al.* (1966) and Clyne and Thrush (1962)] have shown the intensity of this chemiluminescence, I, obeys the expression

$$I = I_o(O)(NO) \qquad (2.1\text{-}1)$$

where $(O)_t$ and $(NO)^*$ are the O atom and nitric oxide concentrations respectively, and I_o is a proportionality constant which depends upon the gas temperature and the geometry of the experimental apparatus. Using Eq. 21.-1, I_o can be determined in the absence of additional O atoms from the slope of a plot of I vs. (NO), since this slope equals $I_o(O)_t$ where $(O)_t = (N)$, the nitrogen atom concentration, which was determined from the titration endpoint. In the mixture of N and O atoms the problem of measuring (O), the oxygen atom concentration is complicated because $(O)_t$ is no longer equal to (N) but is a sum of (O) and (N). However, if I_o is determined in the absence of added oxygen, then (O) can be determined from the slope of I vs. (NO) since,

---

* The NO concentration used in this equation is equal to the added NO concentration minus the initial atom concentration $(N)_o$.

$$\frac{\Delta I}{\Delta(NO)} = I_o((N) + (0)) \qquad (2.1\text{-}2)$$

Measurement of the surface temperature of the sample material is made using an optical pyrometer which views the reactor wall with the aid of a movable quartz prism, which is withdrawn during recombination coefficient measurements. The transparency[+] of the optical system was determined by comparing the observed temperature of a heated filament when the pyrometer was viewing the filament directly and when it was sighted through the two prisms and the quartz window. The total transparency of the eight surfaces was found to be 0.75. This value, along with the emissivity of the sample, were used to calculate the true wall temperature.

[+] Transparency is defined as the ratio of the intensity of the transmitted light to that of the incident light.

2.2 Data Reduction Procedure

Here we outline our approach to the inference of accurate values of γ from measurements of atom flow rates in and out of the reactor described in Section 2.1 of this report [and Section 3.3 of QPR II] Owing to the reactor design procedure exploited in Section 3.2 of the latter report it proved sufficient to develop two "levels" of approximation to γ, the second of which constitutes our best estimate of the true recombination coefficient under the atom pressure-surface temperature conditions prevailing in the reactor.

An initial estimate of γ, hereafter written ${}^1\gamma$, has been obtained by inverting the simple reactor design equation [see Section 2.2.1 below] and making allowance for: a) increasing linear gas velocity associated with heat transfer and pressure drop within the reactor (shown schematically in Fig. 2.2-1), b) atom recombination on the cooled walls of the quartz inlet Section (I) and outlet Section (III).

For values of γ in excess of about 10^{-3} an improved value of γ written ${}^2\gamma$, was estimated by allowing for small corrections associated with transverse concentration and temperature gradients, and homogeneous atom loss, while simultaneously improving upon corrections a) and b) above. We have done this by integrating quasi-one dimensional conservation equations from reactor inlet to exit, until the measured overall atom conversion is reproduced. For this purpose, the level 1 approximation to γ is used to start the iterative calculation, the square duct reactor is treated as an equivalent or "effective" diameter circular duct, and available correlations for heat and mass transfer coefficients appropriate to this geometry are used. As mentioned above, due to our reactor design procedure the value of ${}^2\gamma$ is expected to be of the same order of magnitude as ${}^1\gamma$ and ${}^2\gamma$ and sufficiently accurate for subsequent estimates of aerodynamic heating. Further details concerning each of these procedures are given below.

2.2.1 "Level 1" Inference of γ

Here we apply a simple one-dimensional atom balance equation to each of Sections I, II and III shown in Figure 2.1-1, neglecting transverse atom concentration gradients. Since no appreciable axial diffusion at station i or e was present during the experiment, the overall atom conversion may be expressed as $1 - (\omega_{A,e}/\omega_{A,i})$, where ω_A is the atom mass fraction[†] (A = 0 or N). Eliminating the unknown atom mass fractions at the inlet and outlet of Section II (fabricated of the material of interest), we readily find:

$$\ln\left(\frac{\omega_{A,i}}{\omega_{A,e}}\right) = \left(\frac{\gamma\bar{c}L}{Ud_{eff}}\right)_{I} + \left(\frac{\gamma\bar{c}L}{Ud_{eff}}\right)_{II} + \left(\frac{\gamma\bar{c}L}{Ud_{eff}}\right)_{III} \qquad (2.2\text{-}1)$$

where $\bar{c}$ is the mean thermal speed of the incident atoms, and the U's are appropriately averaged linear velocities over the indicated reactor sections. This equation can be solved directly for $\gamma_{II} \equiv {}^1\gamma$ using estimates of γ_I and γ_{III}. In this way we find

$${}^1\gamma = {}^1\gamma^{(o)} - \Delta^1\gamma \qquad (2.2\text{-}2)$$

where

$${}^1\gamma^{(o)} \equiv \left(\frac{Ud_{eff}}{\bar{c}L}\right)_{II} \cdot \ln\left(\frac{\omega_{A,i}}{\omega_{A,e}}\right) \qquad (2.2\text{-}3)$$

and the quantity $\Delta^1\gamma$, defined by

$$\Delta^1\gamma = \gamma_I \left[\left(\frac{\bar{c}L}{Ud_{eff}}\right) \cdot \left(\frac{\bar{c}L}{Ud_{eff}}\right)_{II}^{-1} \right] + \gamma_{III} \left[\left(\frac{\bar{c}L}{Ud_{eff}}\right)_{III} \cdot \left(\frac{\bar{c}L}{Ud_{eff}}\right)_{II}^{-1} \right] \qquad (2.2\text{-}4)$$

is seen to correct ${}^1\gamma^{(o)}$ for the effects of atom recombination on the water-cooled silica walls of Sections I and III. Values of L and d_{eff} for each duct section are determined by the reactor geometry, whereas the corresponding average

---

[†] This ratio $\omega_{A,e}/\omega_{A,i}$ is related to the measured chemiluminescent intensity ratio *via* corrections for total density changes through the reactor and the temperature dependence of the chemiluminescent "rate constants". The latter correction being important for experiments on O-atom recombination.

values of $\bar{c}$ and U can be determined from gas temperature and pressure measurements, coupled to a knowledge of the total reactor mass flow rate. Values of γ_I and γ_{III} have been obtained from "blank" experiments in an "all quartz" modification of our duct reactor.

2.2.2 Level 2 Inference of γ

Owing mainly to the possible importance of transverse concentration gradients, it was decided to systematically improve upon the value ${}^1\gamma$ obtained from Eq. 2.2-2. To do this the actual duct reactor is considered to be equivalant to that of a cylinder with an equivalent local diameter $d_{eff} \equiv 4 \cdot (\text{Area})/(\text{Perimeter})$. Conservation of atom mass, energy and linear momentum then lead to the following set of coupled ordinary differential equations governing the "bulk" or "mixing cup average" values of $\omega_A(z)$ and $T(z)$ [written, respectively, $\omega_{A,b}(z)$ and $T_b(z)$] and the local static pressure $p(z)$:

$$\frac{d\omega_{A,b}}{dz} = \begin{cases} -\frac{A}{\dot{m}} \left[\frac{\rho\,\gamma_A(T_w) \cdot \bar{c} \cdot \omega_{A,b}}{d_{eff}} + \mathcal{G}_A \right] & \text{(Reactor Sections I and III)} \quad (2.2\text{-}5a) \\ -\frac{A}{\dot{m}} \left[j''_{A;w} \cdot \frac{4}{d_{eff}} + \mathcal{G}_A \right] & \text{(Reactor Section II)} \quad (2.2\text{-}5b) \end{cases}$$

$$\frac{dT_b}{dz} = \frac{A}{\dot{m} \cdot c_{p,b}} \cdot \left[-\frac{4}{d_{eff}} \cdot \dot{q}''_w + \dot{Q}'''_A \right] \quad (2.2\text{-}6)$$

$$\frac{dp}{dz} = \frac{-32}{d_{eff}} \cdot \frac{\dot{m}}{A} \cdot \nu_b \cdot f_\nu\left(\frac{T_w}{T_b}\right) \quad (2.2\text{-}7)$$

The first term in Eq. (2.2-5) accounts for the atom loss due to recombination at the wall. Only in reactor Section II are transverse concentration gradients expected to be important. Therefore the bulk composition, $\omega_{A,b}$ can be used to compute the heterogeneous recombination in the walls of Sections I and III. The second term in Equation (2.2-5) accounts for atom loss via gas-phase atomic recombination.

In the energy equation (2.2-6) the first term accounts for the Fourier conduction energy flux at the reactor wall. The second term, symbolically written $\dot{Q}'''_A$, accounts for the increase in gas temperature due to the heat released via gas-phase recombination. Owing to our choice of reactor operating conditions, this term is usually negligible.

Equation (2.2-7) is a differential form of the Hagen-Poiseuille law giving the pressure drop in a circular duct with laminar flow [see, eg. Bird, Stewart and Lightfoot (1963)]. The function f_ν is introduced to correct for the influence of transverse nonuniformity in gas mixture viscosity.

A more detailed statement of the individual terms in Equations 2.2-5 to 2.2-7) is given in Appendix A2.2 The effects accounted for in deriving and solving these equations can be summarized as follows:

E1 Simultaneous presence of several chemical species in the reactor. The thermal and transport properties of the prevailing gas mixture (atoms, parent molecules, and argon carrier) have been calculated in accord with Chapman-Enskog theory, using a Lennard-Jones 12:6 interaction potential [Hirshfelder, Curtiss and Bird (1954)].

E2 Transverse diffusion of atoms [Rosner (1964d)].

E3 Heterogeneous atom recombination on the cooled inlet and outlet walls of the reactor (Sections I and III).

E4 Atom loss and molecule production due to atom recombination

E5 Transverse heat fluxes associated with the prevailing difference between the wall and bulk gas temperature

E6 Pressure drop in each section of the reactor

E7 Heat released due to homogeneous atom recombination

In view of our reactor design and operating conditions, effects such as axial atom diffusion and axial heat conduction were not expected to be appreciable and have not been included in the present data reduction procedure. Transverse diffusion of atomic species and heat have been included by using local values of the simplest[+] Nusselt transfer coefficient [Bird, Stewart and Lightfoot (1963), Rosner (1964d)]. One of the assumed wall-temperature profiles is shown in Fig. (2.2-1). Arguments of the Nusselt number for heat transfer were based on the downstream distances $(z - z_{au})$, $(z - z_u)$ and $(z - z_d)$ since heat fluxes are expected to be significantly altered at stations z_{au}, z_u and z_d, where the thermal boundary conditions change abruptly. Appreciable atom loss by wall recombination starts at station z_u. Therefore the Nusselt number for mass-transfer is based on $z - z_u$.

Using ${}^1\gamma$ to guide our initial estimate ${}^2\gamma^{(1)}$, the coupled system of nonlinear, first order ordinary differential equations is integrated in the forward z direction using a Runge-Kutta numerical procedure[‡]. The integration is started with the experimentally measured values of $\omega_{A,b}$, T_b and p at the inlet of the reactor.

This quasi-one dimensional formulation of our reactor transport problem includes Seider-Tate-type functions[see, eg. Kays (1966)] correcting constant property transport laws for property nonuniformities so that the computed temperature and pressure of the gas at the exit of the reactor in the absence of atomic species are in agreement with our measured values.

After each integration the values of $\omega_{A,e}$(experim) and $\omega_{A,e}$(computed) are compared and a new value of ${}^2\gamma$ is chosen using an interpolation procedure equivalent to "the false position method". Thus, the value ${}^2\gamma^{(r+1)}$ is determined from

---

[+] ie. that corresponding to a wall temperature (or composition) distribution given by the Heaviside function [Kays (1966)].

[‡] This and other numerical procedures used herein are discussed, for example, in Hildebrand (1956).

our previous estimate ${}^{2}\gamma^{(r)}$ and our first estimate ${}^{2}\gamma^{(1)}$ as follows:

$$ {}^{2}\gamma^{(r+1)} = \frac{{}^{2}\gamma^{(r+1)} \cdot W({}^{2}\gamma^{(1)}) - {}^{2}\gamma^{(1)} \cdot W({}^{2}\gamma^{(r)})}{W({}^{2}\gamma^{(1)}) - W({}^{2}\gamma^{(r)})} \qquad (2.2\text{-}8) $$

where $W({}^{2}\gamma^{(r)}) \equiv (\omega_{A,e}({}^{2}\gamma^{(r)}))_{comp} - (\omega_{A,e})_{exp}$ and, as mentioned earlier, frequently ${}^{2}\gamma^{(1)} = {}^{1}\gamma$. This iteration scheme is terminated when a value ${}^{2}\gamma$ is found so that it provides satisfactory agreement (within 1 percent) between $(\omega_{A,e})_{comp}$ and $(\omega_{A,e})_{exp}$.

A digital computer program has been developed to carry out the numerical integrations and interpolations involved in this level 2 procedure for determining γ . This program also includes subroutines which provide the species and mixture specific heat[+], thermal conductivity and viscosity, as well as the species binary(and pseudo-binary) diffusion coefficients. Subroutines for computing the prevailing Nusselt transfer coefficient, and heats of formation for O and N atoms are also included. For test surfaces with γ in the approximate range $\gamma < 3 \times 10^{-2}$ the differences between ${}^{2}\gamma$ and ${}^{1}\gamma$ computed from the same data are not excessive and ${}^{2}\gamma$ can be considered to be an accurate value of the true, prevailing atom recombination coefficient. However, ${}^{2}\gamma$ -values exceeding about 5×10^{-2} of necessity include appreciable corrections for transverse atom concentration gradients and are intrinsically sensitive to the accuracy of our convective diffusion calculations in the duct reactor. This turned out to be especially true for the high temperature O and N data on the RPP-material, hence the absolute accuracy of our reported recombination coefficients for high temperature RPP degenerates much above about 1250K*. In practice, however, this is not a serious limitation of the technique[✦] since it indicates that

---

[+] We are indebted to C.P. Li (Lockheed Electronics, Houston) for supplying curve fit routines for individual species heat capacities and enthalpies.

[*] At this temperature the ${}^{2}\gamma/{}^{1}\gamma$ is about 2.5. ${}^{2}\gamma$ values above about 5×10^{-1} are more than one-order of magnitude above ${}^{1}\gamma$.

[✦] Accurate γ-values for $\gamma > 10^{-1}$ could perhaps be obtained at very low atom pressures using molecular beam techniques but practical interest in materials with such high recombination coefficients even at low pressures is slight.

for re-entry application this material would essentially behave as a perfect atom recombination catalyst (see Section 5.2). Indeed, for γ-values in this range no continuum reactor or arc-jet experiment is possible which would avoid large diffusion corrections [Rosner (1972)].

Figure 2.2-1 shows a typical set of predicted $\omega_{A,B}(z)$, $T_b(z)$ and $p(z)$ profiles through the duct flow reactor for an O-atom/RSI-coating run with argon carrier gas at $T_w = 1440K$. Note that while the largest portion of the O-atom loss (cf. $\omega_{A,B}(z)$) occurs in reactor section II, in general a correction for atom losses in the partially water cooled quartz[+] sections (I, III) must also be included. This particular run is one for which the reactor fractional conversion (of O to O_2) is large and hence is not suitable for inferences of the p_0 independence of γ_0, assumed in calculating ${}^2\gamma$. Also shown in Fig. 2.2-1 are the small gas pressure drop[‡] and net bulk temperature rise in traversing the entire reactor (Sections I, II, and III). Further details concerning these calculations are given in Appendix 2.2. Using this procedure and a reasonable estimate for ${}^2\gamma^{(1)}$ (usually larger than ${}^1\gamma$) the representative IBM 360/67 computer time for a γ-inference was about 30 sec.

[+] γ_i values for quartz are discussed in Section 2.3.1, which follows

[‡] In determining the function f_ν (cf. Eq. (2.2-7) use is made of the fact that the exit pressure p_e, is routinely measured (see Appendix A2.2)

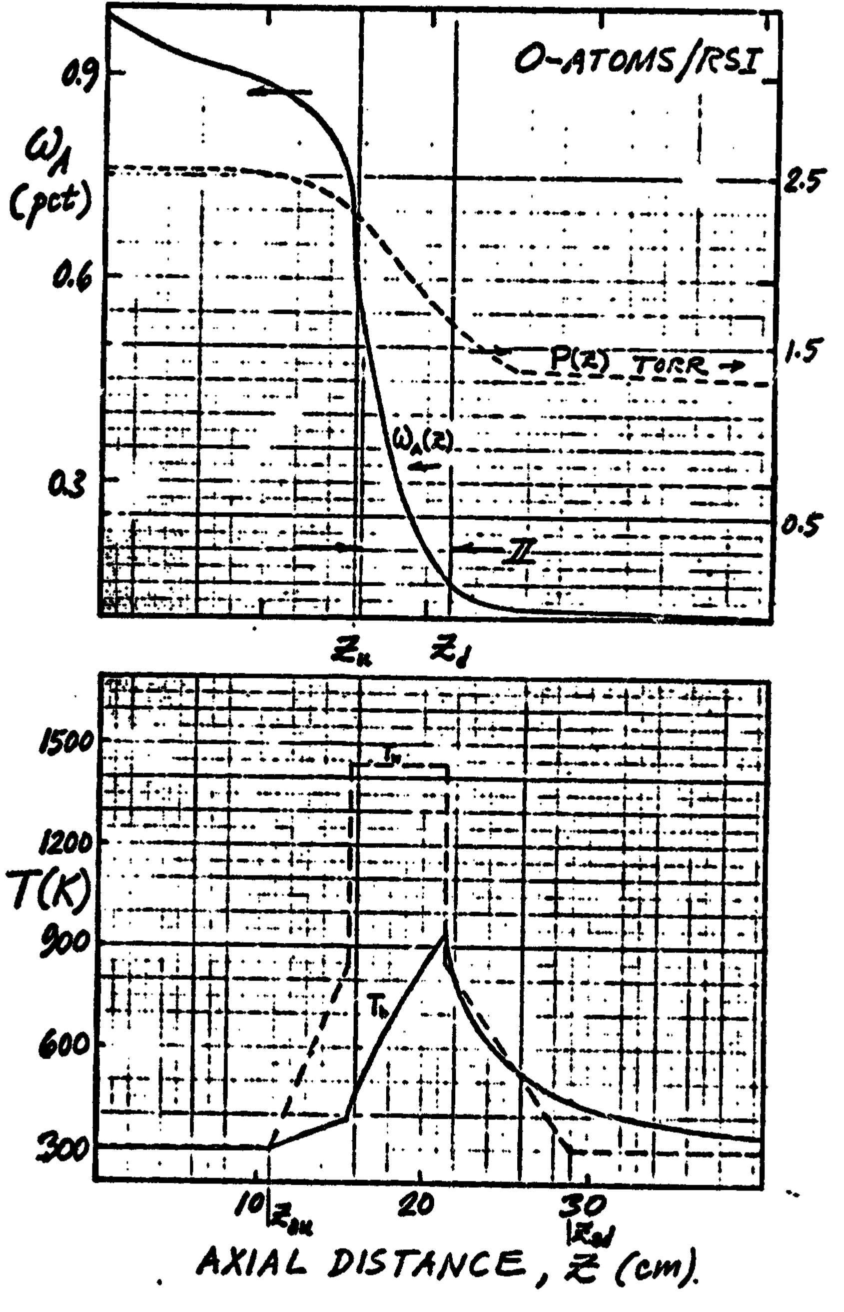

2.2-1 Computed profiles of atom concentration, pressure and gas temperature in duct atom recombination reactor; N-atom/RPP run; T_w = 1120K

2.3 Atom Recombination Coefficient Results for Quartz, Nickel, RSI and RPP

2.3.1 Atom Recombination on Quartz

To accurately evaluate γ for sample TPS materials it is necessary to assess the extent of atom recombination in Sections I and III of our duct flow reactor, which are made of quartz[+]. For this reason γ was measured for O and N atoms on quartz.

Room temperature oxygen atom recombination coefficients on quartz determined using our duct flow reactor are given in Table 2.3-1. The values range from 1.18×10^{-4} to 10.7×10^{-4}, with an average value of 4.0×10^{-4}. As shown in Table 2.3-2 this average value is in agreement with the values reported by Dickens and Sutcliffe (1964) and Krongelb and Strandberg (1959), and Greaves and Linnett (1958) and (1959), but is 10 times larger than the values reported by Hacker et al. (1961) and Berkowitz-Mattuck (1969). Although the value of γ_0 are reproducible for experiments conducted on a specific day, the large variation in γ_0 measured on different days made it necessary to determine γ_0 on quartz before and after the performance of recombination experiments on sample TPS materials. The average of the two γ_0's was used in the determination of coefficients on the sample material.

It was possible to measure the fractional conversion of O atoms through the reactor by three different techniques. In the first method, denoted in Table 2.3-3 by (NO^u), the relative oxygen atom concentration change was measured by adding a small amount of NO upstream of the sample and measuring the chemiluminescent intensity both upstream and downstream. This method yielded values for γ_0 which were consistently lower than the values determined by the second technique, in which NO was added downstream of the sample for the downstream chemiluminescent intensity measurements, denoted by

---

[+] The quartz was cleaned by using the glass-cleaning solution described in Rosebury (1965), with a final rinse of 15% HF solution.

Table 2.3-1

Oxygen Atom Recombination Coefficients ($^2\gamma_0$) on Quartz at Room Temperature

Date	Argon[a]	Oxygen[a]	P_T[b]	O_{out}/O_{in}	$^2\gamma_0$
3/5/73	98.3	86.5	2.19	0.746	1.18(-4)[c]
3/8/73	99.5	87.0	0.66	0.687	3.39(-4)
	99.5	87.0	2.71	0.376	4.52(-4)
	99.5	87.0	3.36	0.242	4.81(-4)
5/3/73	389	23.3	1.47	0.562	10.73(-4)
5/7/73	185	16.2	1.31	0.550	10.35(-4)
6/8/73	358	25.7	3.92	0.273	3.85(-4)
	358	25.7	3.91	0.310	3.39(-4)
6/11/73	288	14.2	1.74	0.612	2.93(-4)
	288	14.2	1.79	0.655	2.44(-4)
6/20/73	385	36.3	2.48	0.464	4.23(-4)
	385	75.7	2.87	0.423	4.18(-4)
7/17/73	371	77.1	2.66	0.374	5.15(-4)
8/9/73	388	68.0	2.58	0.804	1.32(-4)
	388	36.0	1.36	0.859	1.59(-4)
8/10/73	389	72.5	2.96	0.651	2.12(-4)
8/20/73	386	71.5	2.66	0.708	1.89(-4)

a Flow rate in cc.atm/min

b Pressure in Section II in torr

c 1.18(-4) ≡ 1.18×10^{-4}

Table 2.3-2

Oxygen Atom Recombination Coefficients on Quartz at Room Temperature

Reference	γ
Greaves and Linnett (1958)	7.1(-4)
Greaves and Linnett (1959)	1.6(-4)
Dickens and Sutcliffe (1964)	3.5(-4)
Krongelb and Strandberg (1959)	3.2(-4)
Hacker et al. (1961)	0.4(-4)
Berkowitz-Mattuck (1969)	0.4(-4)
This work	4.0(-4)

Table 2.3-3

Oxygen Atom Recombination Coefficients ($^2\gamma_0$) on Quartz at Room Temperature

Date	$^2\gamma_0(NO^u)$	$^2\gamma_0(NO^d)$	$^2\gamma_0(NO_2)$
3/5/73	0.56(-4)†	1.18(-4)	
3/8/73	2.56(-4)	3.39(-4)	
	4.04(-4)	4.52(-4)	
5/7/73	6.40(-4)	10.3 (-4)	9.67(-4)
		10.7 (-4)	9.46(-4)
6/8/73	1.94(-4)	3.85(-4)	
	2.07(-4)	3.39(-4)	3.42(-4)
6/11/73	1.51(-4)	2.44(-4)	
6/20/73	4.23(-4)	5.02(-4)	
6/21/73	4.18(-4)	5.26(-4)	
6/22/73	4.35(-4)	5.39(-4)	

† 0.56(-4) ≡ 0.56 x 10^{-4}

(NO^d). NO_2 titration of O atoms was the third method used. Table 2.3-2 shows that the results using the NO_2 titration technique are in agreement with the method in which NO is added downstream, (NO^d).

The systematic discrepancy between the two NO-chemiluminescent techniques at near-room temperature is probably due to NO poisoning the walls of the reactor so that γ_0 is lowered. Because of the effect of NO on γ_0, only γ_0 values which were determined by adding NO downstream were used to evaluate γ for the TPS materials inserted in Section II.

Because only a portion of Sections I and III is water cooled, and in order to evaluate high temperature atom recombination coefficients for TPS materials mounted in Section II, it was necessary to estimate γ_0 on quartz at elevated temperatures (see Section 2.2). A quartz "wall" reactor was fitted into Section II and measured in the usual manner. To determine the quartz wall temperature <u>via</u> optical pyrometry the outside of the quartz tube was blackened with a fuel rich flame. Unfortunately, upon reactor disassembly it was found that the blackening material had reacted away. Therefore, the "observed" temperature was that of the outer graphite susceptor and not that of the quartz wall. The results of this experiment are shown in Fig. 2.3-1, along with the high temperature data of Greaves and Linnett (1959) and Berkowitz-Mattuck (1969). Assuming that our observed temperatures are higher than the true wall temperature, it is probable that our high temperature γ_0 values are in agreement with those of Greaves and Linnett (1959). For this reason, the high temperature γ_0 values of Greaves and Linnett for quartz were used in our $^2\gamma_0$ data reduction procedure (see Section 2.2).

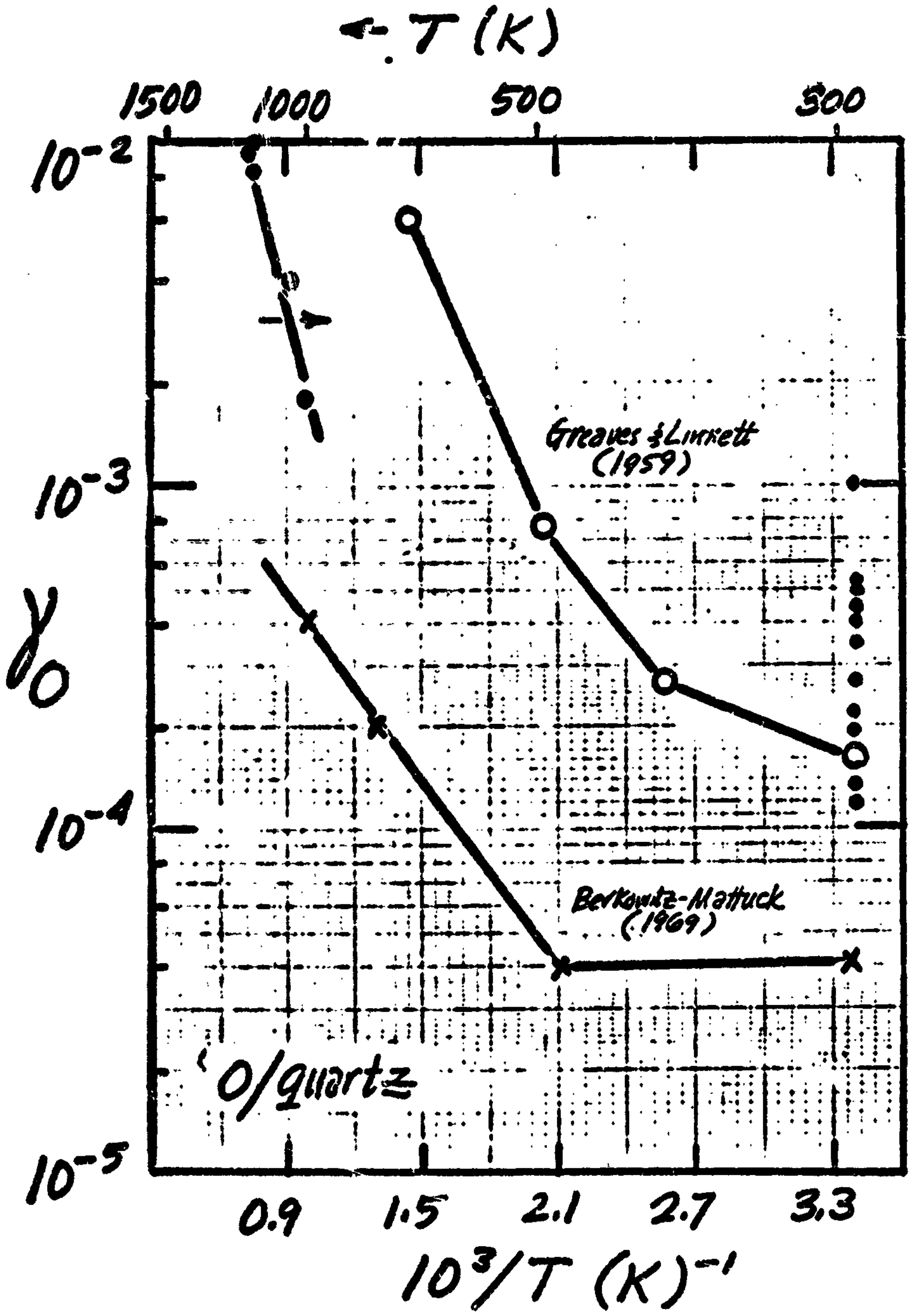

2.3-1 Temperature dependence of O-atom recombination on quartz ● Present work

Room temperature nitrogen atom recombination appears to be much less sensitive to slight changes in the quartz than O atom recombination. For ten different determinations, γ_N ranged between 1.54 and 3.73 x 10^{-4} with average value of 2.27 x 10^{-4}. This value of γ_N is lower than the value of 8.0 x 10^{-4} reported by Marshall (1962). The calculated γ_N on quartz at elevated temperatures are shown in Fig. 2.3-2. It is apparent from our data that γ_N has a maximum value (occuring at an apparent temperature of 1250K) of about 1.3 x 10^{-2} and then decreases rapidly to a value of approximately 6 x 10^{-3} at 1355K. Unfortunately, it is not possible to correlate these apparent temperatures to the true wall temperature, and therefore it is very difficult to theorize on the cause of this sharp drop in the value of γ_N. It should be noted that although no maximum was observed for γ_O on quartz, the maximum apparent temperature reached in the O atom experiments was 1230K. The high temperature γ_N values reported by Marshall (1962) show a much smaller temperature dependence than is indicated by our data. In addition, up to a measured temperature of 1200K no maximum appears in his data.

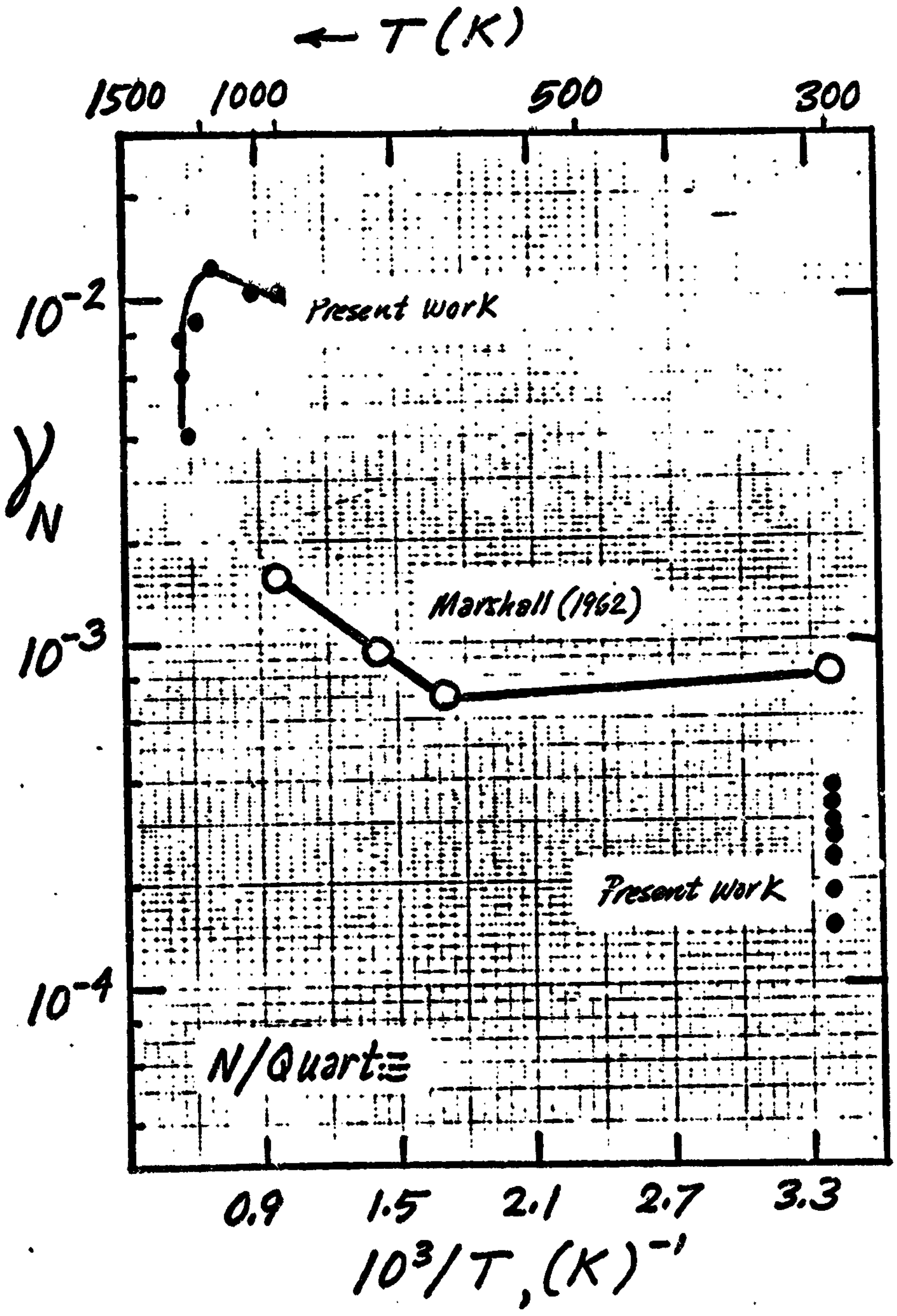

2.2-2 Temperature dependence of N-atom recombination on quartz; ● Present work

2.3.2 Atom Recombination on Nickel

Room temperature, oxygen atom recombination coefficients on NiO are given in Table 2.3-4. The nickel strips used in these experiments were made of Grade A nickel which had been cleaned by the method described by Rosebury (1969). For these experiments the oxygen atom partial pressure was between 4×10^{-2} and 8×10^{-2} torr.

Our room temperature results for O atom recombination on NiO are in agreement with those of Greaves and Linnett (1958) and (1959)† but are higher than the value given by Dickens and Sutcliffe (1964)†. Upon cycling the NiO samples there is an apparent increase γ_0. Since XPS analysis on both the fresh nickel sample and the cycled sample indicated the presence of only NiO on the surface the increase in γ_0 is probably due to a roughening of the surface upon heating.

Unlike the initial experiments on NiO (QPR 3), in later experiments no trend towards lower values of γ_0 were observed during the initial exposure of the nickel surface to O atoms. This observation may be explained by the fact that XPS results of the material that was used in the initial experiments indicated that its surface before O atom exposure was a thin layer of NiO over Ni while in the later experiment the surface contained only NiO. Therefore the initially high values may be indicative of a Ni surface for which γ_0 has been measured as 2.8×10^{-2} [Greaves and Linnett (1958)].

The results obtained for the oxygen atom recombination on nickel have allowed us to check our reactor design criteria (see Section 3.1 of QPR 1). These criteria predict that for low values of $\gamma(\leq 10^{-3})$ the calculated surface recombination coefficient should not differ whether the ${}^{1}\gamma$ or the ${}^{2}\gamma$ method is used for the calculation.

---

† Greaves and Linnett report a γ_0 for NiO between $7.8 - 8.9 \times 10^{-3}$ while Dickens *et al*. report a value of 1.5×10^{-3}

However, for higher values of $\gamma(\sim 10^{-2})$, radial atom concentrations gradients may become significant[†] and the $^2\gamma$ calculations would yield a higher value for the surface recombination coefficient than the $^1\gamma$ calculations.

Table 2.3-5 shows that the reactor design criteria are indeed correct. The $^1\gamma$ values for quartz, corrected for homogeneous atom loss, are in good agreement with the $^2\gamma$ values. For the quartz experiments the predicted radial concentration ratio,*ie*, the atom concentration at the wall divided by the bulk atom concentration, is 0.99. For NiO, however, the $^2\gamma$ value is significantly larger than that predicted by $^1\gamma$, and the radial atom concentration ratio is approximately 0.80. This indicates, as predicted by the design criteria, that for large γ values one must consider radial atom concentration gradients.

Certainly if our data reduction procedure is to be meaningful $^2\gamma_0$ should be independent of the total gas flow rate and total pressure. This independence is shown in Table 2.3-4 for the experiments conducted on 8/14/73. In these experiments the total flow rate was reduced from 728 cc.atm/min to 357 cc.atm/min and calculated $^2\gamma_0$ did not significantly change. Varying the total pressure from 1.90 - 1.30 torr also did not effect the calculated γ value. High temperature oxygen atom recombination experiments were carried out on NiO. At temperatures around 1000K our experiments indicated that γ_0 was greater than 7×10^{-1}. This value of γ_0 is higher than the value of 1.2×10^{-2} predicted by extrapolation of the results of Dickens and Sutcliffe (1964)[‡].

[†] The extent of these concentration gradients depends upon the total pressure in the reactor.

[‡] Their data extended to temperatures of 650K.

2.3.3 Atom Recombination on RPP Coating

The measured oxygen atom surface recombination coefficients on LTV RPP material are given[+] in Fig. 2.3-3. The data cover a temperature range of 1037 to 1735K. In order to check if γ_0 is independent of the O atom concentration the oxygen atom partial pressures were varied between 2×10^{-2} and 7×10^{-2} torr, and with no observable change in the measured value of γ_0.

Corrections to the observed wall temperature measured by the optical pyrometer were based on a spectral emissivity of RPP at 6500 Å of 0.80. This emissivity value is probably a lower limit to the true value because 1) the emissivity of SiC, the major component in the RPP coating, is between 0.85 - 0.92 at 6500 Å [Touloukian and Dewitt (1972)] and 2) the configuration of the reactor is such that Section II approaches a black body condition.

Our $^2\gamma$ data reduction procedure does not differentiate between atoms lost by recombination on the sample surface and atoms lost by a reaction with the surface coating. For this reason, at high temperatures it is possible for the measured atom recombination coefficient to be influenced by the reaction probability. As can be seen in Fig. 2.3-3, the Si(orC) atom removal probability ε_0 is about 10% of the measured γ_0 at 1670K. Owing to our definition of ε_0 (see Section 3.2) one can show that $\gamma_{0,app} = 2\varepsilon_0 + \gamma_0$; thus, the true value of γ_0 (corrected for atom loss by reaction with the substrate) probably begins to level out at temperatures much above 1730K (not shown).

Fresh RPP material has a room temperature γ_0 value ranging between $1.14 - 1.31 \times 10^{-2}$. However, upon heating this material in the presence of oxygen atoms, the room temperature γ_0 value decreases to values ranging between $1.55 - 5.60 \times 10^{-3}$. This decrease in room temperature γ_0 after heating is accompanied by a change in the surface character of RPP since the surface of fresh RPP material consists mainly of SiC, while the surface of material heated in O atoms is mostly SiO_2 (see Section 4) which indicates that SiO_2 has a lower O atom recombination probability than SiC.

[+] If the O-atom/quartz data of Berkowitz-Mattuck (1969) were used to predict O-atom losses in Sections I, III this would only further raise our γ_0-inference by some 30-40 percent. However as discussed in Section 2.3, it appears that in this case the data of Greaves and Linnett (1959) (cf. Fig. 2.3-1) are more appropriate.

Table 2.3-4

Oxygen Atom Recombination Coefficient ($^2\gamma_0$) on NiO at Room Temperature

Date	Argon[a]	Oxygen[a]	P_T[b]	$^2\gamma_0$
3/20/73	490	200	2.02	1.06(-2)
8/14/73	524	204	1.96	1.02(-2)[c]
	249	92	1.30	9.27(-3)
	249	92	1.90	9.06(-3)
	265	92	1.25	9.22(-3)
8/15/73	271[d]	93	1.23	4.11(-2)
	271[e]	93	1.23	4.11(-2)

a Flow rate in cc.atm/min

b Pressure in Section II in torr

c 1.02(-2) ≡ 1.02×10^{-2}

d Reactor had been cycled once to a temperature of 1057K.

e Reactor had been cycled twice to a temperature of 1150K.

Table 2.3-5

Comparison of $^1\gamma$ and $^2\gamma$ Calculations for Oxygen Atom Recombination on Quartz and NiO

Date	Surface	$^1\gamma_0$	$^2\gamma_0$
3/8/73	Quartz	3.47(-4)+	3.39(-4)
	Quartz	4.30(-4)	4.52(-4)
3/20/73	NiO	7.50(-3)	10.6 (-3)

+ 3.47(-4) ≡ 3.47×10^{-4}

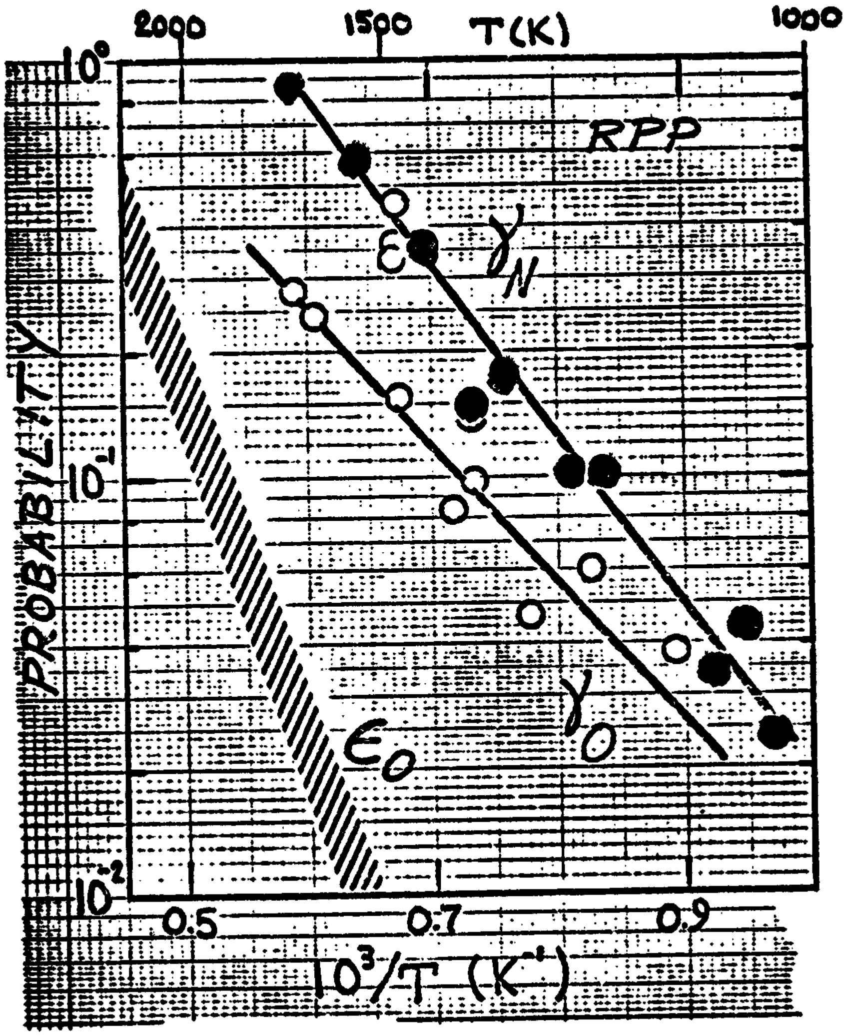

2.3-3 O-atom and N-atom recombination coefficients on the LTV-RPP material; ○, γ_O-values; □, O-atom reaction probability; ● γ_N-values; typical experimental conditions for O-atom runs: argon flow: 260 cc·atm/min, O_2 flow: 115 cc·atm/min, upstream pressure at room temperature: 1.4 torr; gas flow velocity in Reactor Section II: 2500 cm/sec; typical experimental conditions for N-atom runs: argon flow rate: 250 cc·atm/min, N_2 flow rate: 450 cc·atm/min, upstream pressure at room temperature: 20 torr, gas flow velocity in Reactor Section II: 2700 cm/sec.

Figure 2.3-3 also contains our data for N-atom surface recombination coefficients as a function of 1/T for temperatures between 1029 and 1719K. Within experimental uncertainty, γ_N increases linearly with 1/T. The N atom partial pressure ranged between 5.4×10^{-3} and 3.1×10^{-2} torr and γ_N was found to be independent of N atom pressure. The values of the room temperature γ_N ranged between 1.05 and 4.57×10^{-3} and, unlike the case of O atom recombination, the room temperature value of γ_N showed no significant change when RPP was heated in O or N atoms.

Finally, exploratory measurements were made of the apparent values of ${}^2\gamma_O$ and ${}^2\gamma_N$ on RPP in mixtures of O and N atoms between 1153 and 1673K. In the data reduction procedure (cf. Section 2.2) no attempt was made to include the possible influence of nitrogen-oxygen bimolecular exchange reactions (see, eg. Section 5.3) - ie. the O-atom conversion was formally used to infer ${}^2\gamma_O$ and the N-atom conversion was formally used to infer ${}^2\gamma_N$. N + O mixtures were generated by dissociating a dilute N_2 + Ar mixture, then adding NO to convert a portion of the N-atoms to O-atoms via $N + NO \rightarrow N_2 + O$. The N atom partial pressure was varied between 8.8×10^{-3} and 1.2×10^{-2} torr, while the O atom partial pressure ranged between 6.9×10^{-3} and 1.5×10^{-2} torr. The ratio of initial O atom concentration to initial N atom concentration was varied between 0.68 and 1.2 with no apparent effect on the measured γ_O or γ_N values. From a comparison between γ_O measured in an O/O_2 system and that measured in a N/O mixture it appeared that the simultaneous presence of N atoms had no significant effect on γ_O. Scatter in the corresponding ${}^2\gamma_N$ values measured in the presence of O atoms did not allow a quantitative comparison to be made on the ${}^2\gamma_N$ values measured in the absence of O atoms. However, it appears that γ_O and γ_N for RPP are not changed by more than about a factor of 2 when recombination takes place in a mixture of N and O atoms.

2.3.4 Atom Recombination on RSI

The measured oxygen atom surface recombination coefficients on RSI at temperatures between 901K[+] and 1452K[‡] are shown in Fig. 2.3-4. The O-atom data shown in this figure represent an RSI sample that was undergoing three cycles in temperature. The open symbols represent measurements made while the wall temperature was increasing while the blackened symbols represent measurements taken while the temperature was decreasing. Two observations can be made from this data; 1) γ_0 goes through a maximum value of $T \approx 1250K$ and 2) measurements of γ_0 made during the decreasing temperature part of the cycle are slightly higher ($\approx 50\%$) than γ_0 measured during the increasing temperature part of the cycle. It is interesting to note that γ_0 for RSI is approximately the same as the measured γ_0 for RPP at $T = 1100K$. This is not an unexpected result since XPS analysis has shown that both surfaces are essentially SiO_2. At higher temperatures the RSI surface may begin to soften[*] and result in a lowering of γ_0.

Room temperature γ_0 values have been measured in the range 1.03 - 4.62×10^{-3}[±]. SEM results (see Section 4) indicate that RSI material cycled to high temperature has a much rougher surface than fresh material. However, within experimental error this increased surface area due to roughness does not increase the room temperature γ_0 values[#]. Again it is interesting to note that room temperature γ_0 for RSI and γ_0 for cycled RPP are essentially identical.

[+] This temperature was estimated from the change in pressure in Section I due to the increased wall temperature in Section II.

[‡] The spectral emissivity of the RSI coating is 0.79 at 6500 Å

[*] Borosilicate Glass has a softening temperature of ≈1100K and a working temperature of 1510K[Rosebury, (1965)].

[±] The first value of γ_0 measured for RSI was 1.4×10^{-4}. However, we have not been able to reproduce this low value.

[#] The increase in γ_0 would have to be > a factor of 3 before [illegible] would become significant.

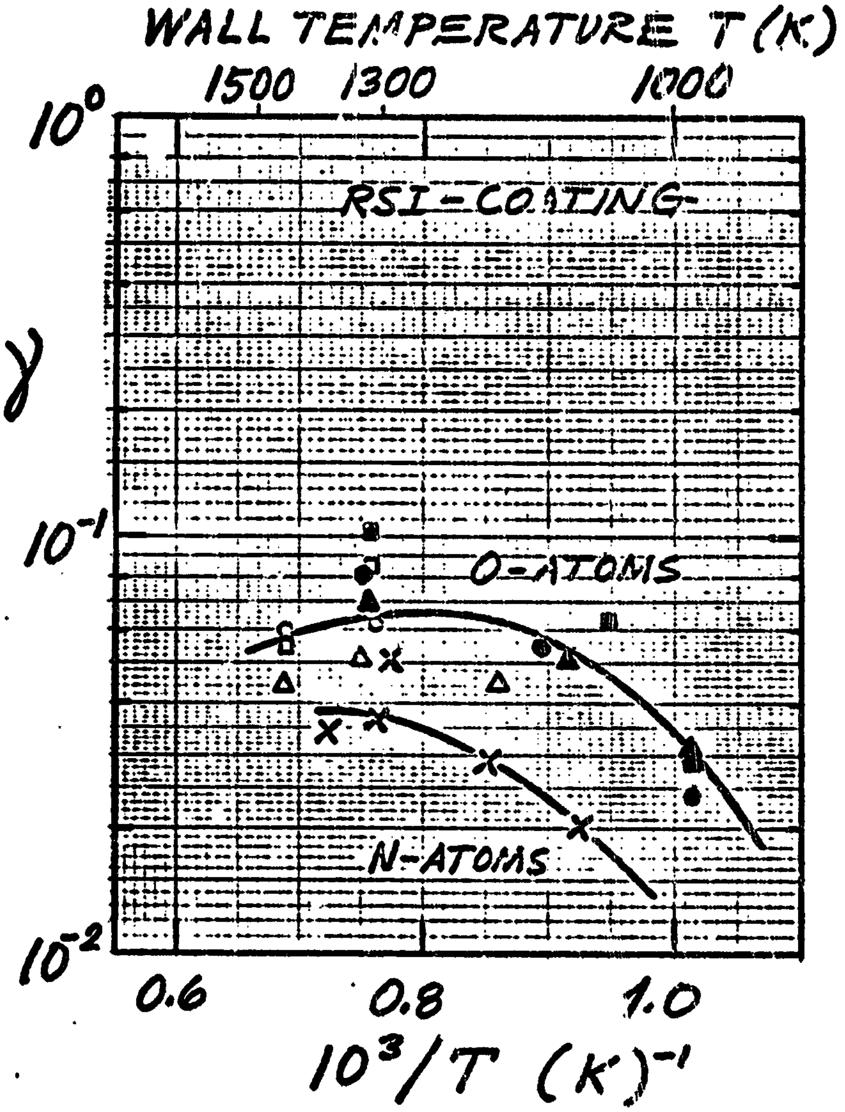

2.3-4

O-atom and N-atom recombination coefficients on the RSI coating material. For O-atom data: open symbols are measurements taken while the wall temperature was increasing, closed symbols are measurements taken when the wall temperature was decreasing; ○, measurements on the first cycle; □, measurements on the second cycle △, measurements on the third cycle. Typical experimental conditions for O-atom experiments: argon flow: 390 cc·atm/min O_2 flow rate: 70 cc·atm/min; upstream pressure at room temperature: 1.6 torr; gas flow velocity in reactor Section II: 2350 cm/sec. Typical experimental conditions for N-atom data: argon flow rate: 302 cc·atm/min, N_2 flow rate: 305 cc·atm/min; upstream pressure at room temperature: 1.6 torr; gas flow velocity in reactor Section II: 2600 cm/sec

To insure that the measured value of γ_0 at high temperature is independent of O atom concentration, the O atom partial pressure was varied between 0.5 and 1.5 x 10^{-2} torr. At 1100K, over this atom concentration range, γ_0 ranged between 5.47 - 5.82 x 10^{-2}.

Figure 2.3-4 also shows γ_N vs. 1/T for RSI. N-atom recombination on RSI also appears to go through a maximum value. Unfortunately, these experiments were in the relatively narrow temperature range 1078K to 1384K, which is not large enough to effectively characterize the curve. The γ_N values for RSI fall slightly below the γ_0 values and significantly below the γ_N values for RPP at 1100K. This difference between γ_N for RSI and RPP may be explained by differences in the RSI and RPP surfaces in the presence of nitrogen (see Section 4).

As in the case of RPP, we made several exploratory experiments on the apparent values of γ_0 and γ_N on RSI in the simultaneous presence of O and N atoms. Apparent oxygen atom recombination coefficients in the presence of N atoms, from 1048K to 1412K exhibited the same shape as the results for γ_0 in the absence of N, but appeared to be shifted to to slightly lower values (ca. factor of 2). Results for nitrogen atom surface recombination coefficients in the presence of O atom as a function of 1/T, were too scattered to make detailed comparisons, but did not differ from the $^{2}\gamma_N$ values shown in Fig.2.3-4 by more than a factor of 2.

The low values of γ_0, γ_N (ca. 2 x 10^{-2}) measured on RSI-coating at ca. 1000K imply a negligible contribution to the reported γ-values at higher temperatures from atom losses in the cracks at the corners of the square cross-section duct. If the crack area were a perfect atom sink and represented a constant fraction (say 1 percent) of the total wetted area then (i) the apparent γ could never fall below this constant lower bound, and (ii) a negligible error would be introduced into any γ-values reported above about 10^{-1}. Thus, the high values reported for γ_0 and γ_N on coated RPP above 1300K (see Section 2.3.3) cannot be attributed to atom loss in the cracks where the flat RPP sections meet.

3. MASS LOSS EXPERIMENTS- LEADING EDGE MATERIAL

Rosner and Allendorf (1970 a,b) have studied the reaction of pure, dense pyrolytic silicon carbide in molecular and atomic oxygen and nitrogen and O + N mixtures at surface temperatures above 1750K. Their results show that the SiC removal probabilities in O, N, or O_2 are greater than 0.1 at T $\geq$ 2000K and not strongly dependent on temperature or pressure. However, at lower temperature the reaction probabilities are strongly temperature and pressure dependent. Interestingly enough, rates in O + N mixtures were found to be substantially below those in pure O or N.

These results were interpreted to indicate formation at lower temperatures of a passivating SiO_2, Si_3N_4, or silicon-oxynitride layer, depending on the reactant gas used. Vaporization of this layer at highest temperatures exposes the SiC to direct attack by the reactant gas.

Stagnation arc jet tests on RPP at Vought Missiles and Space Co. [LTV, (1972)] showed rough agreement with the above results on pure β-SiC(s). However, comparison of these experiments contains significant uncertainties due to extrapolation to higher pressure. Moreover, our XPS results (see Section 4.3) indicate that small amounts of Al_2O_3 in the SiC-coated RPP specimens concentrate on the surface during arc jet tests. Moreover, RPP coating density is half that of pyrolytic SiC. Since this suggests intrinsic differences between the _in situ_ RPP coating and pure β-SiC(s) we have carried out a brief investigation of the reaction between O, N, and O_2 and the RPP coating by exploiting the experimental techniques previously used in our laboratories for SiC(s).

3.1 Technique

The reaction of SiC-coated RPP with dissociated oxygen and/or nitrogen gas mixtures is carried out in the transonic vacuum flow reactor described earlier [Rosner and Allendorf (1967)] which is illustrated in Fig.3.1-1[*] In this reactor, metered argon-reactant gas mixtures pass through the discharge tube where the 2450 Mc, 120 watt microwave discharge partially dissociates the reactant molecules. The dissociated gas mixture emerges from the discharge tube at a linear flow velocity of ca. 2 x 10^4 cm/sec and a total pressure of 1 torr and flows over the electrically heated specimen[†]. Specimen heating current is manually adjusted during reaction to maintain a constant brightness temperature, T_{br}, as observed with an optical pyrometer.

The specimens are rectangular pieces of coated RPP with the carbon substrate exposed on one side and the SiC coating exposed on the other side. Initial specimen dimensions are ca. 0.1 cm thick by 0.2 cm wide x 3.8 cm long. RPP coating and substrate each comprise about 50% of the initial sample thickness. These samples were cut from a larger piece of coated RPP with a silicon carbide saw. Reaction rates were calculated from the change in thickness of the RPP coating after exposure to reactant at elevated temperatures for a measured interval of time. Since the RPP coating/substrate interface was poorly defined, it was not possible to measure thickness changes in the direction perpendicular to the coating-substrate interface. Therefore recession rates were calculated from the change in width of the samples measured parallel to the coating-substrate interface. Small variations in the width of a specimen required that changes in width be measured from low magnification (20x) photomicrographs, to insure that the the initial and final width measurements were made at the same point.

---

[*] The voltage taps in Fig.3.1-1 are used for monitoring resistance of metal specimens. They were not used in experiments with RPP specimens.

[†] The combination of high flow velocity and small specimen diameter prevents diffusion limitations on the reactant arrival rate. This has been demonstrated by showing flow rate independence of the reaction rate at constant reactant partial pressure in studies of the Pt/F atom reaction.

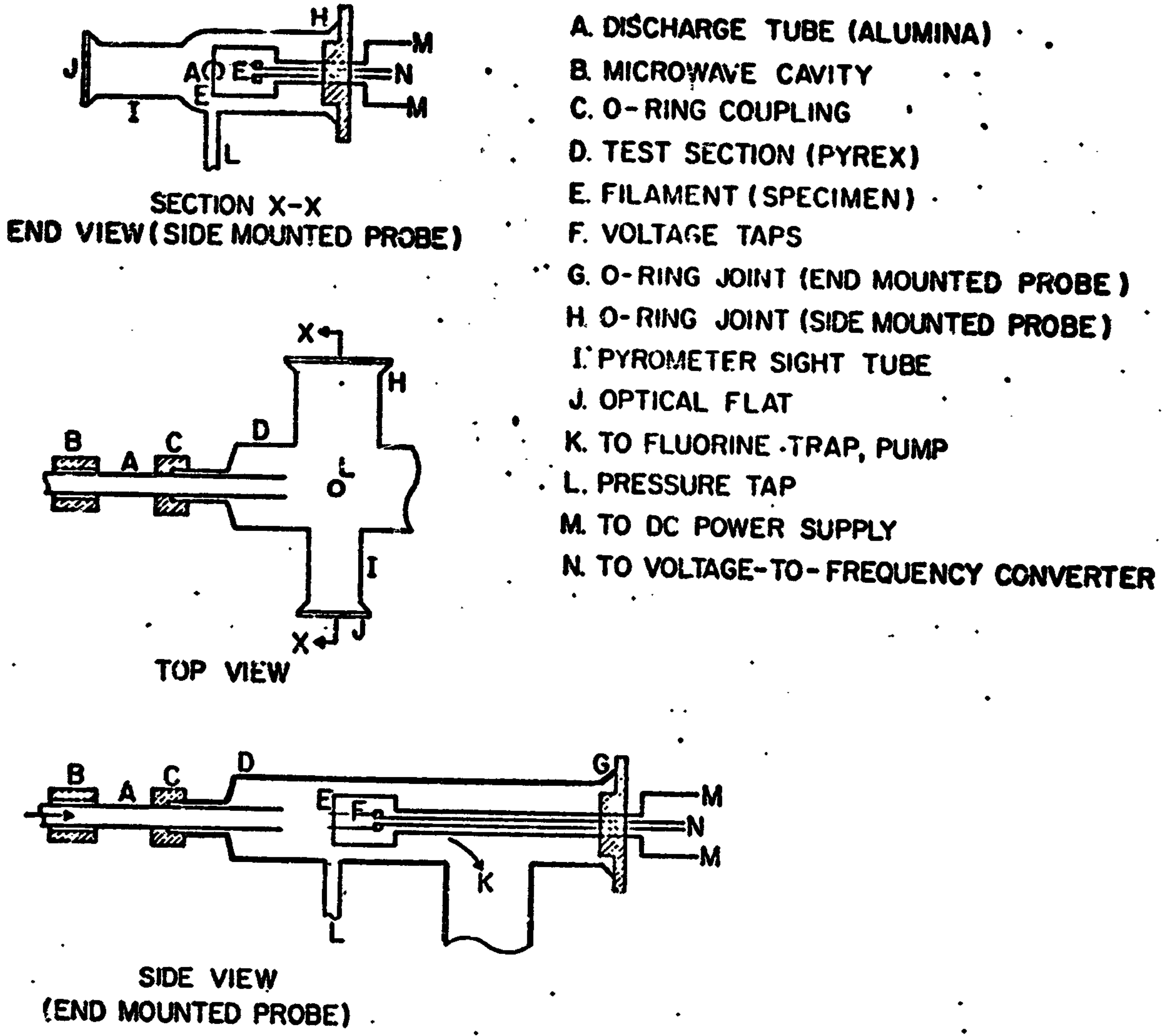

SECTION X-X
END VIEW (SIDE MOUNTED PROBE)

TOP VIEW

SIDE VIEW
(END MOUNTED PROBE)

A. DISCHARGE TUBE (ALUMINA)
B. MICROWAVE CAVITY
C. O-RING COUPLING
D. TEST SECTION (PYREX)
E. FILAMENT (SPECIMEN)
F. VOLTAGE TAPS
G. O-RING JOINT (END MOUNTED PROBE)
H. O-RING JOINT (SIDE MOUNTED PROBE)
I. PYROMETER SIGHT TUBE
J. OPTICAL FLAT
K. TO FLUORINE TRAP, PUMP
L. PRESSURE TAP
M. TO DC POWER SUPPLY
N. TO VOLTAGE-TO-FREQUENCY CONVERTER

3.i-1 Schematic of transonic atom flow reactor used for RPP mass loss experiments

Specimen temperature measurements showed negligible temperature gradients along the central 0.5 cm of the specimen length. However, significant temperature gradients perpendicular to the coating-substrate interface were observed, because the electrical heating current passed mainly through the carbon substrate. The observed temperature gradients were compared with those calculated on the basis of a thermal conductivity of 0.016 cal/(cm·deg K·sec) [LTV(1972) , p. 217] a total emissivity of 0.9[(LTV,(1972), p. 215] for the RPP coating and a small heat flow due to convection. It was concluded that the spectral emissivity of the RPP coating is not less than 90% that of the substrate. Using 0.9 for ε(6650A) for the carbon substrate a value of 0.8 was deduced for the RPP coating and used in data reduction. Temperature corrections were also calculated for window reflection losses according to

$$1/T_{wi} - 1/T_{Nwi} = 5.0 \times 10^{-6} \text{ (deg K)}^{-1} \qquad (3.1\text{-}1)$$

where T_{wi} and T_{Nwi} are observed filament temperatures with and without the window.

Experiments were performed at 1 torr. Nominal O_2 pressures were 0.01 torr or 0.05 torr and N_2 pressures were 0.5 torr. Chemiluminescent titrations (see Section 2.1) showed that approximately 25% of the O_2 was dissociated and that the N atom pressure was between 1×10^{-2} and 3×10^{-2} torr,

Many of the RPP mass loss specimens were examined by XPS (Section 4.1) and SEM (Section 4.2).

3.2 Results

RPP mass loss results are presented in Table 3.2-1 for oxygen reactant, in Table 3.2-2 for oxygen-nitrogen mixture experiments, and in Table 3.2-3 for nitrogen reactant. An Arrhenius diagram of the oxygen data is presented in Fig. 3.2-1 and of the oxygen-nitrogen mixture data in Fig. 3.2-2.

Reaction probabilities, equal to the ratio of the SiC removal flux and the reactant arrival flux, were calculated from the oxygen data.[†] An

---

[†] Thus, we define $\varepsilon_0 \equiv \xi''_{(Si)}/Z''_0$ (or $\xi''_{(C)}/Z''_0$) and $\varepsilon_{0_2} \equiv \xi''_{(Si)}/Z''_{0_2}$ (or $\xi''_{(C)}/Z''_{0_2}$) where $\xi''_{(i)}$ is the evaporation flux of element i (i = Si,C) and Z''_i is the arrival rate (flux) of species i (i = 0,0_2) at temperature T_w. For all expts. ε_{0_2} was calculated, neglecting the affect of partial dissociation. Inasmuch as partial dissociation did not significantly influence the rate, $\varepsilon_0 \gtrsim \varepsilon_{0_2}/2\sqrt{2}$, (since dissociation increases the flux by $2\sqrt{2}$). However, the precision of our experiments limits ε_0 to $0.5\ \varepsilon_{0_2} \le \varepsilon_0 \le 1.06\ \varepsilon_{0_2}$ (assuming that ε_0 is not less than half ε_{0_2})

Table 3.2-1

SiC coated RPP Mass Loss Experimental Results

Expt. No.	§	T (K)	Ambient P_{O_2} (10^{-2} torr)	Δd (cm)	Δt (sec)	Δd/Δt (cm/sec)	Remarks
21	M	1618	5.82	$4.5(-3)^{\#(1)}$	240	1.874(-5)	Blackish appearance
24	A	"	5.30	$2.9(-3)^{(1)}$	240	1.21(-5)	
46	A	"	6.15	$0^{(2)}$	180	0	Dense SiO_2 film
49	A	"	5.95	$0^{(2)}$	360	0	Dense SiO_2 film
55*	A	"	5.65	0	360	0	" quenched in argon
33	A	1722	1.19	$1.5(-3)^{(1)}$	720	2.08(-6)	Glass-like particles
34	M	"	1.33	$3(-3)^{(1)}$	600	5.0(-6)	Large glass-like particles
22	A	"	5.40	$7(-3)^{(1)}$	180	3.89(-[illegible])	Flakes (Brownish appearance)
25	M	"	5.48	$8(-3)^{(1)}$	180	4.45(-5)	Small glass-like particles
50*	A	"	6.15	$3.6(-5)^{(1)}$	420	3.6(-5)	Annealed at 2013K for 20 min. Large glass particles on the side
51	A	"	5.90	$-^{(2)}$	720	-	Annealed at 2013K for 15 min. Continuous molten SiO_2 film
52	A	"	5.60	$-^{(2)}$	720	-	Large glass particles on the side; some on the surface.
32	A	1826	1.24	9.8(-3)	600	1.63(-5)	Small glass-like particles
31	M	"	1.23	6.1(-3)	600	1.02(-5)	", Blackish appearance
20	M	"	5.47	6.4(-3)	180	3.56(-5)	Blackish appearance
53*	M	"	5.60	2.7(-2)	360	1.5(-4)	" , quenched in argon small glass-like particles
26	A	"	5.47	6.4(-3)	120	5.33(-5)	Glass-like particles
54*	A	"	5.90	2.5(-2)	180	1.38(-4)	Blackish appearance, quenched in argon.
28*		1930	1.25	1.45(-3)	600	2.42(-5)	
29*		"	1.25	7.4(-3)	300	2.47(-5)	
30*		"	1.25	1.69(-2)	600	2.83(-5)	"
27		"	5.56	1.43(-2)	120	1.19(-4)	Blackish appearance
23		"	5.62	1.49(-2)	120	1.24(-4)	"
13		2013	1.14	1.45(-2)	600	2.42(-5)	
14		"	1.26	1.30(-2)	540	2.41(-5)	
15		"	1.27	9.7(-3)	600	1.62(-5)	Blackish appearance
16*		"	1.32	5.6(-3)	360	1.56(-5)	"
18		"	5.56	1.44(-2)	180	8.0(-5)	
19		"	5.80	2.93(-2)	180	1.63(-4)	"
17		2088	1.22	1.03(-2)	240	4.29(-5)	
35		2141	1.25	1.09(-2)	180	6.06(-5)	

---

* Samples examined by XPS (See Section 4.1)

\# 4.5(-3) ≡ 4.5 x 10^{-3} etc.

(1) Dimensional change was measured after scraping off the adherent product film

(2) No dimensional change was observed because of the adherent product film; attempt was not made to remove the film.

§ A = atomic, M = molecular

Table 3.2-2

SiC Coated RPP Mass Loss Experimental Results - Reaction with <u>O</u> + <u>N</u> Mixtures(1)

Expt.No.	T (K)	Ambient $p(O_2)$ (10^{-2} torr)	$p(N_2)$	Δd (cm)	Δt (sec)	Δd/Δt (cm/sec)	Remarks
36*	1410	1.17	55	0	1800	0	Dense SiO_2 film, some SiO_2 is observed on C side
37*	1618	1.20	57	3.1(-3)	1200	2.6(-6)	Dense SiO_2 film
59*	"	1.18	56	1.8(-3)	1200	1.5(-6)	" ,quenched in Argon
60*	1722	0.90	43	3.2(-3)	900	3.5(-6)	Continuous molten SiO_2 film, quenched in Argon
41*	"	1.31	60	3.8(-3)	900	4.3(-6)	Continuous molten SiO_2 film
43	"	1.31	60	6.6(-3) (2)	600	1.1(-5)	Numerous glass particles
38*	1826	1.25	57	7.5(-3)	720	1.0(-5)	Small glass particles
44*	"	1.35	60	1.0(-2)	600	1.7(-5)	" " ";a Ta plate was placed behind the specimen to collect the condensate
45*	"	1.28	60	6.4(-3)	600	1.1(-5)	" , annealed at 2018K for 20 min.
61*	"	1.15	54.5	5.9(-3)	720	8.2(-6)	Quenched in argon some glass particles on the end
40*	1930	1.14	53	1.8(-2)	900	2.0(-5)	Small glass particles
39*	2013	1.39	62	8.6(-3)	600	1.4(-5)	" " "
62*	"	1.17	55.5	1.2(-2)	600	2.0(-5)	" quenched in argon
42*	2088	1.30	60	1.0(-2)	600	1.7(-5)	Some small glass particles

(1) All mixtures are dissociated

(2) Dimensional change was measured after removing the film

* XPS analyses were made after reaction

Table 3.2-3

SiC Coated RPP Mass Loss Experimental Results. Nitrogen

Expt.No.	§	Temp (K)	Ambient pN_2 (10^{-2} torr)	Δd	Δt (sec)	$\frac{\Delta d}{\Delta t}$ (cm/sec)	Remarks
48*	A	1826	57	0	300	0	Dense product film
56*	A	2013	54.5	3.6(-3)	600	6.0(-6)	Small white particles over the surface; loosely adherent
57*	M	"	54.5	0	600	0	Black appearance

* XPS analysis were made after reaction

§ A = atomic   M = molecular

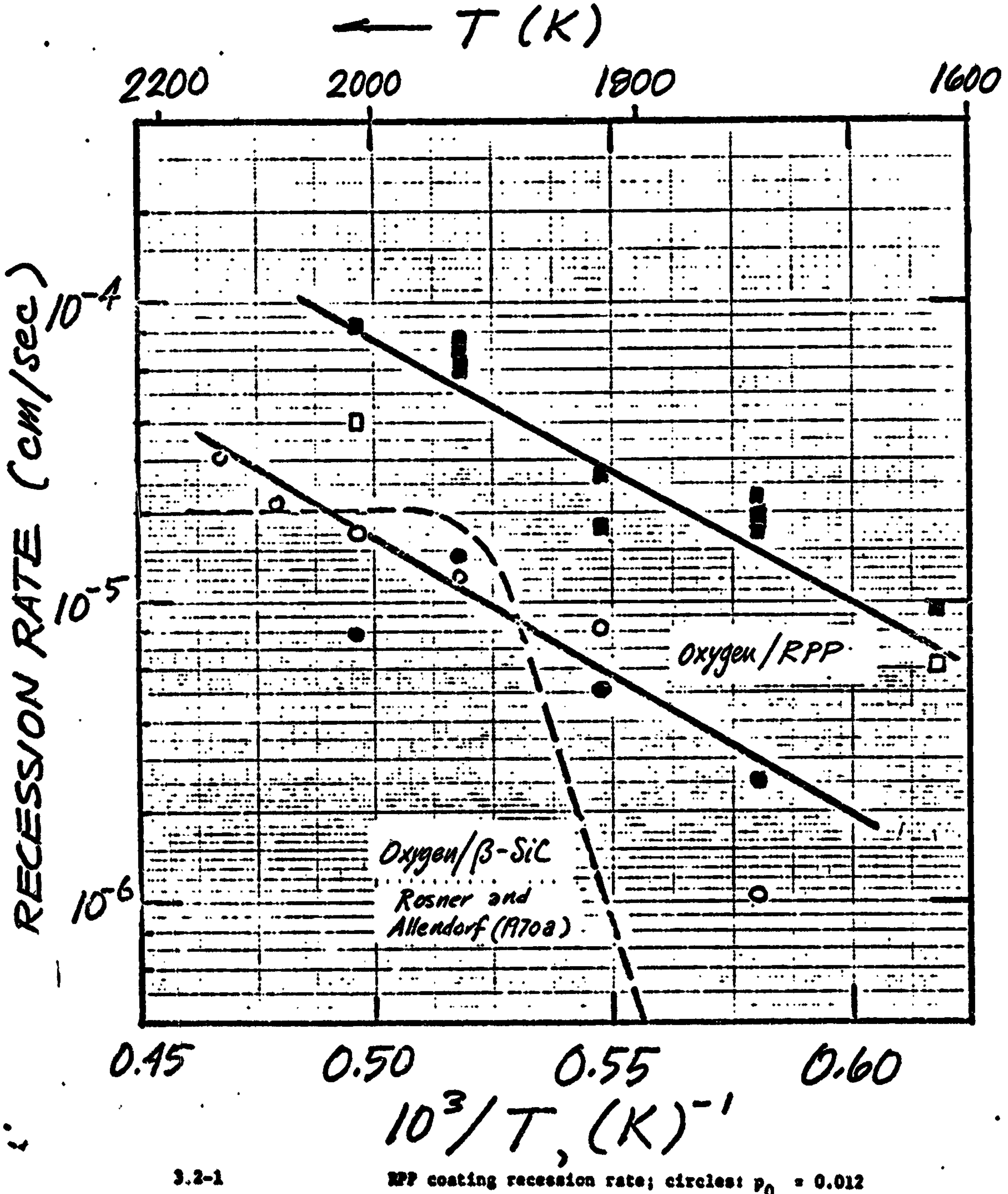

3.2-1 RPP coating recession rate; circles: p_{O_2} = 0.012 torr; Squares: p_{O_2} = 0.055 torr. Open symbols denote 25% dissociated gas mixture; filled symbols denote molecular reactants; dashed line is from Rosner and Allendorf (1970a) for the β-SiC/O reaction at $p_O = 10^{-2}$ torr.

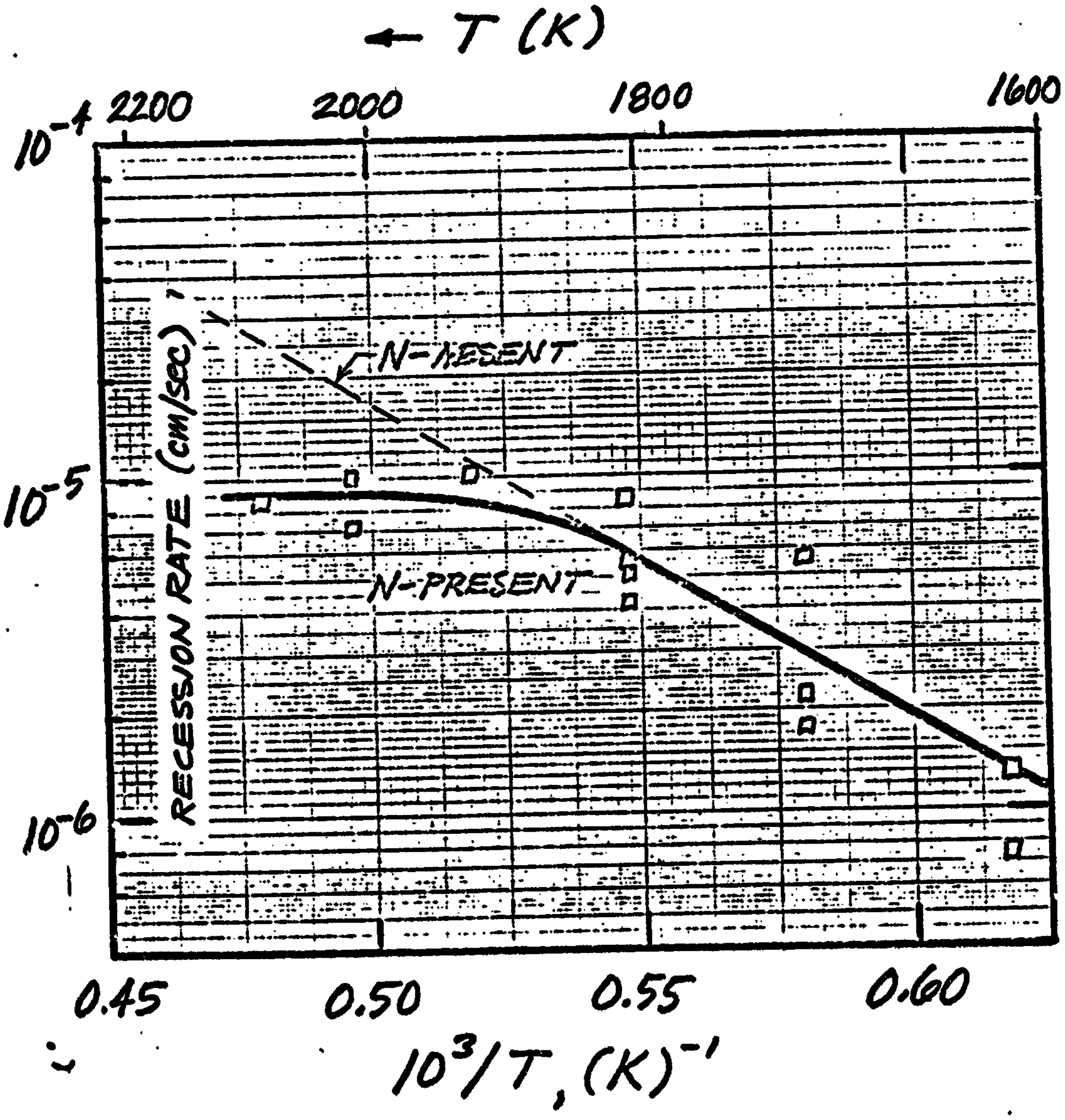

3.2-2 RPP coating recession rate in a dissociated O_2/N_2 mixture. Dashed line is rate in absence of nitrogen

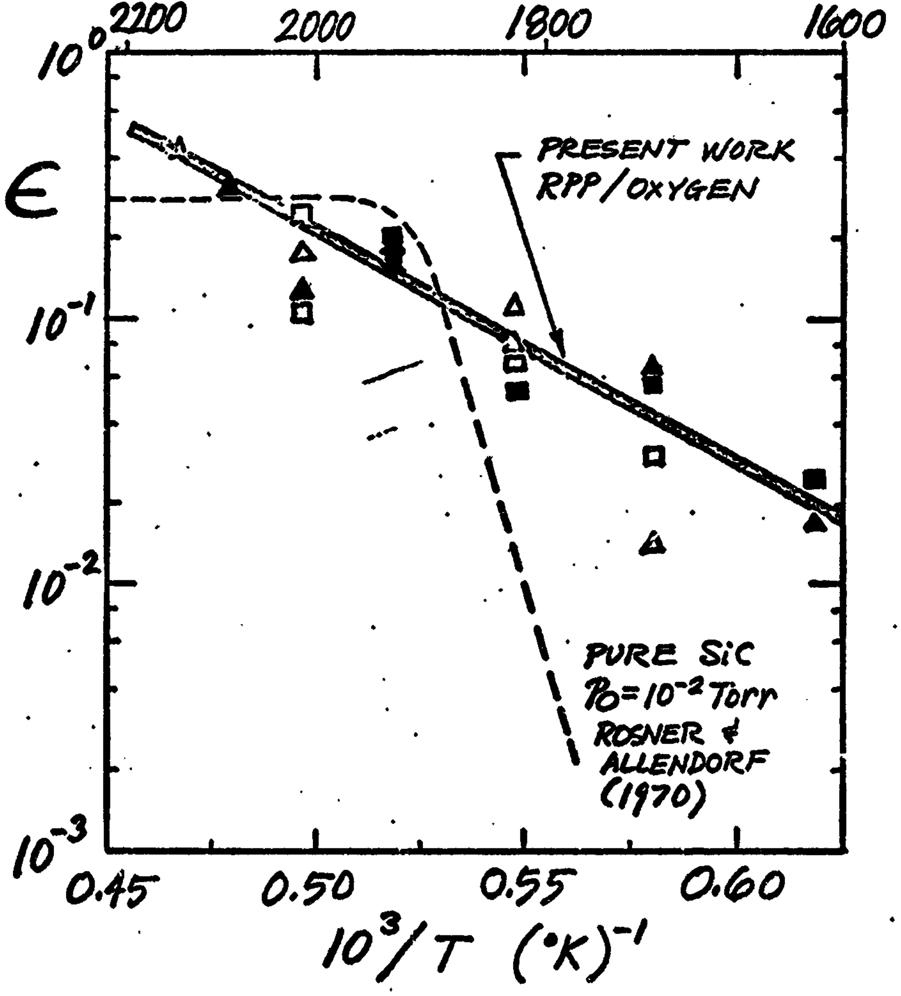

3.2-3 Dependence of oxidation probability of silicon carbide RPP coating on reciprocal temperature. ▲ , ■ = 0.12 torr; ▲, □ = 0.055 torr; ◘ , □ = O_2; ▲ , △ = O_2/O

Arrhenius diagram of these results is presented in Fig.3.2-3. It can be seen from the figure that no significant difference exists in the reaction probabilities for reactant pressures between 0.012 and 0.055 torr. Moreover, partial dissociation of the oxygen molecules does not significantly influence the reaction rates.

Comparison of the oxygen data with rate measurements on pyrolytic silicon carbide at 10^{-2} O-atom pressure [Rosner and Allendorf (1970a)] as shown in Fig.3.2-1 reveals a greater reactivity for the RPP coating below 1900K. Inasmuch as the data of Rosner and Allendorf agree reasonably well below 1900K with the maximum sublimation rate of SiO_2 according to the reaction

$$SiO_2(\text{condensed}) = SiO(g) + \frac{1}{2}O_2(g) \qquad (3.2\text{-}1)$$

it is apparent that the greater rate of RPP removal by reaction with oxygen is due to a mechanism other than sublimation of condensed SiO_2. Moreover, the RPP recession rate increases with oxygen pressure, rather than decreasing with oxygen pressure as was observed for pyrolytic SiC.

The comparison of RPP recession rates in oxygen and oxygen-nitrogen mixtures shows that addition of nitrogen has no influence on the rate of reaction below 1900K, but reduces the recession rate by a factor of 2-4 above 2000K. This behavior is exactly opposite to that observed for pyrolytic SiC [Rosner and Allendorf (1970b)], where N-atom addition suppressed the reaction rate below 2000K but had no effect above 2000K.

Figure 3.2-4 illustrates the results of stagnation arc jet tests on RPP coating by Vought Missiles and Space Company [LTV(1972)]. The stagnation pressure of the air reactant was 0.5 psia. Coating recession rates are presented for the Phase I coating which was prepared by placing a small amount of Al_2O_3 on the RPP surface and then coating in a 70% SiC, 30% Si pack at ca. 2000K. The phase II coating was prepared by coating RPP in a 60% SiC, 30% Si, 10% Al_2O_3 pack with no Al_2O_3 added to the RPP surface. Despite the large pressure differences between these arc jet tests and our studies at 10^{-2} torr pressure the recession rates on the Phase II material differ by no more than a factor of 3. Moreover, the Phase I material is seen to be less reactive below 2000K than the pyrolytic SiC [Rosner and Allendorf (1970a)] at an O-atom pressure of 10^{-2} torr. The decreased reaction rate for the Phase I material

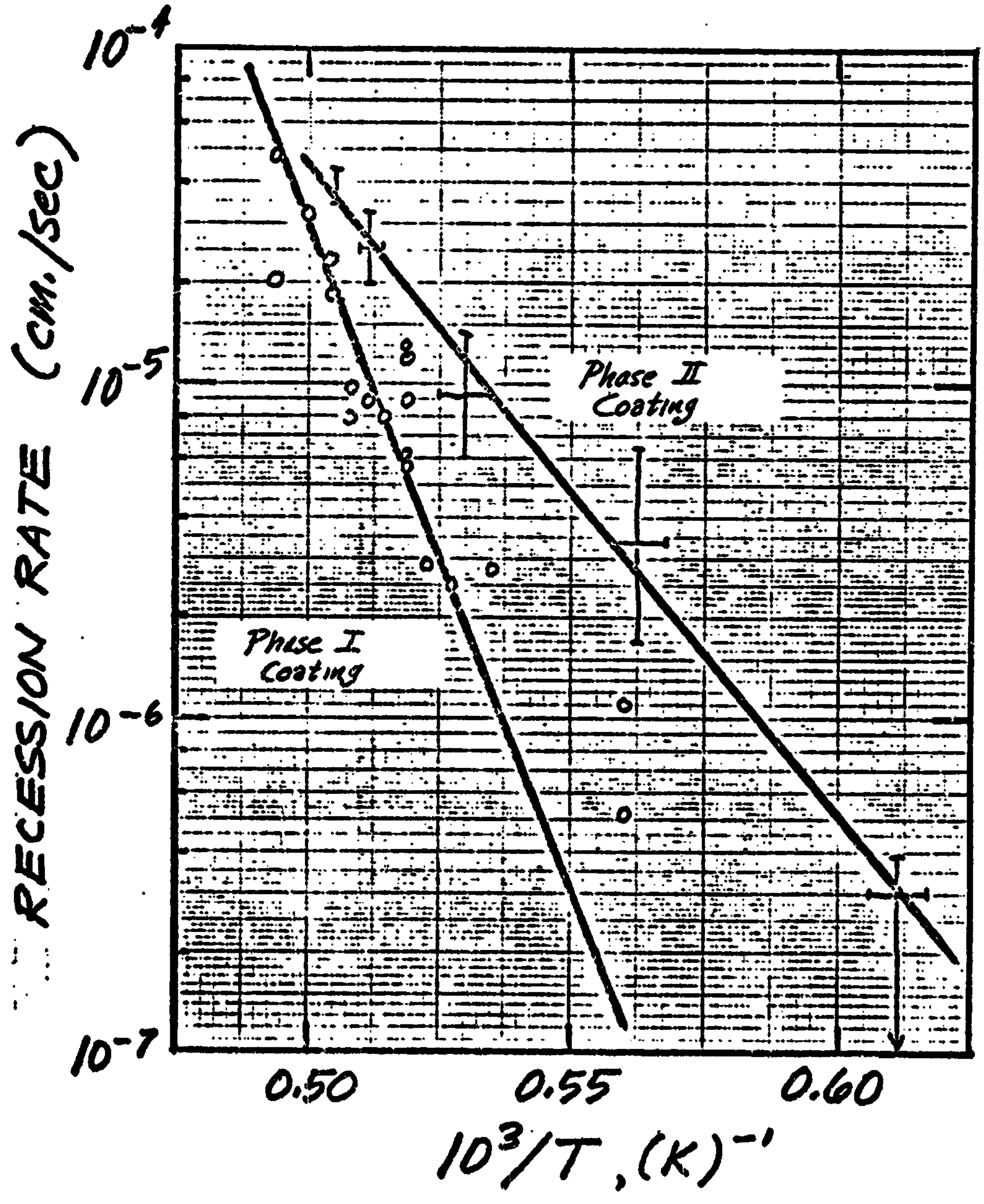

3.2-4 RPP coating recession rates in stagnation arc jet tests. ○ "Phase 1 " coating; + = "Phase 2" coating.

was attributed [LTV (1972)] to the short duration of their experiments. Phase II materials showed a time dependence of the recession rate with lower initial rates due to the increase in sample weight caused by formation of a condensed SiO_2 layer.

The nature of the surface after reaction is of considerable interest in the present study. At lower temperatures (<1700K) an adherent oxide film is formed which makes the measurement of changes in SiC coating thickness difficult. This problem was partially solved by lightly scraping off the adherent film. Fig. 3.2-5a shows micrographs of the surface and edge after reaction at 1618K for 4 minutes (Expt. No. 24A). Between 1700°K and 1900°K the protective film appears to melt. Glass-like particles are observed on the surface after cooling. The surface after reaction shows "islands" of glass-like particles dispersed on the coating surface as illustrated in Fig. 3.2-5b (Expt. No. 26). The size of the glass-like particles decreases as the temperature is increased. At temperatures above 1900 K neither the adherent oxide film nor the glass like particles are observed. Samples exposed at 2013K are illustrated in Fig. 3.2-5c (Expt. No. 18). Unreacted samples are illustrated in Fig. 3.2-5d.

The above observations apply equally to samples reacted with oxygen molecules or partially dissociated O_2/O mixtures. Similar observations were made for experiments in dissociated oxygen-nitrogen mixture except that the particles were observed at the highest temperatures. Glass-like particles were also observed for the two experiments in dissociated nitrogen at 1826 and 2013K. The surface of samples reacted in O_2 above 1800K, in N_2 at 2013K, and samples that were annealed in Ar for several minutes above 2000K were black, in contrast to the lighter appearance of samples reacted under other conditions. XPS analysis showed these black-colored samples to have much higher surface carbon than did the lighter colored samples. Formation of carbon probably occurs *via* the reaction

$$SiC(s) = Si(g) + C(s) \qquad (3,2\text{-}2)$$

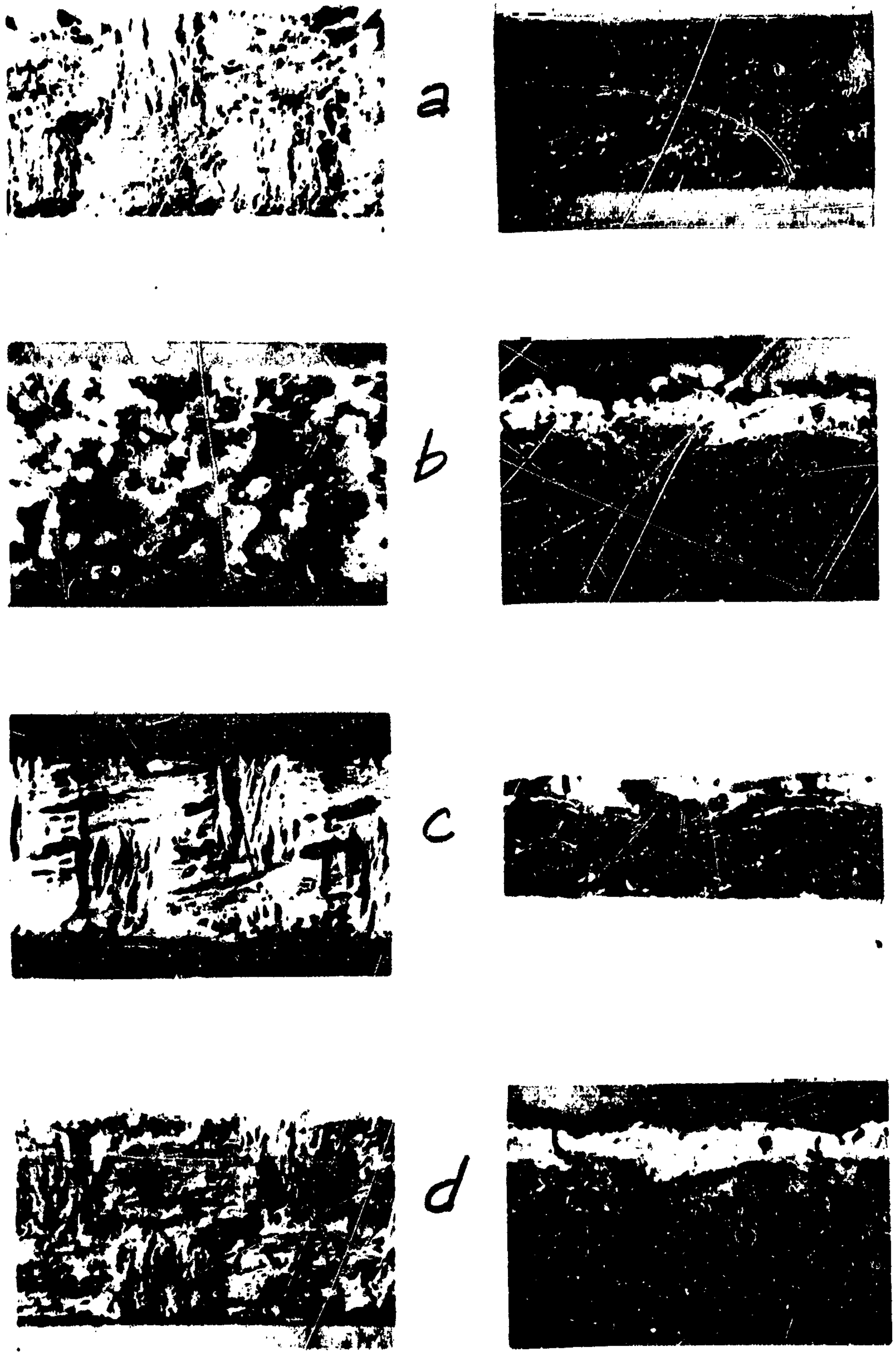

Fig. 3.2-5

for which the equilibrium Si pressure is ca. 10^{-4} torr at 1826 K. The reaction probability of O_2 with graphite [Rosner and Allendorf (1968)] is more than 10 times less than that for O-atoms above 1800K. Thus, the occurrance of carbon in experiments with O_2 but not with O-atom reactant is apparently due to the lower efficiency of O_2 molecules in removing carbon. Above 2290K, where the SiC decomposition pressure exceeds 10^{-2} torr, carbon should be found even in 10^{-2} torr of O-atom reactant. However, experiments were not performed at temperatures above 2140K. Two experiments (Nos. 54 and 58) in which the dissociated oxygen reactant gas was turned off before cooling the sample showed substantial carbon in the XPS study but did not appear black. It is therefore possible that a small amount of carbon forms on the surface above 1930K even in a dissociated oxygen environment and is removed by reaction with O-atoms if the sample is cooled in reactant. On the other hand, the carbon in these experiments may have formed after the oxygen was turned off but before the heating current was turned off.

3.3 Implications

The RPP coating and pyrolytic SiC recession rate measurements reported above strongly suggest that at least three mechanisms are responsible for RPP removal. The first is formation of a semi-protective condensed SiO_2 layer whose thickness depends upon its rate of formation and vaporization. This mechanism is most important at lower temperatures and higher pressures, where the vapor pressure of SiO(g) according to reaction 3.2-1. is smaller than the oxygen pressure so that condensed SiO_2 is formed. The second mechanism may occur at higher temperatures if the oxygen pressure is less than the decomposition pressure of SiC according to Eq.3.2- . Then silicon is removed by decomposition of SiC and a carbon layer (which inhibits

SiC decomposition) is formed, whose thickness depends on the reactant/carbon reaction probability and pressure of reactant gas. These first two mechanisms occur for both pyrolytic SiC and RPP coating. The third mechanism is the physical loss of oxidized particles, which occurs only for RPP coatings. This mechanism suggested by the observation of loosely adherent particles on RPP coating surface at temperatures above 1700K and by the fact that RPP recession rates exceed the maximum possible recession rates for the first two mechanisms. This is shown graphically in Fig. 3.3-1 which plots the equilibrium decomposition vapor pressure of Si over SiC, and the equilibrium vapor pressure of SiO over SiO_2 at 10^{-2} or 5.6^* torr O_2 pressure. Also shown is the total vapor pressure which is developed by the reaction

$$SiC(s) + 2SiO_2(\text{condensed}) = 3SiO(g) + CO(g) \qquad (3.3\text{-}1)$$

The reason that oxidized particles may be lost by the RPP coating but not by the pyrolytic SiC is probably related to the following three observations. First, as shown in Fig. 3.3-1 reaction of a protective SiO_2 coating with the SiC substrate can, in the absence of O_2, develop high pressures at the coating - SiC interface.$^+$ Second, the RPP coating density is half that of pyrolytic SiC. Third, the RPP coating contains significant amounts of Al_2O_3 (see Section 4) which lowers the melting point of SiO_2 from 1996 to 1868K [Levin, et al. (1964)].

Thus, loss of SiO_2 from RPP coating may be due to the force exerted by the vapor produced by reaction of SiO_2 with SiC on areas where the SiO_2 coating covers voids in the RPP coating. The absence of this loss in pyrolytic SiC oxidation may be due to the absence of voids and by the possibly stronger adherence of SiO_2 films which are free of Al_2O_3.

---

* The approximate oxygen pressure in the stagnation arc jet tests[LTV,1972].

\+ Si(1) may form at a protective $SiO_2(1)$ - SiC(s) interface at T > 2000K where the equilibrium constant for the reaction SiO(g) + SiC(s) = 2Si(1) + CO(g) exceeds 0.33, the CO/SiO pressure ratio fixed by reaction 3.3-1.

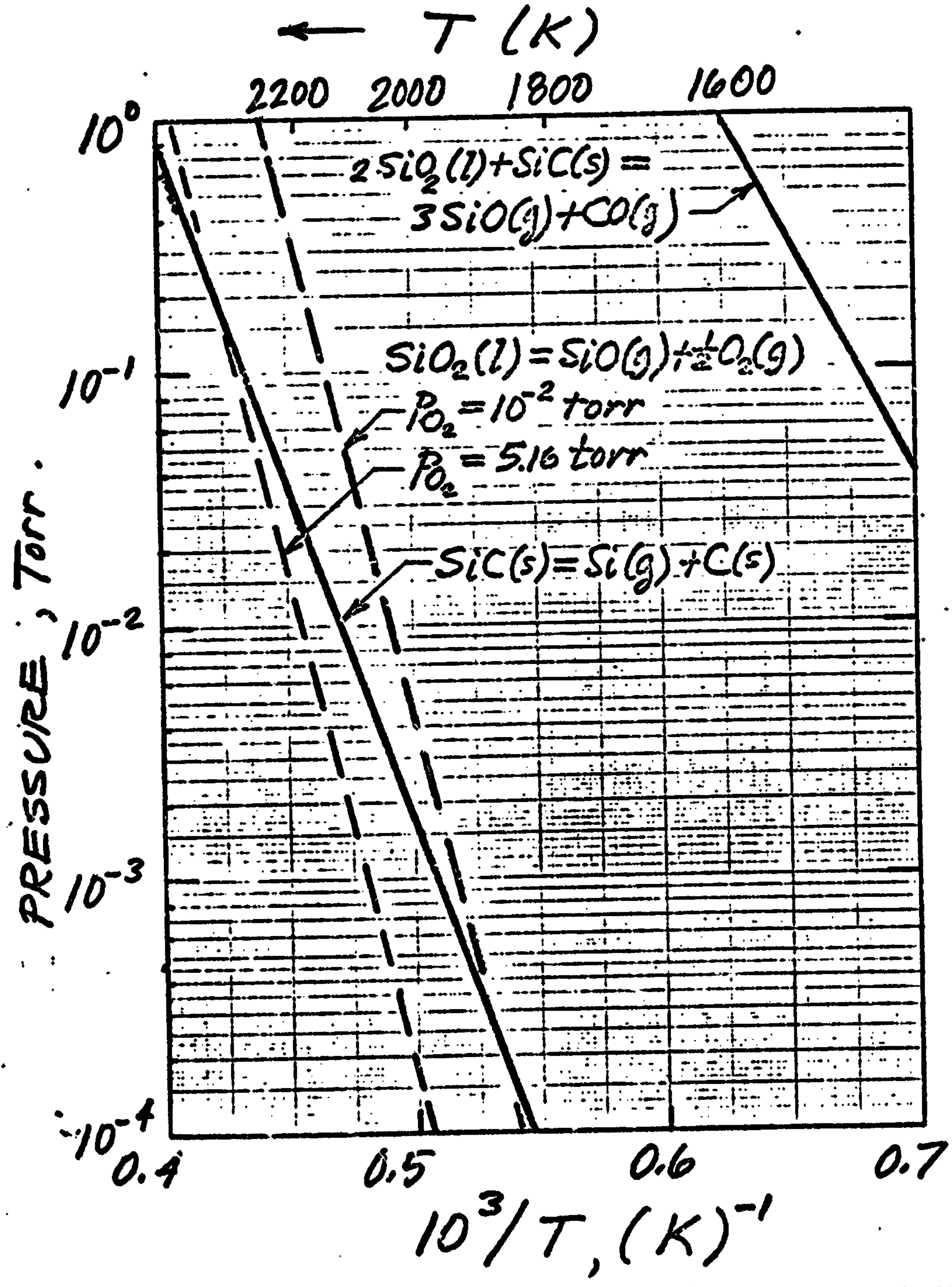

3.3-1 Vapor-condensed phase equilibrium pressures in the SiC-SiO_2-O_2 system.

4. SURFACE CHARACTERIZATION STUDIES

4.1 X-ray Photoelectron Spectroscopy

4.1.1 Technique

In order to understand why a given surface has a particular γ or why γ changes on a surface, one must probe the details of the chemistry and structure of the sample surfaces. The information needed is difficult to obtain, but a relatively new technique, X-ray photoelectron spectroscopy (XPS) or ESCA (electron spectroscopy for chemical analysis) [Seigbahn, *et al.* (1967)], has broad applicability to the problem. The principle of the experiment is simple (see Fig. 4.1-1). X-rays usually Mg-$K\alpha_{1,2}$ (1254 eV) or Al-$K\alpha_{1,2}$ (1487 eV), approximately 0.7 to 1.0 eV line width, impinge on a sample and the ejected photoelectrons are energy analyzed in a high resolution spectrometer. The number of electrons recorded versus kinetic energy constitutes the XPS (ESCA) spectrum. Intensity maxima which occur in the spectrum correspond directly to the various bound electron energy levels in the sample, and peak positions (kinetic energy) can be used to calculate electron binding energies. Comparison of measured binding energy to tabulations of binding energies for the elements usually allows ready identification of peaks. Exact binding energies, however, depend on the charge distribution in the sample (oxidation states) and *chemical shifts* in binding energy can be used to identify the chemical state of an element (ie. Si from SiO_2). Peak areas are determined by the cross-section for photoemission from the energy level in question, the concentration of the element present in the sample, and the electron escape depth. In principle, areas can be used for *quantitative analysis*. All elements but hydrogen can be seen by the technique. Additional

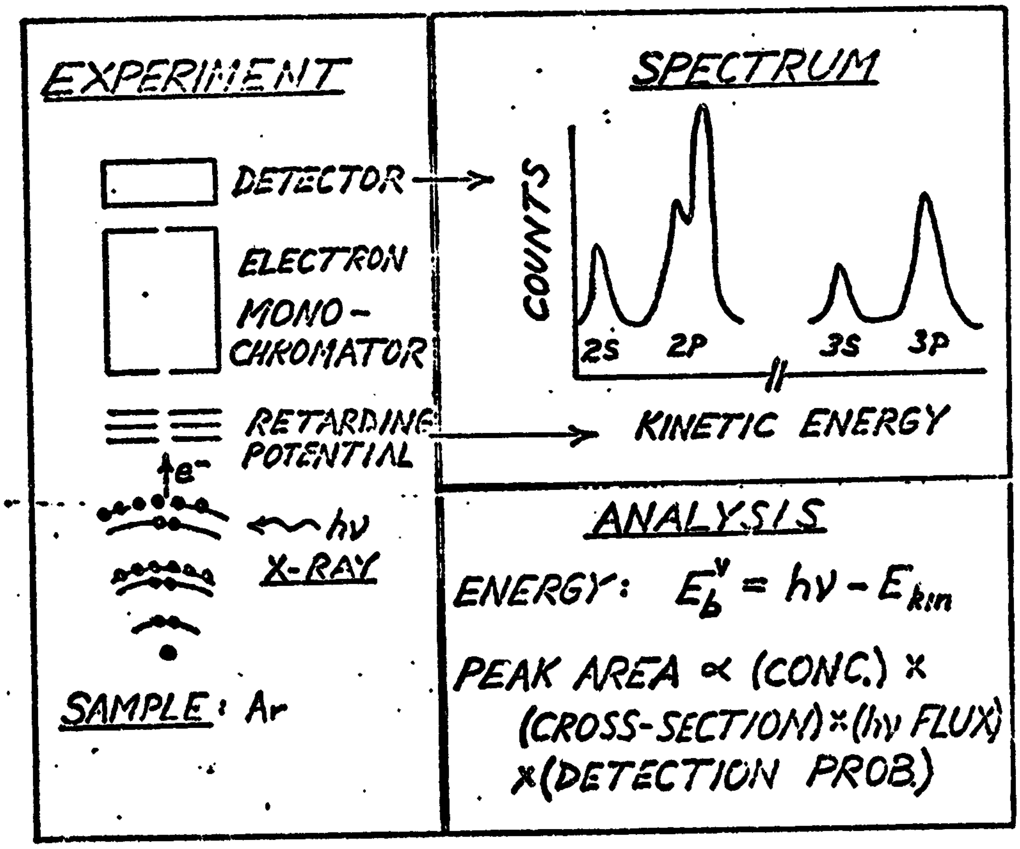

4.1-1 Schematic of the X-ray photo-electron spectroscopy experiment and data analysis.

information is sometimes available from peak shape and peak splitting. This is described in many detailed reviews now in the literature [eg. Carlson (1972), Hercules (1972)].

Since the range of 1 KeV X-rays in solids is relatively long, the depth of the solid which is sampled in X-ray photoelectron spectroscopy is determined by the inelastic mean free path, λ_e, of the emitted photoelectrons (see Fig. 4.1-2). In principle, λ_e depends on the sample material and passes through a minimum as a function of electron kinetic energy [Quinn (1962), Baer et al. (1971)]. Accurate values for λ_e as a function of material and electron kinetic energy are not generally available but the most recent numbers obtained for 10-1400 eV electrons scattered from densely packed solids range from 5 to 40Å, with the average about 20Å, clearly indicating the potential of this technique for the study of surfaces. Siegbahn et al. (1967) showed that the sensitivity of the technique was sufficient to observe monolayer quantities of iodostearic acid. In the past year a number of additional papers have appeared demonstrating in more detail the utility of this method for surface work. Brundle and Roberts (1972) have observed Hg on Au at coverages as low as 0.002 monolayers and recorded C(1s) and O(1s) lines from gases physically adsorbed on Au at low temperature. Kim and Davis (1972) revealed a wealth of surface chemistry during the oxidation of Ni and Madey and Yates (1973) showed a chemical differentiation, on the basis of XPS chemical shifts, of the α and β states of CO adsorbed on W+. Recent work at Yale has shown sensitivity of the XPS technique to 0.02 monolayers of Cs on Mo and has clearly demonstrated that the angular dependence of spectra is an important aid in accentuating and identifying spectral characteristics of the surface itself [Fraser, Florio, Delgass, and Robertson (1973)]. A second

---

+ Recently, two different chemical states of adsorbed oxygen have been found by Barber et al. (1973) after exposure of the basal plane of graphite to O atoms

SOLIDS

ENERGY: $E_b^F = h\nu - E_{kin} - \phi_{SP}$

PEAK AREA: INFLUENCED BY e^- ESCAPE DEPTH

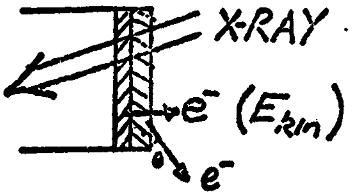

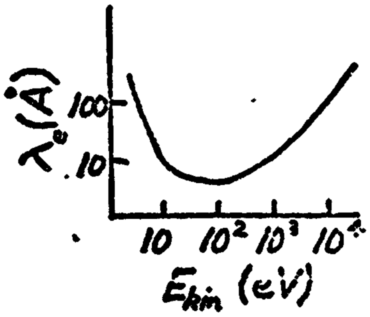

MATERIAL	E_{kin} (eV)	λ_e(Å)
IODOSTEARIC ACID [a]	860	<100
C [b]	950	15
	1170	18
Ag [c]	70	4
	360	8
Au [d]	1200	22

4.1-2 Inelastic mean free path of emitted photo-electrons for various sample materials paper by the same authors shows the utility of Ar ion cleaning for removing overlayers of surface contamination. Removal of hydrocarbon contamination (present on nearly all samples as a result of handling or deposition during measurements at moderate vacuum) generally results in significantly enhanced substrate peak intensities. Use of ion bombardment on multicomponent samples have some uncertainties because some elements may be removed perferentially, but it may be valuable in differentiating samples which have composition gradients in depth. A more complete literature review is given in QPR-1.

A particularly important problem that arises in application of this technique to insulators is that of charging. This occurs when the conductivity is not sufficiently high to allow a ready supply of electrons from ground to fill the positive holes generated by the photoemission. Since charging results in an apparent shift of a spectral line, it must be measured or eliminated in order to record true chemical shifts. Early in this work it was found that by use of small samples, sometimes covered by a high transmission tungsten grid, spectra of insulators could be obtained on both the Fraser et al spectrometer and the commercial Hewlett Packard Spectrometer made available to us by the Chemistry Dept., but charging could not be eliminated. In the last two months of this program, the Hewlett Packard Device was fitted with an electron flood gun which neutralized positive surface charge from above and yielded more reliable.

To summarize, XPS is a powerful tool for the study of surfaces. Chemical shifts can give the chemical state of the sample surface and peak areas a quantitative analysis. The angular dependence of the spectrum and spectral changes after argon ion cleaning may be used to differentiate surface from bulk species. All of these aspects of the technique have been applied to studies of the TPS materials, but emphasis has been placed on elemental analysis of the surface layers. The primary goals are the correlation of γ with surface composition and investigation of the stability of surface composition as a function of various treatments.

4.1.2 Results and Discussion of XPS Experiments

A. Calibration Compounds. Although, as reported in QPR-1, a number of XPS studies on compounds of interest in this work have appeared in the literature, needed intensity ratios where often not reported and uncertain charging effects make binding energies unreliable. Since nearly all experiments were done on the Hewlett Packard spectrometer [made available by a grant to the Chemistry Department by the National Science Foundation (GP - 36553)] calibration data were also obtained on that machine. The compounds, primarily obtained from ROC/RIC[1] were analyzed as received. Mullite ($3Al_2O_3 \cdot 2SiO_2$) and aluminum silicide (AlSi) were studied to obtain the relative photoelectron cross section for silicon vs. aluminum. Silicon carbide (SiC), silicon dioxide(SiO_2), silicon nitride (Si_3N_4)[2] and silicon oxynitride (Si_2ON_2)[2] yielded the binding energy difference between the Si(2p) peak and the oxygen, carbon or nitrogen 1s lines. Except for SiC and SiO_2,powder compounds were dusted on doublesided scotch tape mounted on the specimen holder. Because of the tape background, a comparison of the intensities of carbon or oxygen with silicon is not meaningful for such samples and hence not reported. The results of XPS analyses of the calibration compounds are listed in Table 4.1-1.

The Table reiterates that the surface purity of materials is difficult to control. Mullite and quartz gave clean spectra with identical Si(2p) - O(1s)

---

[1] Research Organic/Inorganic Chemical Co., Sun Valley, Calif.

[2] Courtesy of Mr. M. E. Washburn, Norton Company, Worcester, Mass.

Table 4.1-1

XPS Analysis of Calibration Compounds

Compound	Obs. Binding Energies (eV)					Energy Separations (eV)			Peak Area Ratios			
	Si(2p)	Al(2p)	C(1s)	N(1s)	O(1s)	C-Si	N-Si	O-Si	Al/Si	N/Si	O/si	C/si
AlSi	98.3 101.4	73.8	-	-	531.0	-	-	432.7 429.6	0.39	-	-	-
Mullite ($3Al_2O_3 \cdot 2SiO_2$)	101.6	73.2	-	-	531.0	-	-	429.4	1.32	-	-	-
SiC	99.6	-	281.4	-	531.0	181.8	-	431.4	-	-	1	1.1
SiO_2 (Quartz)	102.3	-	-	-	531.7	-	-	429.4	-	-	10	-
Si_2ON_2	101.5	-	-	397.0	531.4	-	295.5	429.9	-	2.0	-	-
Si_3N_4	100.8 101.5	-	-	396.3	531.0	-	295.5	429.5	-	~2.0	-	-

separations. The silicon carbide samples (Matheson) showed a small amount of oxygen but a single Si(2p) line. The C(1s)/Si(2p) area ratio of 1 was taken as representative of SiC. The SiO_2 - SiC separation was confirmed by 3.0 eV splitting measured for the Si(2p) line from a physical mixture of SiC and quartz. A plasmon loss line*at 23 eV from the parent peak was significnatly larger for SiC than SiO_2 and provided a second, more qualitative differentiation of the two compounds.

Data for Si_2ON_2 are consistent with those for the other oxidized Si compounds and no evidence of surface heterogeneity appeared. This was not the case for Si_3N_4. A splitting in the Si(2p) line indicated presence of SiO_2 or Si_2ON_2. Because of the uncertainty of the curve resolution, clear differention of Si_2ON_2 and Si_3N_4 is not possible at this time. Since the parameters for N containing compounds are between those for SiC and SiO_2, differentiation of a mixture of all compounds on the basis of chemical shift would require computer fitting of data.

The mullite data provides an Al(2p)/Si(2p) area ratio of 1.32 which represents a relative atomic cross-section ratio of 0.44 if electron escape depths for the two peaks are assumed identical. This is the value used to estimate Al content of TPS surfaces. Binding energies for the AlSi surface show a mixture of Al_2O_3, SiO_2 and Si, but no unoxidized Al. Thus, it appears that the oxidized surface of this component undergoes phase separations.

It should be noted that even with use of the flood gun absolute binding energies may vary by ± 0.3 eV due to charging. Thus peak separations are the most reliable energy parameters. A number of uncontrollable experimental variables make absolute peak intensities unreliable and thus only peak intensity ratios are reported.

---

* A plasmon loss line is due to the discrete energy loss of photoelectrons by collective excitation as they leave the solid.

B. RSI Coating (Lockheed 0042)

Fresh: The fresh Lockheed 0042 coating is Corning 7740 borosilicate glass with small amounts of silicon carbide as emittance agent. XPS analysis of the fresh material indicated only silica. No silicon carbide or boron were observed.

Arc Jet Tested: A number of arc jet tested Lockheed RSI coatings were received and examined by XPS. While the surfaces consisted mainly of silica, six of the thirteen samples also contained Al_2O_3* as a contaminant. Conditions of arc jet testing and Al(2p)/Si(2p) peak height ratios are listed in Table 4.1-2. An estimate of the Al/Si atom ratio may be obtained by dividing the area ratios in Table 4.1-2 by 0.44. In general, for samples containing alumina the amount of alumina present on the surface increased with increasing surface temperature, and increased exposure time, but note the exception of one specimen, where a high concentration of alumina was observed at a low surface temperature. Although Al(2p), Al(2s) binding energies are nearly the same as those of the Cu(3p), Cu(3s), differentiation is clear in the Cu($2p_{3/2}$, $2p_{1/2}$) region of the spectrum. In Table 4.1-2 assignment of contaminant peaks to alumina* is firm, but the origin of the contamination is unknown.

One sample designated LMSC-LI-30-1800, obtained from the NASA-AMES Research Center, was known to be contaminated with copper (Goldstein 1973). XPS analysis of this sample clearly showed copper. Moreover, the structure of satellite lines associated with Cu($2p_{3/2,1/2}$) peaks indicated that most of the copper present in the sample was in the form of Cu^{2+}.

γ-Measurement Samples: XPS analysis of samples, exposed to O_2 at ca. 1270K in γ-reactor, showed only SiO_2 and there was no change in surface chemistry before and after reaction. RSI Samples exposed to O + N atom mixture or ca. 1490K showed the presence of nitrogen incorporation (N1s)/Si(2p) = 0.05) besides SiO_2. The presence of nitrogen may be due to Si_3N_4, Si_2ON_2 or dissolved nitrogen.

C. RPP Coating

Fresh: The surface of fresh RPP Coating contained mainly SiC with some silica and alumina. The alumina content of the surface is characterized by the $Al(2p)/Si(2p)_{tot}$ peak height ratio as listed in Table 4.1-3.

---

* Note: cannot distinguish alumina from aluminosilicate. Oxidized aluminum is designated Al_2O_3 for convenience.

Table 4.1.2

Arc Jet Tested RSI Specimens

Specimen #	Model type & Number	$\frac{Al_{2p}}{Si_{2p}}$	Cycles	Surface Temp. °K	Avg. Stream Enthalpy BTU/Lb	Pressure Torr	Source	Remarks
1	LMSC-LI-1500	0	1	1450	1890	2.4	Murray(1)	
2	LMSC-LI-900	0	1	1422	2000	1.6	"	
3	LMSC-LI-900	0.1	1	1255	1180	1.7	"	
4	LMSC-LI-900	0	1	1643	3460	1.6	"	
5	LMSC-LI	0.13	35	1643			Leger(1)	SEM
6	LMSC-LI-1542	0.18	22	1367-1478	6000	4.55	Goldstein(2)	SEM
7	LMSC-LI-30-1800	Cu	1	1260			"	SEM
8	TT 145-4	0.05	1	1644		5.4	C. Scott(1)	
9	TT 129-2	0.06	1	1572		6.0	"	
10	TT 145-3	0.17	1	1700		6.0	"	SEM
11	TT 129-3	0	1	1295		6.0	"	SEM
12	TT 145-5	0	10	1290		6.0	"	SEM
13	TT 113-10	0.11	10	1575		6.5	"	SEM

---

(1) Johnson Spacecraft Center, Houston, Texas

(2) Ames Research Center, Moffett Field, California

Table 4.1-3

Al_{2p}/Si_{2p} Ratio in Fresh RPP Coating

Specimen	$Al(2p)/Si(2p)_{total}$
M130-26	0.1, 0.04
M169-3	0.12
M171-7	0.15
M170-HT	0.1

The average value of 0.1 for the $Al(2p)/Si(2p)_{tot}$ ratio of the fresh RPP coating will be used for comparison with specimens after various treatments.

High Temperature Oxidized and Nitrided Specimens From Mass Loss Experiments: In the earlier stages of this project, the specimens were quenched from mass loss test temperature to room temperature in the reactant gas stream. Later this procedure was modified so that the reactant gas stream was replaced with an argon stream at the end of reaction and the samples were quenched in the argon stream.

Exposure to Dissociated Oxygen: The XPS results of the specimens after reaction with partially dissociated oxygen at temperatures from 1410°K to 1930°K are summarized in Table 4.1-4. C(1s) peak heights for free carbon were obtained directly from the free carbon line when it was well resolved or by subtracting from the total C(1s) peak the amount of carbon that was locked up as SiC (assuming that the cross section for C and Si are the same; see Section 4.1-2A).

The samples quenched in argon or in dissociated oxygen from relatively low temperature (< 1620°K) exhibited similar surface chemistry.

Table 4.1-4

XPS Results of Mass Loss Specimens, Reaction with Dissociated Oxygen

Expt. No.	Temp K	pO_2 ($x10^{-2}$torr)	Time Sec	$\left(\frac{SiC}{Si_{2p}}\right)_{tot}$	$\left(\frac{SiO_2}{Si_{2p}}\right)_{tot}$	$\frac{Al_{2p}}{Si_{2p}\ tot}$	$\frac{Free\ C_{1s}}{Si_{2p}\ total}$	$\frac{O_{1s}}{Si_{2p}\ tot}$	Remarks, impurities
The following specimens are quenched in argon after reaction									
55	1618	5.90	180	0	1	0.15	0.6	9.5	Ca
54	1930	5.65	360	1	0	0	45.0	1.0	
The following specimens are quenched in dissociated oxygen									
7	1410	1	600	0	1	0.11	0.2	11.0	
8	1618	1	300	0	1	0.11	0.4	7.75	Au(from sample backing)
46	1722	6.15	420	0.75	0.25	0.3	0.1	4.0	
1	1830	1	1200	0.72	0.28	0.04		5.5	
2	1826	1	900	0.62	0.38	0.11	0.1	5.0	
9	1830	1	600	0.75	0.25	0	0.1	2.0	
28	1930	1	600	0.69	0.31	0	0.2	6.9	
29	1930	1	200	0.64	0.36	0.03	0.2	10	
10	1930	1	300	0.61	0.39	0	0.1	5.4	
The following are the loosely adherent powder from the sample									
1*	1830	1		0.7	0.3	0.05			

* Powder is sprinkled on to aquadag.

The sample surface consisted mainly of SiO_2 with alumina concentrations nearly the same as that of fresh material.

The surface chemistry of samples quenched from higher temperatures depended on whether they were quenched in argon or in dissociated oxygen. The surface of a sample that was quenched in argon after reaction at 1930°K contained a substantial amount of free carbon on the surface. Minor amounts of SiC were also present. The surfaces of samples quenched in dissociated oxygen, however, consisted of a mixture of SiC and SiO_2 and contained very little free carbon. The concentration of alumina on the surface was very small in samples quenched from high temperature and did not depend upon the method of quenching.

The dissociative vaporization of SiC ($SiC(c) \rightarrow Si(g) + C(c)$, and SiO_2 ($SiO_2(l) \rightarrow SiO(g) + \frac{1}{2} O_2(g)$) are plotted in Figure 3.3-1. At 1930K the vapor pressure of Si(g) is substantial (10^{-3} torr). Hence during reaction at high temperature and low pressure the surface is likely to be bare of any protective oxide film. This is in accordance with the results reported by Rosner and Allendorf (Rosner 1970). We have found that at this temperature SiC tends to lose silicon and form a carbon rich layer when heated in argon. Thus, the observed high concentration of carbon of the samples quenched in argon is taken as due to the dissociative vaporization of SiC(s). When the samples are quenched in dissociated oxygen they can undergo partial oxidation as the temperature decreases and form a stable SiO_2 film. One would then expect that surfaces quenched in O should consist of SiC and SiO_2 at room temperatures. Our XPS results are in accordance with this hypothesis. The oxidation probability of carbon is also high (> 0.2) in atomic oxygen [Rosner and Allendorf(1968)] above 1000K so very little free carbon is left after quenching in dissociated oxygen.

Exposure to Undissociated Oxygen Molecules: The XPS results for O_2 experiments are summarized in Table 4.1-5. The surface of the sample quenched in argon after reaction at 1930°K consisted mainly of carbon and SiC. This result is similar to that after reaction with dissociated oxygen. The spectra of samples quenched in oxygen were too weak to allow quantitative interpretation. At 1722°K, the surface consisted of SiC, SiO_2. Minor amounts of free carbon were also observed. The surfaces of samples after reaction at 1930°K, 2013°K show a substantial amount of free carbon. Although in Expt. 16, part of free carbon observed may be associated with the gold backing, the results indicate that the oxidation of carbon in oxygen molecules is not as fast as in atomic oxygen. This is again in accord with the findings of Rosner and Allendorf (1968). They report that the oxidation probability of graphite is at least an order of magnitude smaller in molecular oxygen compared to oxygen atoms.

Exposure to Dissociated and Undissociated Nitrogen: XPS results for these experiments are shown in Table 4.1-6 . The surface of the sample reacted with undissociated nitrogen at 2013 °K (quenched in argon) consisted of carbon and minor amounts of silicon. No nitrogen was observed. The binding energy value of Si(2p) peak and a smaller value of O(1s)/Si(2p) suggest that the silicon present is probably in the form of SiC. The absence of any silicon nitride indicates either that there is no reaction between silicon carbide and molecular nitrogen or that any silicon nitride formed vaporized during quenching. Rosner and Allendorf (1970) report that the reaction of SiC with molecular nitrogen is negligibly slow.

Exposure to dissociated nitrogen at 1826°K (and cooled in dissociated nitrogen) led to a significant incorporation of nitrogen in the surface.[†] Although the binding energy differences between Si_{SiC}, $Si_{Si_3N_4}$, $Si_{Si_2ON_2}$ are very small, the high value of N(1s)/Si(2p) and the small value of $C(1s)_{SiC}$

[†] Our XPS data also reveal that atomic nitrogen is effective in removing the free carbon formed upon SiC thermal decomposition (see the free C_{1s}/Si_{2p} ratio for runs 48, 56; cf. run 54). This is consistent with the finding of Rosner and Allendorf (1970a) that N atoms react efficiently with SiC, but not efficiently with pure graphite.

Table 4.1-5

XPS Results of Mass Loss Specimens Reaction with Undissociated Oxygen

Expt. No.	Temp K	pO_2 (10^{-2} torr)	Time sec	$(\frac{SiC}{Si_{2p}\ tot})$	$(\frac{SiO_2}{Si_{2p}\ tot})$	$\frac{Al_{2p}}{Si_{2p}\ tot}$	$\frac{\text{Free } C_{1s}}{Si_{2p}\ tot}$	$\frac{O_{1s}}{Si_{2p}\ tot}$	Remarks impurities
The following are quenched in argon									
53	1930	5.60	360	1	0	0	45.0	1.0	
The following are quenched in oxygen									
22	1722	5.4	180	0.5	0.5	0.1	0.9	8.7	see note
30	1930	1.25	600	1	0	0.02	7.2	1.4	see note
16	2013	1.32	360			0	30.0	13.3	Au backing (see note)

Note: The values indicated are approximate.

Table 4.1-6

XPS Results of Mass Loss Specimens Reaction with Nitrogen

Expt. No.	Temp. K	pN_2 (Torr)	Time (sec)	$\frac{Al_{2p}}{Si_{2p}}$	$\frac{N_{1s}}{Si_{2p}}$	Free C_{1s}/Si_{2p}	$\frac{O_{1s}}{Si_{2p}}$	Remarks
The following specimen was reacted with undissociated nitrogen and cooled in argon								
57	2013	0.55	600	0.5	0	100	1.0	Silicon is probably in the form of SiC
The following specimens were reacted with dissociated nitrogen								
48	1826	0.57	300	0.24	2.3	1.7	6.4	Cooled in dissociated nitrogen. Major amount of silicon is in the form of Si_3N_4, $SiON_2$
56	2013	0.55	600	0	1.16	13.8	1.7	Cooled in argon

indicate that most of the silicon observed was in the form of Si_3N_4 or Si_2ON_2 (approximately 75%). It is not possible to differentiate between the nitride and oxynitride.

Reaction with dissociated nitrogen at *ca.* 2000°K produced a lesser amount of nitrogen in the surface. There was also substantial increase in the free carbon. The small amount of nitrogen can be ascribed to increased volatility of silicon nitrides at the higher temperature. Since the sample was quenched in argon, formation of nitrides at lower temperatures was prevented but some free carbon was generated.

Exposure to Dissociated Oxygen - Nitrogen Mixture: The XPS results for these samples are summarized in Table 4.1-7. The results are comparable to those after reaction in dissociated oxygen except for the presence of nitrogen incorporated in the surface in certain cases. Reaction with O + N mixture up to 1620°K produced an essentially silica surface with no nitrogen. This behavior was independent of the method of quenching and indicated that oxidation is more favorable than nitridation at temperatures below 1620°K

At temperatures above 1620°K, the observed surface chemistry depended on the method of quenching. After argon quenching the surfaces of specimens reacted with the O + N mixture at temperatures 1720 - 1820°K consisted of silicon carbide, nitrides or oxynitride. No SiO_2 was observed. In one specimen (Expt. No. 61) a significant increase in alumina was observed. After 2000°K only free carbon and small amounts of SiC were present.

The surfaces of samples quenched in reactant gas mixtures after reaction at temperatures above 1620°K, consisted of SiC, SiO_2 and various amounts of incorporated nitrogen. Note that sample #38 showed only SiO_2 and no nitrogen Two other samples reacted under similar conditions failed to confirm this isolated behavior.

An attempt was made to collect condensed vapor on a Ta plate downstream from the specimen. XPS analysis showed that the condensate was mainly silica.

Table . 4.1-7

XPS Results of Mass Loss Specimen Reaction with Dissociated Oxygen and Nitrogen

Expt. No.	Temp	pO_2 ($x10^{-2}$torr)	pN_2 (torr)	Time sec	$\left(\frac{SiC+Si_3N_4+Si_2ON_2}{Si_{2p}\ tot}\right)$	$\frac{SiO_2}{Si_{2p}\ tot}$	$\frac{Al_{2p}}{Si_{2p}\ tot}$	$\frac{N_{1s}}{Si2p_{tot}}$	$\frac{Free\ C_{1s}}{Si2p_{tot}}$	$\frac{O_{1s}}{Si2p_{tot}}$	Remarks, impurities
The following are quenched in argon											
59	1618	1.18	0.56	1200	0	1	0.16	0	0.2	11.0	Ca
60	1722	0.90	0.43	900	1	0	0.04	0.2	0.4	1.3	Majority of Si is SiC*
61	1826	1.15	0.55	720	1	0	0.26	0.2	2.0	3.0	"
58	2013	1.16	0.55	600	1	0	0	0	25.7	1.0	"
62	2013	1.17	0.56	600	1	0	0	0	56.0	1.0	"
The following are quenched in dissociated oxygen-nitrogen mixture											
36	1410	1.17	0.55	1800	0	1	0.02	0	0.3	10.0	
37	1618	1.20	0.57	1200	0	1	0.13	0	0.6	10.5	Ca, Au
41	1722	1.31	0.60	900	0.67	0.33	0.01	0.2	0.2	3.0	Au
38	1826	1.25	0.57	720	0	1	0	0.02	0.45	9.5	
44	1826	1.35	0.60	600	0.69	0.31	0	0.2	0.2	4.2	
45	1826	1.28	0.6	600	0.68	0.32	0.05	0.1	0.2	6.0	
40	1930	1.14	0.53	900	0.65	0.35	0.04	0.12	0.2	5.0	
39	2013	1.39	0.62	600	0.66	0.34	0	0.26	0.3	3.9	
42	2013	1.30	0.60	900	0.69	0.31	0.01	0.21	0.2	4.2	
The following is the condensate downstream collected on a Ta plate (quenched in reactant)											
44C	1826	1.35	0.60	600	0	1	0	0	0.14	9.6	Au

* This is deduced from C_{1s}/Si_{2p} ratio

The XPS results obtained with nitrogen - oxygen mixtures are consistent. There is evidence for nitrogen incorporation in the surface at temperatures above 1720K. At temperatures above 1820K, the results suggest appreciable loss of nitrides or oxynitrides by dissociation ($Si_3N_4(c) \rightarrow 3Si(C) + 2N_2(g)$) or oxidation ($Si_3N_4 + 3O_2 \rightarrow 3SiO_2 + 2N_2$). For specimens quenched from high temperature in the reactant mixture, the incorporation of nitrogen may occur at lower temperature. The silicon oxidation behavior is similar to that in dissociated oxygen. The results are not precise enough to differentiate Si_2ON_2 from SiC or Si_3N_4)

Arc Jet Tested RPP Samples

The surface chemistry of three arc jet tested samples showed a wide variation in spite of similar arc jet test conditions(1). The surface of sample M130-25 consisted mainly of alumina with small amounts of SiO_2. The surfaces of the other two specimens showed equal amounts of silica and Al_2O_3. The concentration of alumina was higher than that of fresh RPP material by a factor of 4.

1.	Specimen	Surface Temp °K	Avg. Stream Enthalpy BTU/lb	Cycle	$\frac{Al_{2p}}{Si_{2p}}$
	M130-25	1894	6900	1	2.4
	W18-11-1	1916			0.4
	W18LE60-1	1905			0.4

Surface Concentration of Alumina as a Function of Treatment: As shown in Table 4.1-3, the Al(2p)/Si(2p) peak height ratio was about 0.1 for fresh RPP coating. Reaction with oxygen and O + N mixture at temperatures 1620-1820K in the mass loss reactor did not change this ratio appreciably. However, after γ-measurements at 1820K with N + O, the ratio increased by a factor of 4. Reaction with N also increased this ratio to 0.24 at 1820K in mass loss reaction and 0.52 at 1720K in the γ-measurement reactor. Plasma arc jet tests in air at 1900K also produced a surface rich in alumina.

Higher temperature (above 1820K) generally resulted in a very small value Al(2p)/Si(2p). At low temperature of 1410°K, again a small value was observed (Sample #36, Table 4.1-7)

Youngblood (1972) reported that the majority of alumina is restricted to the first 20μm from the surface, and concentration at the surface is higher than in the interior. Thus, removal of this surface layer would result in a very small surface concentration alumina, as observed in mass loss specimens after high temperature treatment and substantial surface recession. Treatment with N produced a rather adherent film, and the preferential evaporation of silicon can account for the higher value for Al(2p)/Si(2p) ratio. At lower temperature the evaporation of silicon and the surface recession are small, and hence the Al(2p)/Si(2p) ratio is the same as the fresh coating. If contamination of aluminum is ruled out in arc jet experiments, the resulting increase in Al(2p)/Si(2p) should be due to preferential loss of Si.

It follows from the above discussion that the presence of alumina on the surface may be an indication of an adherent product film and a small surface recession. An exception to this implication was found in one sample at a low temperature of 1410K where an adherent film, and a Al(2p)/Si(2p) ratio of 0.1 were expected. A rather low Al(2p)/Si(2p) value of 0.02 was found in this case. This could be due to engulfing of alumina by SiO_2 (Sp·gr SiC = 3.22; Sp·gr of SiO_2 = 2.2-2.6), or the loss of the surface layer during handling but cannot be resolved without further investigation.

γ-Measurement Samples: XPS analyses were made on samples after reaction with O, N and O + N in the γ-reactor. The results are summarized in Table 4.1-8. The reaction with O produced a surface chemistry similar to that observed in mass loss specimens. The surface consisted of SiO_2 with some free carbon and the fresh Al(2p)/Si(2p) ratio. Exposure to N also resulted in a surface consisting of SiC , Si_3N_4 or Si_2ON_2 with a rather high amount of alumina (Al(2p)/Si(2p) = 0.52). This is again consistent with mass loss specimens. N + O treatment gave similar results.

Sample spectra of XPS results on a specimen after reaction with N + O at 1673°K in γ-reactor is shown in Fig. 4.1-3a. Spectra of a specimen after reaction with O at 1722°K in mass loss reactor is shown in Fig. 4.1-3b. The figures indicate that the N(1s) and Al(2p) peaks are considerably higher after exposure to N + O mixture. The Si(2p) peak in 4.1-3b consists of two peaks ($\Delta E = 2.4$ eV) corresponding to SiC and SiO_2. The location of the single Si(2p) peak in Fig. 4.1-3a suggest that it is either SiC, Si_3N_4 or Si_2ON_2 (see Section 4.1.2A) and definitely not SiO_2. The C(1s) line in both figures is split showing both free carbon and SiC. The high binding energy peak corresponds to free carbon and low energy one to SiC. Note that the intensities of C_{SiC} and Si_{SiC} are nearly the same. The O(1s) peaks are not split but their intensities are about ten times those of the silicon peaks

The figures also illustrate the fallibility of using absolute intensities as a measure of the amount of an element in the specimen when the experimental conditions are not controlled rigidly to preserve cleanliness.
The Fig. 4.1-3b was obtained with a new x-ray anode, and Fig. 4.1-3a was taken about fifteen days later. Note that the intensities major peaks have been reduced by about 50% in 4.1-3a. This general lowering of intensity is presumed to be due in this case to a lower x-ray flux.

Table 4.3-8

XPS Results γ-Measurement Specimen of RPP Coating

Reactant	Temp	P_{O_2} (torr)	P_{N_2} (torr)	$\frac{(SiC+Si_3N_4+Si_2ON_2)}{Si_{2p}\ tot}$	$\left(\frac{SiO_2}{Si_{2p}\ tot}\right)$	$\frac{Al_{2p}}{Si_{2p}\ tot}$	$\frac{N_{1s}}{Si2p_{tot}}$	Free $\frac{C_{1s}}{Si2p_{tot}}$	$\frac{O_{1s}}{Si_{2p}}$ tot	Remarks, impurities
O	1740	0.52*	0	0	1	0.16	0	0.43	12.9	Ca
N	1719	0	1.6	1	0	0.52	0.96	0.23	5.6	
O + N	1673	$P_O=1.3\times10^{-2}$	1.5	1	0	0.43	0.43	0.37	5.1	

* 14% molecules are approximately dissociated

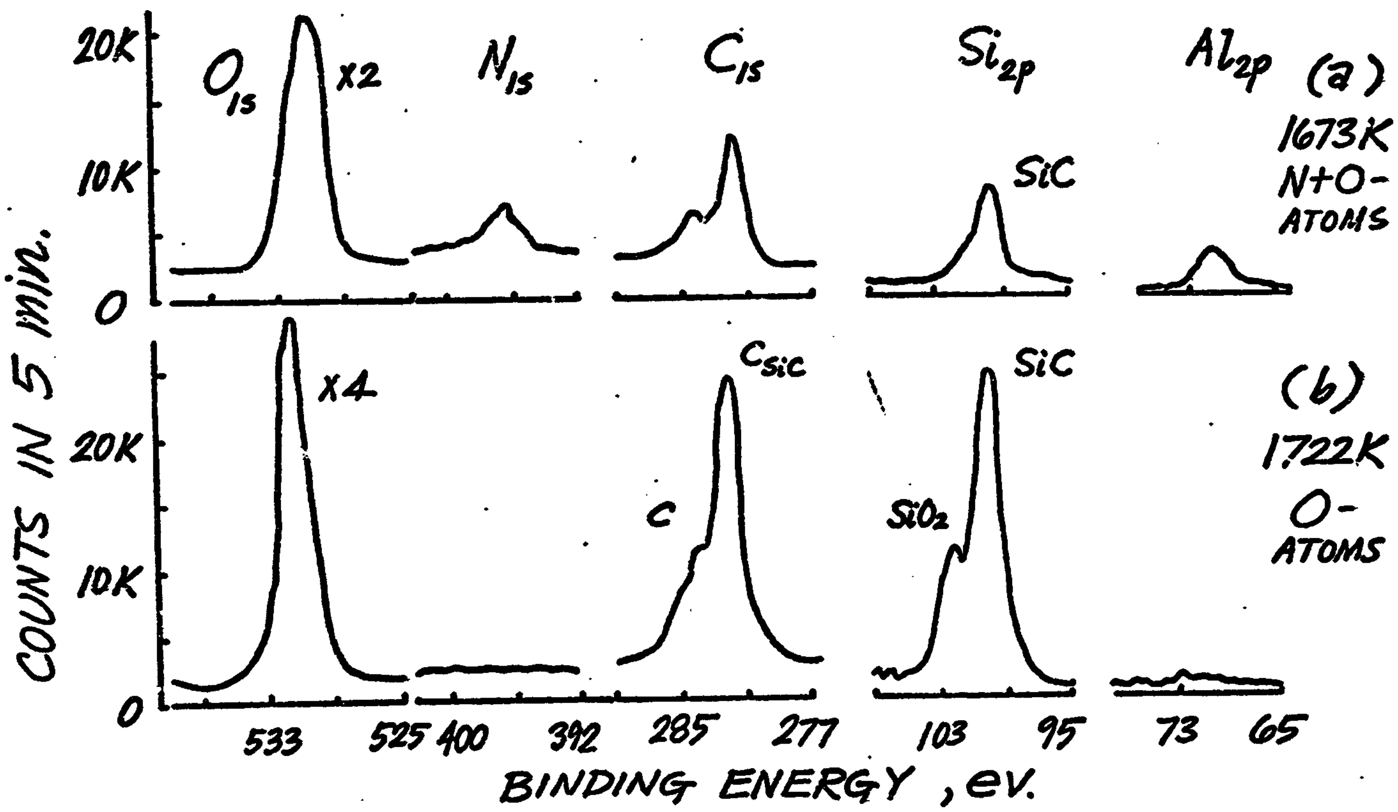

4.1-3 XPS spectra of RPP coating of (a) γ-sample after exposure to N + O atoms at 1673K and (b) mass loss sample after exposure to O atoms at 1722K.

D. Nickel: Nickel samples were analyzed by XPS before and after γ measurements. The spectra showed that the surfaces of initial nickel samples were NiO or NiO with a minor amount of Ni metal. After recombination studies up to 1070°K, the surface consisted of only NiO. The implication of this result is that, as expected, γ measurements were done mainly on an NiO surface, and the cleaning process did not remove the oxide film. Kim and Davis (1972) report that an evaporated nickel film oxidized to Ni_2O_3 in air in fifteen minutes. Hence if γ values on pure nickel are required, then the nickel metal should be formed in situ either by reduction with hydrogen at high temperature, or by evaporating nickel in vacuum.

4.1.3 Conclusions and Implications of XPS Experiments

The conclusions drawn from the data presented in Section 4.1.2 are summarized briefly below

1) Nitrogen is incorporated into the RPP surface after exposure to N atoms at temperatures from 1600-1900°K. The amount of nitrogen on the surface decreases as the temperature is increased from 1900°K to 2000°K. No nitrogen is taken up in N_2 at 2000°K. Thus XPS may provide a qualitative test for the presence of N atoms in a reactant gas stream.

2) In the temperature region 1400°K < T < 1600°K Si on the RPP surface is present as SiO_2.

3) At temperatures about 1700°K an integral SiO_2 protective coating is not maintained on RPP under the conditions of the mass loss experiments. Heating RPP about 1800°K in Ar yields a great excess of carbon on the surface. A carbon excess is also seen after heating to 1900°K in O_2, as a result of the lower reaction probability for O_2 vs. O in oxidation of carbon.

4) Loss of Al on the surface after mass loss experiments on RPP at T > 1700°K indicates substantial surface recession and non-adherent surface film. High Al content of arc jet tested RPP samples may indicate formation of a more adherent protective film at the high oxygen pressures of the arc jet experiment.

5) All γ measurements in RPP materials have been done on surfaces containing aluminum.

6) Half of the arc jet tested RSI samples received were contaminated with Al. Such contamination of arc jet tested RPP samples cannot be ruled out but enhancement of Al surface concentration by Si evaporation is possible.

7) The surface of the nickel used for γ calibration runs was NiO.

The presence of aluminum on RPP surfaces suggests that the effect of this component on γ should be studied independently. Stability of the surface film on RPP at the pressure used in the mass loss experiments appears poor and is aided only slightly by the presence of N atoms. The effect of reactant pressure as well as surface temperature appears to be important. Future tests of RPP stability and establishment of criteria for vehicle re-use can be aided by XPS.

4.2 Scanning Electron Microscopy

4.2.1 Technique

The physical morphology of the surface has a significant influence on the reaction kinetics, primarily through the extent of the surface available to the reactants (interface area) and through the ease of access of the reactant to the surface (pore size distribution). Moreover, in non-planar surfaces involved in a gas-solid reaction, there may be multiple collisions of the reactant (gas) with the surface, thereby increasing the "apparent" reaction probability [Rosner, (1972)]. It is also possible that the physical nature of the surface may change in the course of the reaction, thereby affecting the reaction probability. Thus, in the study of gas-solid reactions the physical structure of the solid surface should be defined.

At present, a complete characterization of physical structure or the "roughness" of the surface, especially of inhomogeneous surfaces, can not be made. However, scanning electron microscopy provides a tool by which one can obtain morphological details by means of high resolution pictures with good depth of focus and minimum sample preparation [Drew (1968), Murr (1970)]

In scanning electron microscopy a high energy electron beam (10-20KeV) is swept across the surface of the sample. Low energy secondary electrons emerge from the solid as a result of atomic excitations. The energy of these electrons as a general rule is less than 50 eV, and characterized by a maxima around 10-20 eV. The secondary electron yield depends upon the incident beam energy, surface chemistry, density of surface sites and more importantly on the surface morphology because of the angle the incident beam makes with any particular site. Secondary electrons emerging from the surface are collected, amplified, synchronized, and presented on a video display. During the scanning, the changes in surface morphology result in changes in secondary electron current and this provides an intensity contrast in the CRT display. The resulting image thus obtained appears three dimensional because of the secondary electron current contrast and by virtue of large depth of field associated with the small size of the incident beam and small aperture angles employed in the electron optics.

The ease of preparation of the sample (only a thin coating (500Å) of gold is necessary to prevent charging), and large depth of focus obtainable makes the scanning electron microscopy suitable for the observation of surfaces of TPS materials. Even though complete characterization of the roughness of the surface cannot be made by scanning electron microscopy, broad changes in the surface morphology can be correlated with the reaction probability.

4.2.2 Results of Scanning Electron Microscopy Experiments

The surfaces of TPS materials were observed by SEM in the as received state and after exposure at high temperature to $\underline{O}$, O_2, $\underline{N}$, N_2 and $\underline{N} + \underline{O}$ in the atom recombination reactor or in the mass loss reactor. Plasma arc jet tested samples were also examined. Although many of the details in the micrographs can not be described fully due to inadequate terminology, a brief summary of the observations is described.

A. RSI Coating (Lockheed 0042)

Fresh and Ion Bombarded: The surface of the fresh material was very smooth with little detail. Argon ion bombardment (580 eV), however produced a low density of pinholes. The hole size ranged from 0.5 μm to about 10 μm. The surface was depressed around the holes.

Exposure to Oxygen Environment (γ-measurement samples): Heating the RSI to 1100K in an oxygen atom atmosphere produced a smooth but wavy surface with craters of various sizes (up to 50 μm), as shown in Fig. 4.2-1. Higher temperature treatment produced a somewhat more pronounced wavy surface but with a lower density of craters. The craters appear to be due to escape of gases from the bulk in the form of bubbles.

Arc Jet Tested Samples: Samples arc jet tested at 1300K produced a surface similar to the one described above. A bubble that was frozen is shown in Fig. 4.2-2. The bubble density decreased after exposure to 10 cycles. Higher temperature testing (1600K) produced very rough cauliflower-like surface.

REPRODUCIBILITY OF THE ORIGINAL PAGE IS POOR

4.2-1

4.2-2

4.2-3

4.2-4

4.2-5

4.2-6

4.2-7

4.2-8

B. RPP Coating

Fresh: The RPP coating was made by siliconizing a woven graphite substrate. Carbon fibers (about 1 um) were bundled in about 1mm bundles and woven in a criss-cross manner. While the woven structure was clearly visible in the micrographs, the surface of the fresh coating was relatively smooth. Cracks of the order of 0.01 mm wide were also observed. The surface of the coating was broken in places where the bundles cross each other. Fig. 4.2-3 shows the surface of fresh RPP coating.

Higher Temperature Exposure to Oxygen, Nitrogen Atoms and Molecules: Scanning electron micrographs were obtained after exposure to $\underline{O}$, O_2, $\underline{O}$ + $\underline{N}$ at 1618, 1826 and 2013K. A sample exposed to $\underline{N}$ at 1826K was also examined.

Reaction with $\underline{O}$, O_2 at 1618K produced a loosely adherent film on the surface. This film had a tendency to fall off when subjected to mechanical shocks. The surface of the film was relatively smooth and flaky in structure. The substrate underneath the coating appeared to be similar to the fresh material. An adherent film and the substrate are shown in Fig. 4.2-4.

Exposure to $\underline{O}$ or O_2 above 1720K appeared to have melted the protective film. After cooling shiny glass like particles were seen. In the lower limit of this temperature region (1720-1930°K),they formed bridges and hence they were relatively continuous. In the upper limit only small isolated islands were observed. The film thus formed was extremely fragile and usually fell off during handling. For this reason, scanning electron micrographs of glass-like particles are not available. However, photo micrographs taken soon after reaction provided the necessary observation.

At 1720K, probably due to low viscosity, the molten layer appeared to be susceptible to aerodynamic shear. Fig. 4.2-5 illustrates this, where molten layers were frozen in the sides of samples.

Scanning electron micrographs of the substrates after exposure to $\underline{O}$, O_2 at 1820K showed a very smooth surface. Wide cracks along and across the specimen were also observed. At high magnification, as shown in Fig. 4.2-6,one can observe small spherical particles. Many of them lumped together. Exposure to $\underline{N}$ atoms at 1826K produced a dense looking surface. Surface cracks were fewer in number. Fig. 4.2-8 illustrates this for comparison purposes.

Exposure to mixture of N and O atoms appeared to produce a more adherent film. Examination of a sample after exposure to N + O of 1826K produced an appearance similar to that of a sample exposed to O, O_2 at 1618K.

Higher temperature exposure at 2013K to oxygen produced a surface clear of any product film. The surfaces looked etched and cracked in numerous places. Deep pits of various shapes were also observed. At very high magnification the surface was full of holes of the order of 0.3 μm as shown in Fig. 4.2-7. N + O mixtures at this temperature appeared to leave a thin, adherent spongy film on the surface.

These observations indicate that the behavior of the protective film can be classified into three different regions from its physical morphology. The low temperature region (below 1720K) produces an adherent film (even though susceptible to mechanical shocks especially towards the higher temperature limit) and the surface appearance is similar to that of fresh coating. At moderate temperatures (1720-1920K) the film melts and is susceptible to aerodynamic shear at the testing temperature. On cooling, the film is extremely susceptible to handling. At high temperatures (above 1920°K) generally no product film is observed and the substrate is full of microholes. Exposure to nitrogen atoms produces a denser and well adherent product below 1920K. Behavior of the surface layer in mixtures of O and N is between that of pure O or N. A fairly adherent film is observed at moderate temperatures, and the high temperature erosion is not as severe as in O.

Arc Jet Tested RPP: Surfaces of RPP coating after exposure to a plasma arc jet around 1900K were observed by SEM. Results were somewhat different with different samples even though the test conditions were similar. The surface of specimen (M 130-25 M131) was highly rough and showed a many-layered open structure. In places where these layers had been abraded, the surface was granular in structure. This sample showed high Al surface content in XPS measurements. The surfaces of two other specimens (W18LE60-1, W18-11-1) were smooth but wavy. The materials appeared to be abraded along the direction of the fibers. Some wide cracks were also observed in these samples and this may be due to handling in our laboratory (it was necessary to break the specimen in small pieces for XPS analysis). It should be noted that cracks were also observed after mass loss experiments where mechanical shocks were absent.

4.2.3 Conclusions and Implications

The presence of bubbles on the RSI (Lockheed 0042) coating after heating to 1300K suggests a significant uptake of gases or a gas generating mechanism in the bulk. Further investigation of this phenomenon is needed. Higher temperatures (1600K) produce very rough surfaces.

The protective oxide film formed on RPP coating after reaction with O at 1600K in the mass loss reactor is not adherent and provides little protection from further oxidation. The oxide film melts at higher temperature (1820K) and may be subject to aerodynamic shear. At very high temperature (2000K) the surface of RPP after oxidation or nitridation is very rough.

Based on the results of Section 4, both XPS and SEM techniques may be useful for testing surface conditions after a flight in order to decide on the replacement of TPS coatings.

5. AERODYNAMIC HEATING OF HYPERSONIC GLIDE VEHICLES

5.1 Method of Predicting Radiation Equilibrium Surface Temperatures for Candidate Thermal Protection System Materials

We have developed a simple procedure for predicting surface temperatures during re-entry at representative points on the Space shuttle orbiter (eg. nose stagnation-point, wing leading edge and lower fuselage) for the candidate TPS materials, including those studied in this program. This procedure, outlined below, should also prove useful in the future as new coatings and γ measurements become available, since it rapidly provides a quantitative measure of the benefits to be achieved in flight via reduced local atom recombination rates. Using this method for a material with any $\gamma_O(T_w)$, $\gamma_N(T_w)$, $\varepsilon(T_w)$ - relation* and for an orbiter with any prescribed re-entry trajectory (on the altitude-flight velocity plane) the instantaneous surface temperature at which the outgoing thermal radiation is in balance with the prevailing aerodynamic heat flux can be predicted at critical points on the Orbiter vehicle. Basically, for surface elements with an insignificant "view" of other Orbiter surface elements the quasi-steady radiation equilibrium temperature is obtained by a numerical solution of the nonlinear equation:

$$\varepsilon(T_w) \cdot \sigma T_w^{\,4} = -\dot{q}_w''(T_w) \qquad (5.1\text{-}1)$$

where $\dot{q}_w''(T_w)$ is the prevailing aerodynamic heat flux to the surface element under investigation, and σ is the Stefan-Boltzmann constant. The approach we have adopted to calculate $-\dot{q}_w''(T_w)$ includes the distinct participating physiochemical phenomena in a rational way, and yet leads to rapidly evaluated formulae essential for engineering design purposes. As will be seen, where necessary, the method is "calibrated" via numerical solutions to the nonequilibrium shock layer-boundary layer problem reported in the literature.

---

* Here $\varepsilon(T_w)$ is the total hemispheric emittance of the material under the conditions prevailing during re-entry

Our basic assumptions and the dominant effects taken into account are the following

a. Stagnation point (or line) heat transfer is comprised of a thermal (Fourier conduction) and chemical (recombination) contribution, the latter being estimable for conditions of Orbiter re-entry by neglecting three-body gas phase atom recombination [cf. eg. Rosner (1963)].

b. The atom recombination contributions due to O and N are treated independently since, in general, $\gamma_O \neq \gamma_N$ and differing amounts of O and N atoms will be generated in the shock layer, depending on geometry and flight conditions[+] [cf. eg. Kang (1970, 1972), Blottner (1969), Li (1973)].

c. While high Reynolds number boundary layer (BL) theory provides a useful first approximation to $-\dot{q}''_w$, the density ratio-shock Reynolds number product $[(\rho_\infty/\rho_s) \cdot Re_s]$ is small enough under conditions of peak orbiter heat flux to necessitate the introduction of a correction factor $F_{Re} \equiv -\dot{q}''_w/(-\dot{q}''_w)_{BL}$ expected to be not very different from unity (cf. eg. Cheng (1963), under Space Shuttle Orbiter conditions.

d. Owing to inadequate O_2 and N_2 residence time in the low density shock layer, the N and O-atom concentrations attained at the effective outer edge of the wall boundary layer (see Fig. 5.1-1) in general, fall below that corresponding to local thermodynamic equilibrium (LTE) at post-shock adiabatic stagnation conditions (cf. eg. Chung (1961), Tong (1965), Park (1964), Inger (1966), Kang (1970, 1972)]. This influences the partitioning of $-\dot{q}''_w$ between conduction and atom recombination by increasing the former at the expense of the latter.

e. At the prevailing reactant pressures and temperatures N and/or O-atom loss by chemical combination with the surface (eg. to produce (SiO(g), CO(g), Si_3N_4(c) etc) is negligible compared with surface-catalyzed atom recombination

---

[+] Also, should it be necessary in the future to account for surface-catalyzed NO(g) production, or homogeneous bimolecular reactions (see Section 5.3.2) information on both ω_N and ω_O will be required.

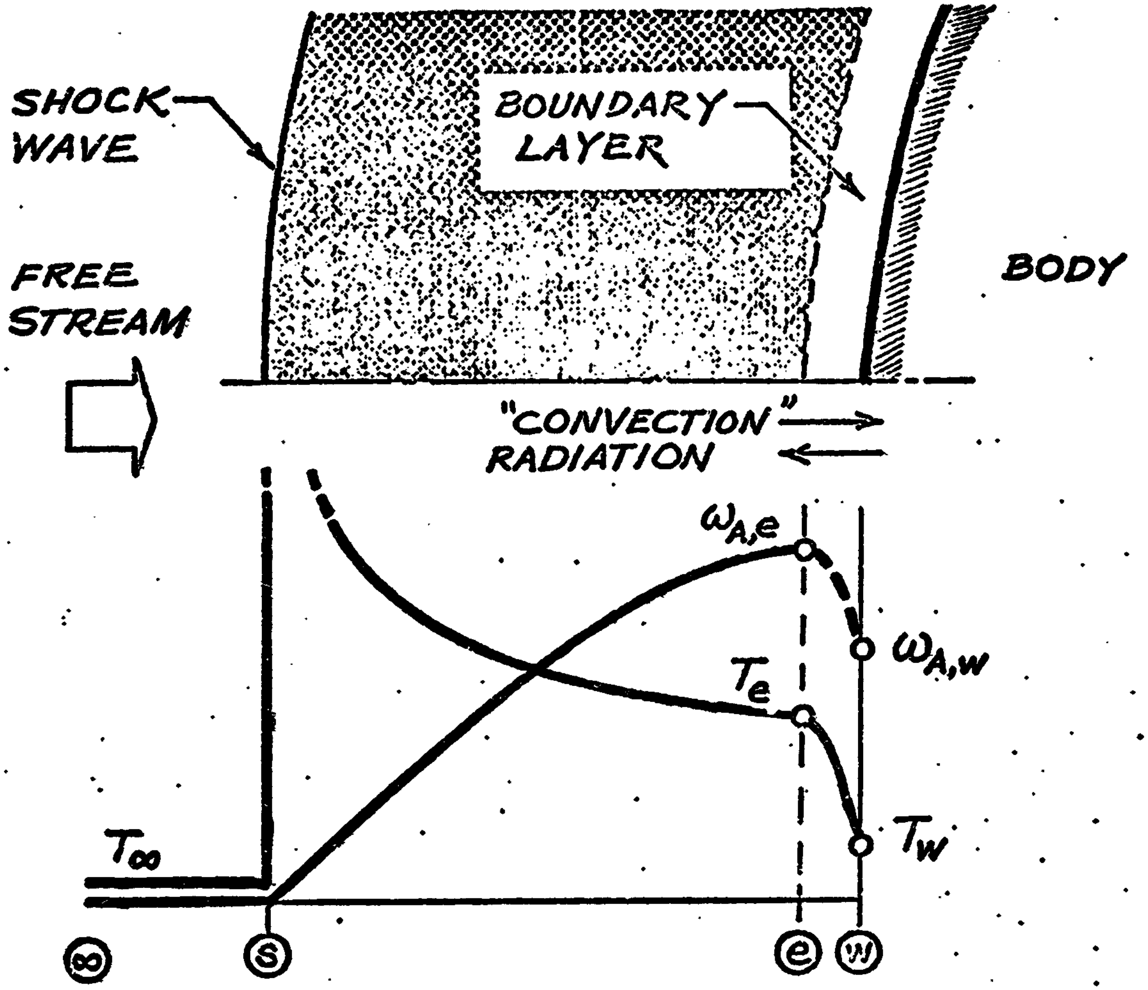

5.1-1

Atom concentration and gas temperature profiles in the stagnation region shock layer of a hypersonic, blunt-nosed body.

To evaluate $(-\dot{q}''_w)_{BL}$ we exploit the correlation recommended by Rosner (1963), which, for our present purposes, can be recast in the following form:

$$(-\dot{q}''_w)_{BL} = (\rho_\infty U \ St_h)_{BL} \cdot \Delta h_f \ [1 + \sum_{i=0,N} \phi_i \mathcal{H}_i] \qquad (5.1\text{-}2)$$

Here the relevant heat transfer coefficient is:

$$(\rho_\infty U_\infty \ St_h)_{BL} = \begin{bmatrix} 0.763 \\ \text{or} \\ 0.570 \end{bmatrix} \cdot \left(\frac{\rho_w \mu_w}{\rho_e \mu_e} \right)^{0.1} \cdot \left(\beta \rho_e \mu_e \right)^{1/2} \cdot (Pr)^{-0.6} \qquad (5.1\text{-}3)$$

for a 3 or 2-dimensional stagnation point, β being the prevailing velocity gradient at the outer edge of the boundary layer. Since Δh_f is the "frozen" enthalpy difference across the boundary layer, the terms $\phi_i \mathcal{H}_i$ $(i=0,N)$ explicitly embody the atom diffusion-recombination contributions. Thus, in the absence of gas phase atom recombination, we write[‡] [Rosner (1963)]:

$$\phi_i = \frac{\mathcal{W}_i}{1 + \mathcal{W}_i} \qquad (i = 0,N) \qquad (5.1\text{-}4)$$

where

$$\mathcal{W}_i \equiv \frac{\frac{1}{4} \cdot \left(\frac{8RT_w}{\pi M_i} \right)^{1/2} \cdot \gamma_i(T_w) \cdot \rho_w}{F_{Ra} \cdot (\rho_\infty U \cdot St_h)_{BL} \cdot (Le_i)^{0.6}} \qquad (5.1\text{-}5)$$

and

$$\mathcal{H}_i \equiv (Le_i)^{0.6} \cdot \frac{\Delta h_{chem.\ i,\ max}}{\Delta h_f} \qquad (5.1\text{-}6)$$

It is convenient to introduce two functions of shock layer Damköhler number, $F_{Dam,i}$ defined by

$$F_{Dam,i} \equiv \omega_{i,e}/\omega_{i,e;eq} \qquad (i=0,N) \qquad (5.1\text{-}7)$$

[†] Our notation is largely that of Rosner (1963). R/M_i is the specific gas constant and Le_i is the Lewis number based on the pseudo-binary diffusion coefficient D_{i-mix}

[‡] Here we assume that T_w is not so large as to cause $\omega_{i,eq}(T_w;p)$ to be comparable to $\omega_{i,w}$ $(i = 0,N)$

This will allow us to take into account incomplete shock layer dissociation (item d above), expected to be especially important for estimating the N-atom contribution to $-\dot{q}''_w$. Values of $\mathcal{H}_{i,eq}$ are readily calculated from Eq. 5.1-6 with $F_{Dam,i} = 1$ and the values of $\omega_{i,eq}$ given in available tables - eg. Lewis and Burgess (1965). As discussed below, values of $F_{Dam,i}$ are computed in a separate subroutine from correlation formulae compatible with specific shock layer computations (cf. eg. Chung (1961) Park (1964), Tong (1965), Inger (1966), Chung, Holt and Liu (1968), Kang (1970), Blottner (1969) and Li (1973)]. The values of $F_{Dam,i}$ not only explicitly determine the $\mathcal{H}_i$, but they appear implicitly in the evaluation of Δh_f, which is shown below to exceed $(\Delta h_f)_{eq}$ (the value of Δh_f that would have prevailed had complete equilibrium been achieved at adiabatic post-normal shock stagnation conditions (see Fig. 5.1-1)).

Since complete post-shock equilibrium air conditions have been conveniently tabulated by Lewis and Burgess (1965) at specific altitude-velocity couples (Z,U) by reading in these data and using a simple two dimensional (Z,U) interpolation, we have developed a computer program which finds T_w using the above formulation for a vehicle passing through any point on the altitude (Z) flight velocity (U) plane. Thus, radiation equilibrium temperature calculations are now possible , for any orbiter vehicle trajectory. Of course the corresponding temperatures for very active or totally inactive atom recombination catalysts of any emittance can also be rapidly obtained, to determine the margin available for future materials improvements <u>via</u> reductions in $\gamma_i(T_w)$.

[+] We adopt the convention that T_w is the reference temperature in apportioning chemical and thermal contributions to the gas mixture enthalpy. Thus $h_{f,w} = 0$ and h_{chem} is based upon heats of formation evaluated at T_w [see, eg. Rosner (1972) and Bartlett and Grose (1969)].

While the procedure is illustrated here for the forward stagnation region of the fuselage (nose) and wing it can be modified via the use of an effective value of β to provide estimates at other critical locations on the orbiter vehicle (eg. at the base of the fuselage). Thus, at high angle of attack the fuselage will take on some of the aerodynamic characteristics of a swept "cylinder". This implies that a point on the underside of the fuselage along the line of bilateral symmetry of the aircraft but upstream of the wing might be considered to be on the two dimensional stagnation line of a "cylinder" with an effective nose radius obtainable from the fuselage cross-section and exposed to a normal velocity $U\ \sin\alpha$.

Further development and exploitation of these methods was beyond the scope of the present program, however, it is useful to consider the following details of the method to provide the basis for intelligent modifications and extensions in the future. Illustrative calculations and discussions of their implications are given in Section 5.2 for the RPP leading edge/nose cap material. Extensions of our methods to provide rational predictions for downstream RSI panels will be considered in the future.

+ For a 3-dimensional, symmetrical stagnation point (blunt nose) we use the modified Newtonian approximation for the inviscid velocity gradient, β, appearing in Eq.(5.1-2). [Boison and Curtiss (1959)], viz

$$\beta = \left\{ (\rho_\infty/\rho_s) \left[2 - (\rho_\infty/\rho_s) \right] \right\}^{1/2} U/R_B$$

For a 2-dimensional unswept stagnation line the corresponding value of β is [Hayes and Probstein (1959)]:

$$\beta = \left[3(\rho_\infty/\rho_s) \right]^{1/2} U/R_B$$

‡ No attempt is made to compute here the tradeoff between the beneficial effect of wing sweep-back (via reduction of normal component of velocity) and the viscous dissipation associated with the spanwise component of the flow. Since treating only the former would be overly optimistic, our two-dimensional stagnation line predictions (see Section 5.2) are for an equivalent unswept "cylinder".

5.1.1 Equilibrium Stagnation State Conditions

An important "reference" state of dissociated air for computing local aerodynamic heating is the equilibrium state obtained by adiabatically stagnating the hypersonic free-stream. A sufficiently complete description of this state would consist of the pressure p_e, the temperature $T_{e,eq}$ and composition (mole fractions) $x_{i,e;eq}$ ($i = O, N_2, NO, N, N_2, \ldots$), from which all thermodynamic and transport properties entering Eq. (5.1-1) could be computed. This state could, of course, be computed ab initio for each flight condition, (U,Z) using a subroutine incorporating the equations of state, energy, momentum and a Gibbs free-energy minimization procedure. However, since our goal is a design-oriented aerodynamic heating program which involves maximum simplicity and minimum computer time we instead make use of the availability of such equilibrium stagnation state calculations at "mesh points" in the range U = 6 (1) 26 kfps, Z = 130 (10) 400 Kft [see Lewis and Burgess (1965)]. These data are put into the program on cards and two-dimensional interpolation is done to provide the value of any property $\Phi(U,Z)$ in terms of the tabulated values of this same property at the "neighboring" mesh points. For this purpose we use the truncated (quadratic) series expansion:

$$\Phi(U,Z) = \Phi(U_o,Z_o) + (\Phi_U)_o(U-U_o) + (\Phi_Z)_o \cdot (Z-Z_o) \qquad (5.1\text{-}8)$$
$$+ \frac{1}{2}\left[(\Phi_{UU})_o\cdot(U-U_o)^2 + 2(\Phi_{ZU})_o\cdot(U-U_o)\cdot(Z-Z_o) + (\Phi_{ZZ})_o\cdot(Z-Z_o)^2\right]$$

where (U_o, Z_o) is the nearest mesh point on the altitude-flight speed plane and the partial derivatives evaluated at this point, eg. $(\Phi_Z)_o \equiv (\partial\Phi/\partial Z)_{Z=o}$ etc. are evaluated using central-difference formulae [see, eg. Hildebrand (1966)] If flight conditions are such that complete O_2 and N_2 dissociation occurs within the shock layer then these interpolated properties Φ are used as is to compute ρ_e, μ_e, Δh_f etc. required to evaluate $(-\dot{q}''_w)_{BL}$. However, should the shock layer dissociation kinetics of O_2 and /or N_2 be inadequate, the abovementioned "reference" properties Φ are still used to generate relevant gas mixture properties at the outer edge of the boundary layer in terms of the values of $F_{Dam,i} \equiv \omega_{i,e}/\omega_{i,e;eq}$ ($i = O, N$). This procedure is outlined in Section 5.1.3.

5.1.2 Thermodynamic and Transport Laws and Data

The present version of the computer program incorporates the following basic assumptions and conventions:

a) dissociated air can be considered a mixture of the 5 perfect gases O, O_2, NO, N and N_2

b) transport properties for each of these neutral species depend on local pressure and temperature in accord with the predictions of first-order Chapman-Enskog theory with the Lennard-Jones 12:6 interaction parameters given by Svehla (1962). The thermal conductivity of the diatomic molecules O_2, NO and N_2 are related to their corresponding "monatomic" conductivities $(15/4)\,R\mu_i/M_i$ by the Eucken factor [Bird, Stewart and Lightfoot (1960)]

c) The mixture properties μ and λ are well approximated by "mixing rules" of the Wassiljewa-Wilke form [Bird, Stewart and Lightfoot (1960)]. D_{i-mix} (for i = O, N) is computed from

$$D_{i-mix} = (1-x_i)\cdot\Big(\sum_{j\neq i} x_j/D_{ij}\Big)^{-1} \qquad (5.1\text{-}9)$$

d) absolute species enthalpies (based on T_{ref} = 298.16K) and dimensionless molar heat capacities $(C_{p,i}/R)$ are well-approximated by the polynomial expressions given by Li (1973). These agree with the JANAF data up to 6000K, and formally allow thermodynamic calculations up to 40,000K[‡]

e) frozen (sensible) and chemical contributions to the absolute species enthalpies are <u>defined</u> using $T_{ref} = T_w$. Thus, the absolute molar enthalpy for species i is written:

$$H_i(T)=\int_{T_w}^{T} C_{p,i}\,dT + \Delta H^{o}_{f,i}(T_w) \qquad (5.1\text{-}10)$$

[‡] Of course, the 5 species model of dissociated air breaks down above some (pressure-dependent) threshold temperature

where $\Delta H^{\circ}_{f,i}(T_w)$ is the enthalpy change across the reaction forming one mole of species i from O_2 and/or N_2 at temperature T_w and $C_{p,i}$ is the molar specific heat at constant pressure. With this convention $\Delta h_f \equiv h_{f,e} - h_{f,w} = h_{f,e}$ so that:

$$\Delta h_f = \sum_i \omega_{i,e} \int_{T_w}^{T_e} c_{p,i} dT \qquad (5.1\text{-}11)$$

where $c_{p,i} \equiv C_{p,i}/M_i$. Also:

$$\Delta h_{chem,i} \equiv h_{chem,i,e} - h_{chem,i,w} = (\omega_{i,e} - \omega_{i,w}) \cdot Q_i \qquad (5.1\text{-}12)$$

where $Q_i \equiv \Delta H^{\circ}_{f,i}(T_w)/M_i$

f) where mean properties appropriate to the boundary layer are required (eg, Pr and Le_i in Eq.(5.1-2), the values used herein are the arithmetic mean between those at station e and station w.

While refinements to these property estimates can be readily incorporated in future modifications of the present program, these choices proved convenient and were deemed sufficient for the illustrative calculations included herein.

5.1.3 Incomplete O_2 and/or N_2 Dissociation in the Low Density Shock Layer

Under glide re-entry conditions it seems likely that shock layer dissociation of O_2 and N_2, being finite rate processes, will not proceed to their equilibrium values in the residence times available[†] [Chung (1961), Cheng (1963), Tong (1965) Inger (1966), Kang (1970), Kang and Dunn (1972)]. For this reason, our formulation incorporates the two functions $F_{Dam,i}$ ($i = O,N$) which can vary between zero (no dissociation) and unity (equilibrium dissociation) depending upon the

---

[†] In this important respect the flight situation is markedly different than most arc jet-produced environments (where appreciable atom concentrations usually exist in the "free stream" as a result of recombination "freezing" during the nozzle expansion). See, also, Section 5.4.

magnitude of an appropriate Damköhler number for the dissociation of molecules M ($M = O_2, N_2$) of the form:[†]

$$\frac{t_{flow}}{t_{dissoc.}} = \frac{\Delta}{U} : \frac{\rho_s}{\rho_\infty} \cdot \frac{k_M(T_s)}{(M_M/N)} \rho_s \qquad (5.1\text{-}13)$$

where Δ is the shock layer thickness, $k_M(T_s)$ is the dissociation rate constant at temperature T_s and N is Avogadro's number (6.023 x 10^{23} molecules/mole).

Since the $F_{Dam,i}$ are incorporated <u>via</u> a subroutine, any one of a number of previous estimates and correlations for the $F_{Dam,i}$ can be readily used in the present program. In this connection we have investigated the $F_{Dam,i}$ correlations suggested by the results of Park (1964), Tong (1965) and Inger (1966). These authors treated a pseudo-binary (atom "A" + molecule "M") model of partially dissociated air and predicted non-equilibrium values of ω_A established at a noncatalytic wall over a range of equivalent nose radii, ambient densities, flight velocities and wall temperatures, providing analytical or graphical correlations of their results for particular choices of the dissociation rate constant. In exploiting this work we make the useful assumptions:

A1 Owing to the disparity in bond energies, O_2 dissociation is sufficiently faster than N_2-dissociation so that either one of two cases prevails:

$F_{Dam,O} < 1$ when $F_{Dam,N} = 0$ <u>or</u> $F_{Dam,O} = 1$ when $F_{Dam,N} < 1$

A2 Values of ω_i at the effective outer edge of the wall boundary layer (station e) can be identified with predicted values of $\omega_{i,w}$ for a noncatalytic (γ=0) wall.

A3 Bimolecular dissociation kinetics dominate the shock layer, hence at any flight speed $\omega_{i,e}$ depends on ρ_∞ and R only through their product: $\rho_\infty R$ ("binary scaling").

[†] While this experssion may ultimately prove useful to correlate available $F_{Dam,i}$ "data" (multicomponent shock layer computer runs) it is not explicitly invoked in the present computational scheme. However, it should be remarked that the $F_{Dam,i}$ correlation cited below exhibits the $\rho_\infty R_B$ dependence implicit in Eq. 5.1-13 at constant flight speed U.

The first of these essentially states that O_2 and N_2 dissociation are "sequential", the second is expected to be reasonable under conditions such that F_{Re} is not very different from unity (i.e. $(\rho_\infty/\rho_s) \cdot Re_s$ sufficiently large so that departures from high Reynolds number boundary layer theory are not very great). The third assumption is defensible for Space Shuttle Orbiter re-entry conditions, except when $F_{Dam,i}$ approaches unity, (since the equilibria $2A \rightleftarrows M$ are established via 3-body homogeneous recombination).

Since the simplest of the suggested $F_{Dam,i}$ correlations is that due to Tong (1965) we will illustrate the nature of an $F_{Dam,i}$ subroutine for this case. However, in view of the fact that agreement on the magnitude of the $F_{Dam,i}$ implied by different workers is not good (see below), we suggest that improved $F_{Dam,i}$ subroutines be developed for future use. Our program is organized to facilitate the incorporation of such future developments as well as the calculation of interesting limiting cases ($F_{Dam,i} = 0$ or $F_{Dam,i} = 1$).

For the parameter range $278 \leq T_w \leq 1665\text{K}$, $15 \leq U \leq 26$ kfps, Tong's numerical integrations across the shock layer could be represented by

$$\log_{10} \frac{(\omega_{A,w})_{\gamma=0}}{\omega_{A,\max}} = -\left[\frac{\log_{10}(\rho_\infty/\rho_{\infty,\max}) + 0.045}{1.478}\right]^2 \qquad (5.1\text{-}14\ )$$

where $\rho_\infty/\rho_{\infty,\max} \leq 0.989^\dagger$ and

$$\omega_{A,\max} \equiv \left[0.608\left(\frac{U}{10^4}\right)^2 - 1.03\right] \cdot \left(\frac{10^3}{T_w}\right)^{1.65} \qquad (5.1\text{-}15\ )$$

$$\rho_{\infty,\max}(\text{lb}_m/\text{ft}^3) \equiv R_B^{-1}\left[1.22 \times 10^{-5} + 3.76 \times 10^{-3}\left(\frac{U}{10^4}\right)^{-7}\right] \qquad (5.1\text{-}16\ )$$

and R_B, U are expressed in feet and feet/sec, respectively. In using these results (in accord with A1,2) we conclude that if $(\omega_{A,w})_{\gamma=0} \leq 0.232$

---

† For $\rho_\infty/\rho_{\infty,\max} > 0.989$ we take $(\omega_{A,w})_{\gamma=0}/\omega_{A,\max} = 1.0$ (see below)

then $F_{Dam,N} = 0$ and

$$F_{Dam,O} = (\omega_{A,w})_{\gamma=0} \; / \; \omega_{O,e;eq} \qquad (5.1\text{-}17)$$

However, if $(\omega_{A,w})_{\gamma=0} \geq 0.232$ then $F_{Dam,O} = 1$ and

$$F_{Dam,N} = \omega_{N,e} / \omega_{N,e;eq} \qquad (5.1\text{-}18)$$

where

$$\omega_{N,e} = [\,(\omega_{A,w})_{\gamma=0,\mathrm{Tong}} - 0.232]\cdot\frac{Q_O}{Q_N} + (\omega_{A,w})_{\gamma=0,\mathrm{Tong}}\cdot\left(1 - \frac{Q_O}{Q_N}\right) \qquad (5.1\text{-}19)$$

To indicate the variations in $F_{Dam,i}$ expected based on "atom + molecule" computations available in the literature, we compared values of $F_{Dam,i}$ found from Tong's correlation, with those implied by Fig. 6 of Inger (1966) for the specific conditions $R_B = 1$ ft, $T_w = 1500$K, $U = 26$ kfps. This comparison is shown in Fig. 5.1-2, where it is noted that Inger's method predicts complete O_2 dissociation to higher altitudes than Tong's and a more gradual transition from equilibrium to frozen behavior for nitrogen at lower altitudes. For $R_B = 1$ ft, near conditions of peak heating, both methods predict nonequilibrium N_2 dissociation and essentially complete O_2 dissociation.

We also found that the empirical correlations suggested by Park (1964) to describe his numerical results for $(\omega_{A,w})_{\gamma=0}$ led to physically unreasonable results for the $F_{Dam,i}$ under Re_s conditions relevant to the Space Shuttle Orbiter.

Of course, numerical predictions of $(\omega_{i,w})_{\gamma=0}$ are now available for specific conditions (U, Z, R_B, T_w) based on lengthy multicomponent, viscous shock layer integrations, and presumably more accurate reaction rate constants [Kang (1970), Kang and Dunn (1972), Li (1973), Blottner (1969)].

+ Had Tong's correlation for $\rho_\infty/\rho_{\infty,max} > 0.989$ been used, the corresponding values of $F_{Dam,i}$ would turn down at sufficiently <u>low</u> altitudes. This non-physical behavior was therefore precluded by setting $(\omega_{A,w})_{\gamma=0}/\,\omega_{A,max} = 1.0$ above $\rho_\infty/\rho_{\infty,max} = 0.989$.

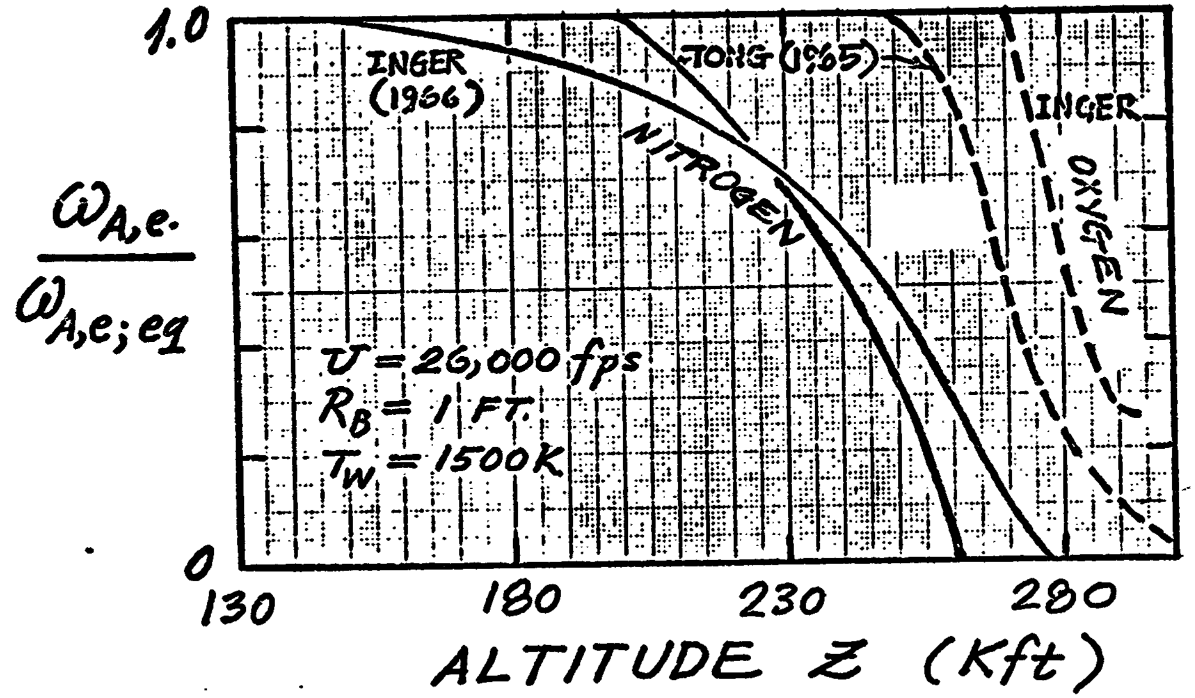

5.1-2 Approach to dissociation equilibrium in the shock layer of a hypersonic vehicle; flight velocity = 26 kfps; nose radius = 1 ft.; wall temperature = 1500K; comparison of prediction methods of Inger (1966) and Tong (1965).

In the future these "data points" should be used to obtain improved correlations for the $F_{Dam,i}$ functions introduced here - or to "calibrate" the $F_{Dam,i}$ routine illustrated above.

It remains to consider how the $\omega_{i,e}$ and T_e are calculated in terms of the $F_{Dam,i}$. The composition $\omega_{i,e}$ follows immediately from the definition of $F_{Dam,i}$ $(i=0,N)$, the known values of $\omega_{i,e;eq}$, and the facts that a) $\Sigma\omega_{i,e} = 1$ b) $\omega_{(N),e}/\omega_{(0),e} = (1-0.232)/(0.232)$ [where $\omega_{(N)}$ and $\omega_{(0)}$ are, respectively, the *element* mass fractions of nitrogen and oxygen]. When $\omega_{NO,e;eq}$ is not completely negligible we add the tentative approximation c) $\omega_{NO,e} \approx F_{Dam,0} \cdot \omega_{NO,e;eq}$. These statements then yield two equations in the two unknowns $\omega_{O_{2,e}}$ and $\omega_{N_{2,e}}$ which completes the determination of the $\omega_{i,e}$. The corresponding temperature T_e then follows from the constancy of the total enthalpy, *ie.* T_e satisfies the nonlinear equation:

$$\sum_i \omega_{i,e} \cdot h_i(T_e) - \sum_i \omega_{i,e;eq} \cdot h_i(T_{e,eq}) = 0 \qquad (5.1\text{-}20)$$

This is solved *via* a rapidly convergent Newton-Raphson iteration procedure, starting with the rough estimate:

$$T_e^{(0)} = T_{e,eq} + \sum_{i=0,N} (1-F_{Dam,i}) \cdot \omega_{i,e;eq} Q_i / c_{p,e;eq} \qquad (5.1\text{-}21)$$

Having thus determined $\omega_{i,e}$, and T_e compatible with the flight condition (U,Z) and the corresponding $F_{Dam,i}$, all gas properties at station e can be computed as outlined in Section 5.1.2 (with the additional approximation $p_e \approx p_{e,eq}$). Thus, ρ_e, μ_e, Δh_f etc appearing in the expression for $(-\dot{q}_w'')_{BL}$ are evaluated.

5.1.4 Numerical Methods and Computational Efficiency

It is clear from the above subsections that the desired radiation equilibrium temperature T_w appears in many explicit and implicit ways in Eq. (5.1-1). However, this causes no difficulty if an iterative, numerical solution is used, in which all functions of T_w are evaluated using the "current" estimate $T_w^{(n)}$ and a systematic convergent procedure for calculating $T_w^{(n+1)}$ is provided. The scheme adopted here is a finite-difference modification of the Newton-Raphson method, which circumvents the need to calculate an analytic derivative of the function whose "root" is being sought. Thus if Eq. (5.1-1) is represented by

$$f(T_w) = 0 \qquad (5.1\text{-}22)$$

and if $T_w^{(n)}$ is the current estimate of the root, an improved estimate is:

$$T_w^{(n+1)} = T_w^{(n)} - \frac{\frac{1}{2}\left[f(T_w^{(n)} + \hbar) + f(T_w^{(n)} - \hbar)\right]}{\dfrac{\left[f(T_w^{(n)} + \hbar) - f(T_w^{(n)} - \hbar)\right]}{2\hbar}} \qquad (5.1\text{-}23)$$

where the temperature increment ħ is (arbitrarily) taken to be 10 K. The first approximation in this scheme, ie. $T_w^{(0)}$ is taken to be the radiation equilibrium temperature obtained from the preceding point (U,Z) along the re-entry trajectory. In practice, this scheme has proven to be quite effective, usually requiring no more than 4 iterations to obtain $\left|T_w^{(n+1)} - T_w^{(n)}\right| \leq 1\ K$. Thus, the value of T_w at each (U,Z) point along a re-entry trajectory can be obtained with about 2 sec of computer time on an IBM 360/67. This computational efficiency will make it possible to exploit the program for parametric and design studies at minimal cost.

5.2 Implications of γ-Results

To illustrate the use of the computational procedures outlined in Section 5.1 in predicting important trends and parametric dependencies we have computed radiation equilibrium temperatures for the RPP (leading edge, nose cap) material under a number of aerodynamic conditions. In addition to calculations based on our experimentally obtained γ_i-values we have also included calculations based on the extreme (limiting) cases $\gamma_i = 0$, $\gamma_i = 1$. All calculations below are based on a total hemispheric emittance function $\varepsilon(T_w)$, ranging between 0.94 and 0.85, in accord with the normal hemispheric emittance data reported in Fig. 5-26 of LTV (1972). In addition to calculations in which shock layer dissociation nonequilibrium effects are incorporated <u>via</u> the $F_{Dam,i}$-subroutine illustrated in Section 5.1.3, comparisons are included for the limiting cases $F_{Dam,i} = 1$ ($i = 0,N$) [equilibrium dissociation in the shock layer] and $F_{Dam,i} = 0$ [no dissociation (or ionization) in the shock layer].

Figure 5.2-1 illustrates the role γ can play in determining the wall temperatures expected under peak heating ($U = 24$ kfps, $Z = 240$kft) conditions for a nose radius of 1 ft. Here γ is considered to be a parameter ($10^{-3} \leq \gamma_A \geq 10^{\circ}$) and no distinction is made between γ_O and γ_N. Note that if equilibrium dissociation were achieved in the shock layer then $T_w(\gamma = 10^{-3})$ would be about 380K less than $T_w(\gamma = 10^{0})$, with maximum sensitivity of T_w to γ in the range $10^{-2} \leq \gamma \leq 10^{-1}$. Not surprisingly, when allowance is made for incomplete N_2 dissociation in the shock layer, this sensitivity of T_w to γ decreases, amounting to about 62K if only O_2 dissociated. The extent of dissociation† depends on the nose radius, and if the nose radius were only 1 ft. then using the Tong (1965) correlation to estimate $F_{Dam,i}$ yields a sensitivity of T_w to γ of only about 40K.

It is now interesting to consider the predicted T_w vs. time history during a typical Orbiter re-entry trajectory using experimental γ-data and considering several body radii in the range of interest. The cases

---

† Interestingly enough, these predictions suggest that perfect catalyst ($\gamma = 1$) with equilibrium shock layer dissociation would run some 130K cooler than a surface of the same emittance and nose radius in a non-dissociating (and/or ionizing) $O_2 + N_2$ atmosphere. This is attributed to the effect of very different gas properties at the values of T_e predicted without dissociation.

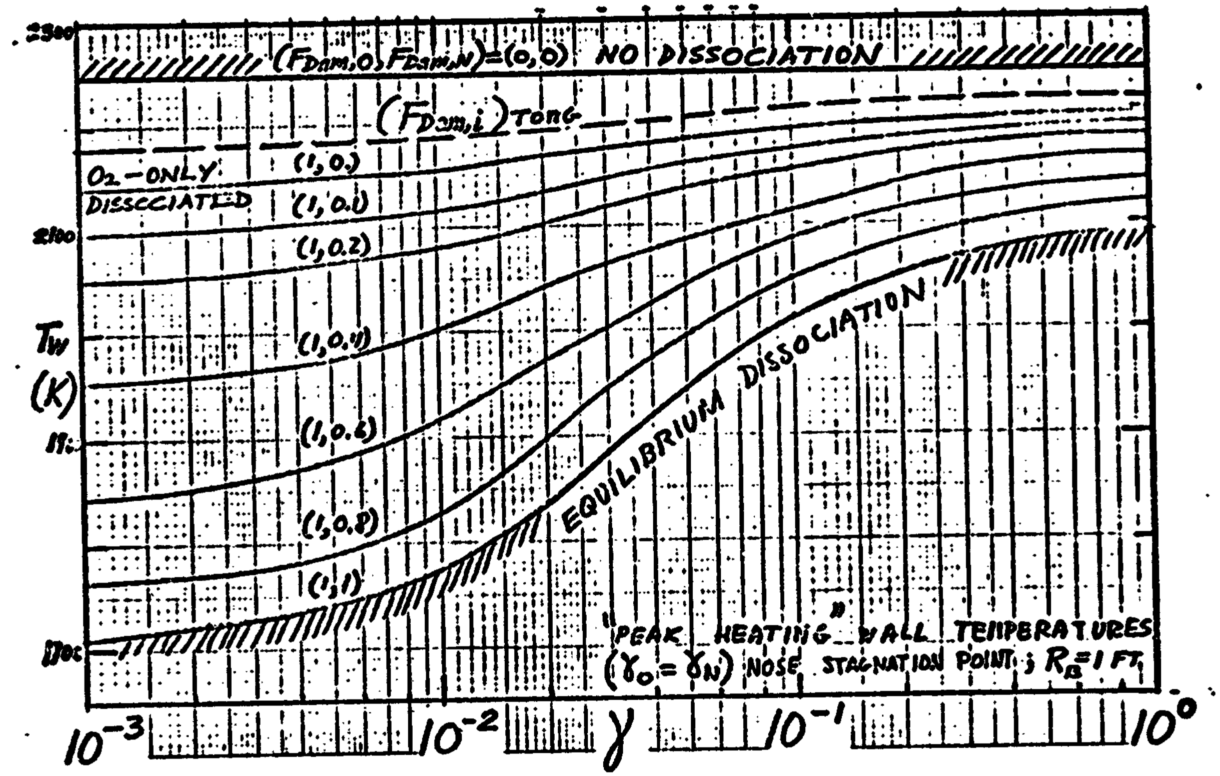

5.2-1 Dependence of radiation equilibrium temperature on atom recombination coefficient for a 1 ft. nose radius body (3-dim) under conditions of peak aerodynamic heating.

described below are only illustrative of what can now be economically accomplished using the computational methods of Section 5.1. In Figs. 5.2-2 to 5.2-4, γ_{EXP} refers to calculations in which the γ_i values were based on our duct reactor measurements in O + N mixtures. Predictions using the data shown in Fig. 2.3-3 (and their extrapolation to higher T_w; subject to the bound $\gamma_i \leq 1$) yield radiation equilibrium temperatures even closer to the corresponding $\gamma = 1$ case. All $T_w(t)$ plots are based on the velocity-altitude trajectory given in Table 5.2-1, and pertain to forward stagnation points (3 dim) or lines (2 dim) on the Orbiter vehicle.

Figure 5.2-2 reveals that for $T_B = 2$ ft (3-dim) both $\gamma_i(T_w)$ and shock layer dissociation effects are quite important in determining the expected T_w-t history[+]. While the potential gains from low γ are sizeable (up to 218K temperature reduction near 800 Sec.) our γ_i data (cf. curve marked γ_{EXP})for the present RPP material suggests only modest (ca. 15K) departures from the corresponding $T_w(t)$ expected for a "perfect" ($\gamma = 1$) atom recombination catalyst. These $\gamma \neq 1$ temperature reductions become even smaller for smaller nose radii, and don't show up in the scale of Fig. 5.2-4. When finite-rate shock layer dissociation is included for $R_B =$ 1 ft., Figure 5.2-3 illustrates that if equilibrium shock layer dissociation were achieved under otherwise identical conditions then $\gamma \neq 1$ temperature reductions would be quite appreciable (cf. Fig. 5.2-1). More detailed computations, including their implications with respect to anticipated RPP mass loss and re-use capability are obviously now possible, and are suggested as valuable extensions of this work. Similarly, the implications of our γ_i-measurements on RSI-coating can now be included in similar formalism, making appropriate allowances (via St_h) for the downstream location of RSI panels on the Orbiter vehicle.

[+] The rapid surface temperature rise predicted for $\gamma = 0$ beyond an elapsed re-entry time of 800sec is primarily caused by the failure to dissociate N_2 in the shock layer as the flight speed decreases. This increase also shows up (in less dramatic fashion) for catalytic surfaces (see curves marked γ_{EXP} and $\gamma = 1$). One concludes that nonequilibrium phenomena strongly influence the shape of the surface temperature vs. time locus during re-entry.

Table 5.2-1

Nominal Trajectories for a 175,000 Lb. Space Shuttle Orbiter[a]

Time (sec)	Altitude (ft)	Velocity (ft/sec)	$-\dot{q}_w''$[b] (btu/ft^2-sec)
0	400,000	25,532	2.05
80	361,189	25,580	4.70
150	325,387	25,623	11.50
235	280,937	25,652	40.57
285	257,516	25,590	76.32
340	243,208	25,347	102.97
373.75	243,255	25,145	100.3
426.25	239,959	24,822	103.5
516.25	236,854	24,214	102.3
616.25	232,115	23,454	102.23
718.75	226,047	22,547	102.18
818.75	218,292	21,478	102.16
908.75	208,646	20,272	102.13
988.75	196,326	18,858	102.13
1033.75	192,475	17,868	92.59
1101.25	188,225	16,433	76.98
1198.75	180,937	14,347	57.36
1376.25	164,392	10,567	29.59
1496.25	150,310	8,029	16.47
1596.25	136,186	5,940	8.61
1675	122,026	4,330	4.37
1767.5	105,271	2,679	1.43
1805	94,487	2,124	.89
1851.5	80,000	1,495	.41

---

a. 040A MK II polar entry trajectories of 11/19/71; high cross range, $\alpha = 30°$; supplied by C.D. Scott, 31 August 1972.

b. $-\dot{q}_w''$ is the fully catalytic heating rate to a 1-foot radius "reference" sphere.

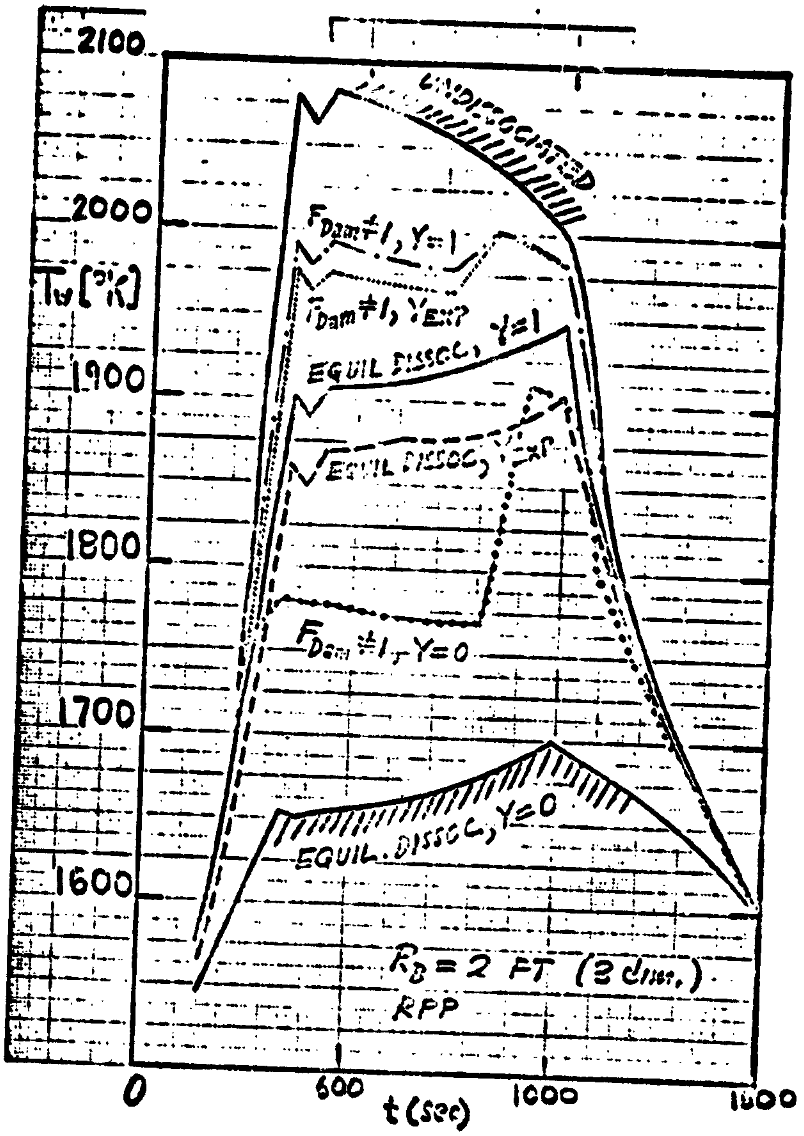

5.2-2 Predicted surface temperature vs. time during the re-entry of a 2 ft. nose radius orbiter vehicle with RPP nose cap.

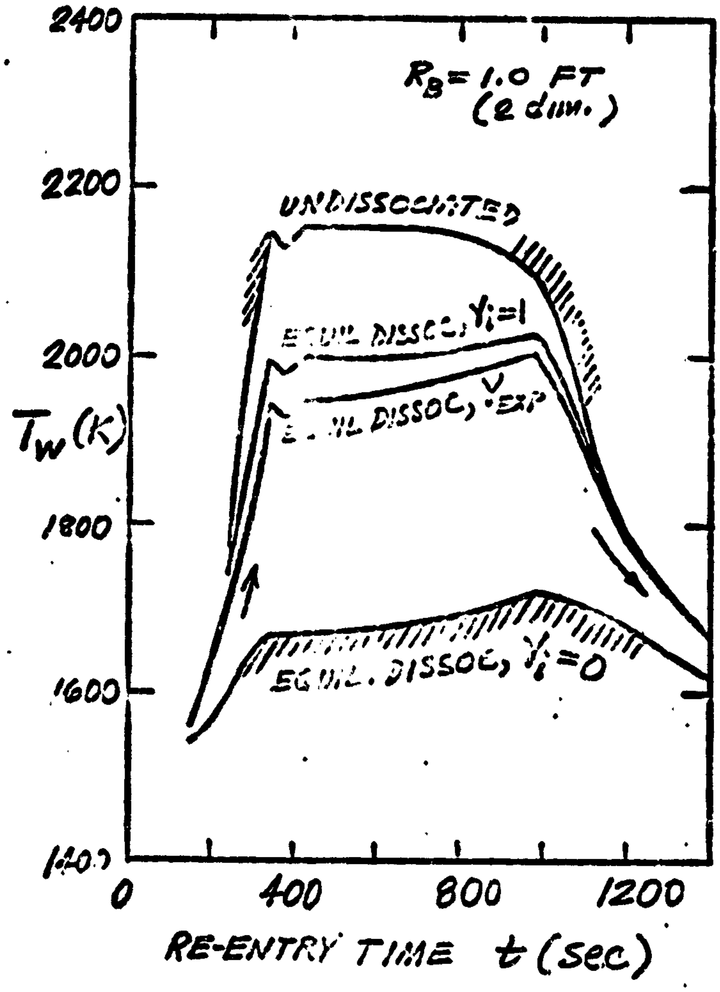

5.2-3 Predicted surface temperature vs. time during re-entry for a 1 ft. nose radius, unswept 2-dimensional leading edge of RPP material; $\gamma_{dam,i}$-limiting cases

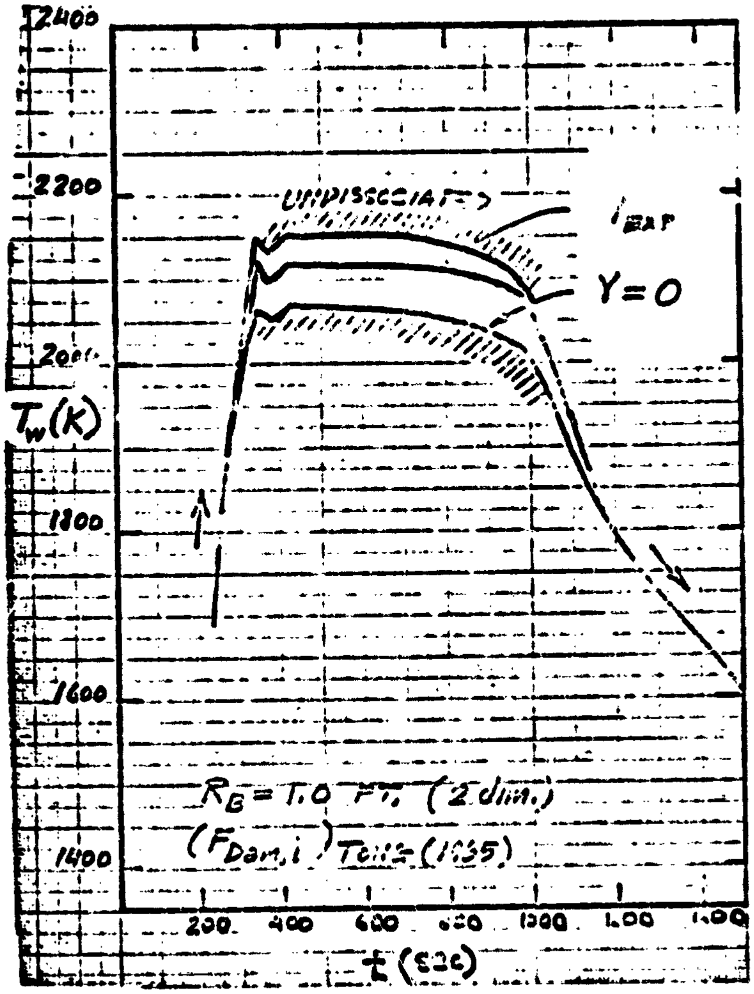

5.2-4 Predicted surface temperature vs. time during re-entry for a 1 ft nose radius, unswept 2-dimensional leading edge of RPP material; $F_{Dam,i}$ calculated using the modified Tong (1965) correlation.

5.3 Previously Unconsidered Chemical Events Which Could Modify the Rate of Energy Transfer to the Vehicle Surface

In keeping with our goal of developing reliable and convenient methods for predicting vehicle surface temperatures in terms of $\gamma_O(T_w)$-and $\gamma_N(T_w)$-data we have initiated quantitative studies of two interesting and potentially important processes. Both classes of processes discussed in this subsection in effect require the relaxation of assumptions underlying the aerodynamic heating method outlined in Section 5.1. The assumptions in question are:

a) the energy released per gram of recombining atoms i (i=O,N) is $Q_i \cong \Delta H^\circ_{f,i}(T_w)/M_i$ where $\Delta H^\circ_{f_i}(T_w)$ is the equilibrium heat of the atom formation reaction at the prevailing surface temperature T_w

b) under glide re-entry conditions the viscous boundary layer may be considered "chemically frozen" with respect to gas phase atom recombination reactions

We are motivated to examine the first of these assumptions since recent low pressure ($p \leq 1$ torr) surface recombination experiments [Harteck et al. (1960,1964), Wood et al. (1963, 1967), Melin and Madix (1971)] indicate that in some cases only a small fraction of the equilibrium heat of recombination is released at the catalyst surface. Thus, in Section 5.3.1 we briefly[+] address the question: what do these low-pressure laboratory studies imply with respect to the expected level of aerodynamic heating of hypersonic glide re-entry vehicles ?

The second of these assumptions has traditionally been based on order-of-magnitude recombination-time estimates carried out for a pseudo-binary (atom "A" + molecule "M") partially dissociated gas, recombining by a

---

[+] For a more detailed treatment, see Rosner and Feng (1973)

3-body process, eg.

$$A + A + M' \rightarrow M + M' \qquad (5.3\text{-}1)$$

However, in considering the interpretation of our recombination coefficient measurements carried out in O + N mixtures (see Section 2.3) it occurred to us that the following sequence of 2-body processes in the boundary layer could influence the wall energy transfer:

$$N + O_2 \rightarrow NO + O \qquad (5.3\text{-}2)$$

$$N + NO \rightarrow N_2 + O \qquad (5.3\text{-}3)$$

since, in effect, they can "undo" surface-catalyzed O-atom recombination and replace it by the more exothermic formation of N_2. Our assessment of the possibility and influence of these homogeneous reactions in partially dissociated <u>air</u> is given in Section 5.3.2 below.

5.3.1 Role of Surface-Catalyzed Production of Excited Molecules

Implicit in the analysis of Section 5.1 is the assumption that the atom recombination event statistically leads to diatomic molecules in thermochemical equilibrium with the surface. However, atom recombination on some surfaces evidently leads to the production of excited molecules (see the abovementioned references). Clearly, if these excited molecules could escape the boundary layer without being "quenched" the energy transferred to the catalytic surface would be less than if the catalyst had produced molecules with the local thermodynamic equilibrium (LTE) distribution of internal energy states [Rosner (1962b)]. Indeed, at least partial escape must have occurred in the low pressure experiments cited above, since the observable was the energy transfer to calorimeter surfaces exposed to a known atom concentration. To determine whether this can occur in the orbiter re-entry environment it is necessary to better understand the details of the quenching process. For this purpose we have carried out a "conductivity-cell" analysis in the spirit of [Rosner (1963)] in which a) a well-defined electronically excited state (designed by M^*) is produced with probability s^* per recombination event ($s^* < 1$), b) this state, with energy level Q_{M^*} (per gram) above the ground state molecule, is quenched either by gas phase collision (with 2-body rate constant k_q) within the "cell" of thickness δ or by encounter with the wall (wall quenching probability γ_q), c) atom recombination occurs only at the wall, with probability γ. Since the details of this analysis are included in a recent paper [Rosner and Feng (1973)] only the principal results and conclusions are presented here.

The role of the parameters $\mathcal{H}$ (see Section 5.1) s^* and Q_{M^*}/Q_A (where Q_A is the LTE heat of ground state atom recombination) is readily appreciated by first considering the limiting case of neither gas phase nor wall quenching. Then, for a single recombining species:

$$\frac{-\dot{q}''_w}{-\dot{q}''_{w,min}} = 1 + (1 - s^* \cdot \frac{Q_{M^*}}{Q_A}) \cdot \phi \mathcal{H} \qquad (5.3\text{-}4)$$

where $-\dot{q}''_{w,min}$ is the corresponding aerodynamic heat flux to a non-catalytic material. Since N_2 dissociation in the shock layer of the orbiter vehicle may be sluggish (see Section 5.1) it is of interest to apply Eq.(5.3-4) to the production of $O_2(^3\Sigma_u^+)$ via surface-catalyzed O-atom recombination[+]. In this case $Q_{M^*}/Q_A = 0.875$ and, for conditions near orbiter peak heating ($Z = 240$Kft, $U = 24$ Kfps) we estimate $\mathcal{H}_0 = 0.73$). If we now compare two tive recombination catalysts ($\phi = 1$), only one of which produces $O_2(^3\Sigma_g^+)$ upon every recombination event, then, in the absence of localized quenching, we find

$$\frac{(-\dot{q}''_w)_{s^*=1}}{(-\dot{q}''_w)_{s^*=0}} = \frac{1 + (1-0.875) \cdot (0.73)}{(1+0.73)} = 0.63 \qquad (5.3\text{-}5)$$

[+] Values of $Q_{0,eff}/Q_0$ reported by Melin and Madix (1971) for Au,Fe,Ni,Pt and W are low enough to correspond to $s^* = 1$ (to within experimental error) for the production of $O_2(^3\Sigma_u^+)$

Since the radiation equilibrium temperature is approximately[†] proportional to $(-\dot{q}_w'')^{1/4}$ (cf. Section 5.1) under conditions for which $(T_w)_{s^*=0}$ is about 1900K the value of $(T_w)_{s^*=1}$ would therefore be about 1700K, yielding about 200K local "saving" for a "perfect" catalyst (say $\gamma_0 \gtrsim 10^{-1}$) producing $O_2\,({}^3\Sigma_u{}^+)$ on every recombination event.

This situation can be altered considerably in the presence of appreciable wall quenching or gas phase quenching [Rosner and Feng (1973)] Even if the overall homogeneous quenching rate constant k_q is as large as that for $O_2({}^1\Sigma) + N_2(g)$ we find that the parameter $\mathcal{L}_{eff}$, defined by

$$\mathcal{L}_{eff} \equiv \left[1 + \omega_{A,e} \cdot \left(\frac{1 + \frac{1}{2}\mathcal{W}_A}{1 + \mathcal{W}_A}\right)\right]^{-1} \cdot \left[\frac{1}{2}\left(1 + \frac{T_w}{T_e}\right)\right]^{-3/2} \cdot \mathcal{L} \qquad (5.3\text{-}6)$$

where

$$\mathcal{L} \equiv \frac{k_{q,w}\delta}{D_{M^*}\rho} \cdot \frac{N}{M_M} \left(\frac{pM_M}{RT_w}\right)^2 \left(\frac{T_w}{T_e}\right)^{3/2} \qquad (5.3\text{-}7)$$

is only of the order of 10^{-1}, so that wall quenching would appear to be the more likely quenching mechanism under these conditions [‡]. Available experimental data on the excited molecule wall quenching probability γ_q are sparse, even for $O_2({}^1\Sigma_g{}^+)$. Since the ratio of γ_q to the atom recombination probability γ for $O_2({}^1\Sigma_g)$ quenching on room temperature pyrex is evident slightly larger than 10, we examined the effect of setting $\gamma_q/\gamma = 15$ in the following equation, applicable in the limit of negligible gas phase quenching:

[†] More exactly, $T_w \sim (-\dot{q}_w'')^{1/n}$ where n is the local value of $d(\ln \varepsilon_w \sigma T_w^4)/d\ln T_w$ [see, eg. Rosner (1964a)]. Thus, n=4 only for the case of constant emittance.

[‡] Our procedures for estimating the effective values of gas film thickness, δ, and the chemical enthalpy parameter $\mathcal{W}$ are identical to those given by Rosner (1963)

$$\frac{-\dot{q}''_w}{-\dot{q}''_{w,\min}} = 1 + \left[1 - s^* \cdot \frac{Q_{M^*}}{Q_A} \cdot \frac{1}{1 + \frac{1}{\sqrt{2}} \left(\frac{\gamma_q}{\gamma}\right) \cdot \left(\frac{D_A}{D_{M^*}}\right)_w \mathcal{W}} \right] \cdot \phi H \quad (5.3\text{-}8)$$

Combining these estimates, we find that if $s^* = 1$ a minimum value of $-\dot{q}''_w/(-\dot{q}''_{w,\max})$ of (only) about 0.97 is attained at $\phi = 0.11$. Comparing two catalysts with $\phi = 0.11$ under these conditions we find that, if $s^* = 1$, $T_w = 1670$K, whereas if $s^* = 0$, $T_w = 1690$K. Since $0 \leq s^* \leq 1$, we see that unless much smaller values of γ_q/γ are relevant, the maximum surface temperature reduction to be expected from oxygen atom recombination to energetic excited molecules (eg. $O_2(^3\Sigma_u^+)$ rather than ground state molecules) is only about 20K. Interestingly enough, while γ_q/γ appears to be much smaller for $O_2(^1\Delta_g)$ quenching on pyrex, the energy transfer effects of recombination to $O_2(^1\Delta_g)$ are also smaller since Q_{M^*}/Q_A is only 0.192, again leading to temperature reductions of some 20K. We tentatively conclude that wall temperature predictions neglecting the phenomenon of oxygen atom recombination to metastable electronically excited molecules will only slightly overestimate T_w†. Hence the use of available γ-data and the (previously implicit) assumption $s^* = 0$ is not likely to be overly conservative unless surfaces with $s^* = 1$ and small γ_q/γ for very energetic metastable molecules are encountered. Only if reasonably low γ_q surfaces could be found which, say, produce $O_2(^3\Sigma_u)$ molecules with $s^* = 1$ and with much lower wall quenching probabilities than Pyrex would this conclusion be altered.

Corollaries of our theoretical model relevant to the inference of γ based on differential energy flux measurements in the laboratory are included in the full-length paper of Rosner and Feng (1973). Thus, in the presence of recombination to excited molecules, values of γ previously determined from differential energy flux measurements under continuum conditions would be low by a calculable amount dependent upon s^* and the kinetics of excited molecule quenching; see, eg. Section 5.4.

---

† If vibrationally excited molecules were produced at surfaces during atom recombination the present formulation would retain many of its present features, however a more detailed homogeneous quenching model (accounting for the large number of "species" of various energy levels) would be required.

5.3.2 Influence of Bimolecular Exchange Reactions on Energy Transfer to Solids in Dissociated Air

In addition to the obvious possibility of direct recombination to N_2, the presence of atomic nitrogen formed in the shock layer can cause a) the surface-catalyzed formation of NO(g), and b) the gas phase conversion of NO(g) and O_2(g) to N_2 via Reactions (5.3-2,3) (See Fig. 5.3-1). Since these processes can be important even when the three-body homogeneous recombination ($N + N + M \rightarrow N_2 + M$) proceeds at a negligible rate, it is prudent to consider their energy transfer consequences under glide re-entry vehicle conditions. To our knowledge no assessments of this type have previously been reported in the aerospace literature.

Rather than divert too much attention from our principal goal of γ_O, γ_N determinations and their aerodynamic heating implications, we decided to estimate as simply as possible the heat transfer effects of Reactions (5.3-2,3) under conditions of nominally peak heating. The "worst case" was treated - ie. $\omega_{N,e} = \omega_{N,e;eq}$ to maximize the N-atom concentrations "available" for the abovementioned gas reactions. Since little is currently known about the kinetics of surface-catalyzed NO(g) production in dissociated air, our preliminary analysis is confined to the limiting case in which the only source of NO(g) is that due to Reaction (5.3-3) occurring near the O-atom recombination catalyst. Indeed, we concluded that a simple but useful quantitative analysis of the effects of these reactions could be carried out under the simplifying assumption that these reactions are rapid enough to be considered "pseudo-heterogeneous". This implies that they take place in a chemical "sublayer" of thickness δ_{chem} small compared to the total diffusion boundary layer thickness, δ. As indicated below, the "pseudo-heterogeneous" hypothesis leads to a very simple algebraic model of species transport across the predominantly "frozen" boundary layer. In addition to yielding the expected trends, the results of this model will be shown to amply justify more detailed studies of these kinetic phenomena in the future. Ultimately, it is

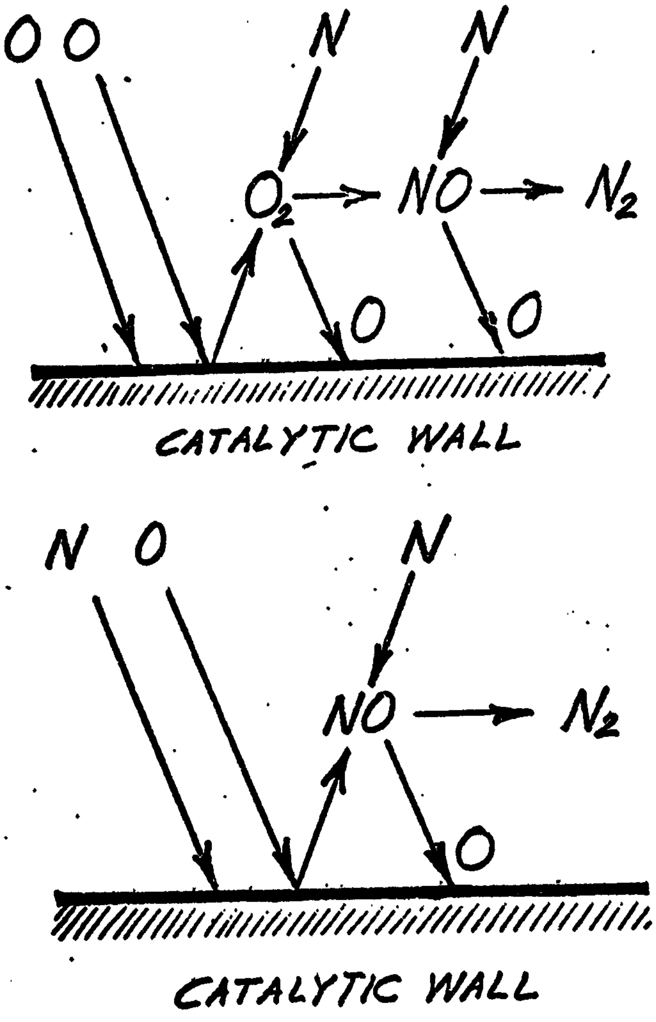

5.3-1 Bimolecular N-atom reactions within the boundary layer possible that these effects could be routinely included in aerodynamic heating calculations by treating them as pseudo-heterogeneous. Once rigorous nonequilibrium boundary layer solutions are available and correlated in this way, this approach would be closely akin to that of Chung and Liu (1963), who represented the effects of gas phase atom recombination by an expression in terms of an *effective* (fictitious) heterogeneous rate process. In the present section our approach is intrinsically different, since we seek to make *ab initio* estimates of an effect of gas phase reactions, in the absence of more rigorous calculations including these effects.

By assuming the NO diffusion term and homogeneous chemical sink term (due to Reaction (5.3-3)) are in approximate balance within the "chemical sublayer" we obtain the following estimate for δ_{chem}

$$\delta_{chem} = \left[\frac{(M_N/N) \cdot D_N \cdot (\omega_{NO,w} - \omega_{NO,e})}{\rho_w k_3(T_w) \cdot \frac{1}{2}(\omega_{NO,w} + \omega_{NO,e}) \cdot \omega_{N,w}}\right]^{1/2} \qquad (5.3\text{-}9)$$

where $\delta_{chem} \ll \delta$. Then, by equating the actual reaction rates *within* δ_{chem} to their pseudo-heterogeneous counterparts, when $\omega_{NO,e} = 0$ we estimate

$$k_{3,w;eff} = \frac{1}{2} \cdot k_3 \delta_{chem} \qquad (5.3\text{-}10)$$

$$k_{2,w;eff} = k_2 \delta_{chem} \qquad (5.3\text{-}11)$$

Then we write 4 simultaneous algebraic equations in the 4 unknowns $\omega_{i,w}$ ($i = O, O_2, NO, N$) by re-expressing the species balance equations:

$$\begin{matrix}\text{(real + pseudo)-heterogeneous} \\ \text{"source" strength} \\ \text{per unit surface area}\end{matrix} = \left[\frac{\overline{D_i \rho}}{\delta} \cdot (\omega_{i,w} - \omega_{i,e})\right] \qquad (5.3\text{-}12)$$

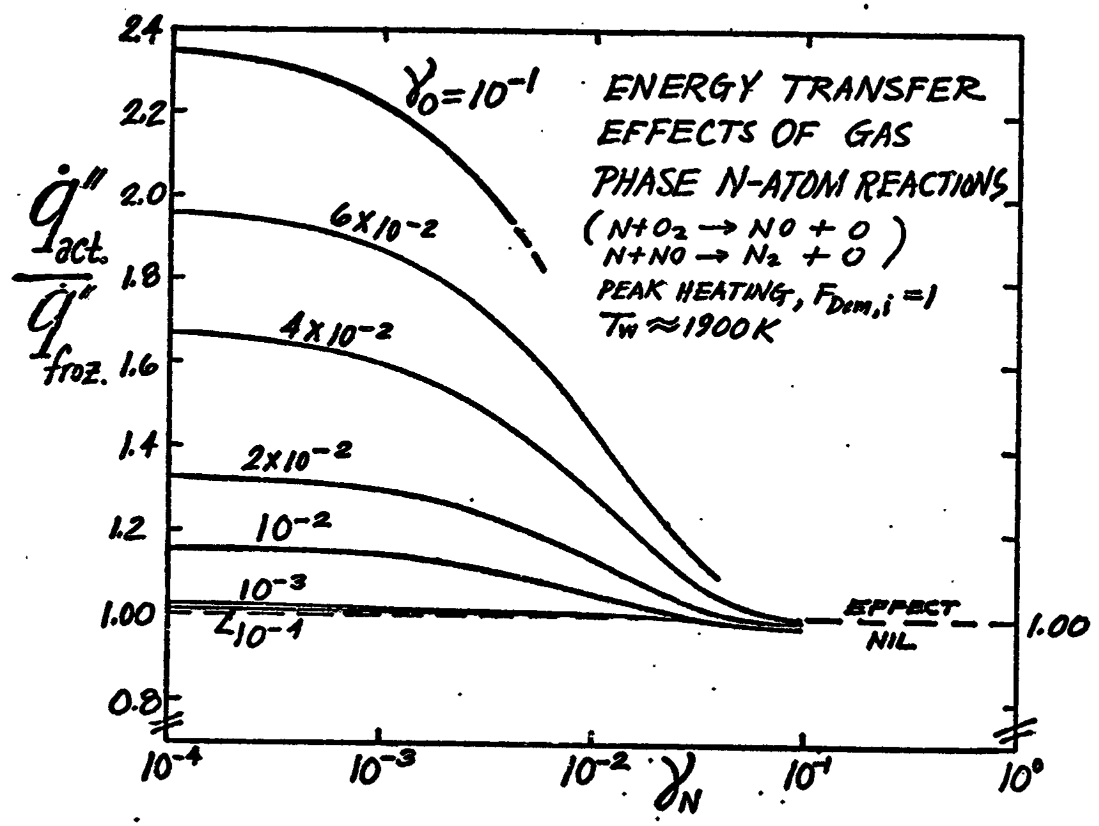

5.3-2 Energy transfer effects of bimolecular gas phase N-atom reactions under conditions of peak aerodynamic heating.

These are solved iteratively for the $\omega_{i,w}$, from which the energy flux is estimated using:

$$-\dot{q}_w'' = \bar{\lambda} \cdot \frac{T_e - T_w}{\delta} + \sum_{i=O,N,NO} \frac{\overline{D_i \rho}}{\delta} \cdot (\omega_{i,e} - \omega_{i,w})\, Q_i \qquad (5.3\text{-}13)$$

Illustrative calculations of $-\dot{q}_w''$ using this approach were carried out for the case: $Z = 240$ kft, $U = 24$ kfps, $R_B = 1$ ft, $F_{Dam,N} = 1$, $T_w = 1900K$ with the results shown in Fig. 5.3-2. To minimize the effects of uncertainties in mean gas properties $(\bar{\lambda}, \overline{D_i \rho})$ and total boundary layer thickness, δ, we have displayed the ratio of $(-\dot{q}_w'')$ - "actual" (including the pseudo-heterogeneous N-atom reactions) to $(-\dot{q}_w'')$ - "frozen" (the energy flux computed neglecting gas phase reactions but under otherwise identical conditions). Only results for which δ_{chem} is less than 0.2δ are included, and the values of k_2, k_3 (expressed in $cm^3 molec^{-1} sec^{-1}$) were taken to be [Prud'homme and Lequoy (1969)]:

$$k_2(T) = 2.16 \times 10^{-14}\, T \cdot \exp\left(-\frac{7080}{RT}\right) \qquad (5.3\text{-}14)$$

and

$$k_3(T) = 2.22 \times 10^{-13}\, T^{1/2} \qquad (5.3\text{-}15)$$

respectively (where T is in degrees Kelvin). The values of γ_O, γ_N were taken to be parameters, as it was expected that the effects of these bimolecular exchange reactions would be greatest when γ_O is large (to produce considerable O_2) and γ_N is small (to consume the least possible amount of N *via* the *true* heterogeneous recombination reaction).

The results shown in Fig. 5.3-2 bear out these expectations and reveal surprisingly large energy transfer effects - up to a factor of ≈ 2.3 for the worst case shown[†] ($\gamma_O = 10^{-1}$, $\gamma_N = 10^{-4}$). Evidently, only if $\gamma_O < 10^{-3}$ or γ_N exceeds about 10^{-1} would a simple "frozen" estimate of the energy

---

[†] This would correspond to about a 450K increase in radiation equilibrium temperature compared with the corresponding "frozen" boundary layer prediction.

transfer rate prove reasonable. Thus, based on this admittedly simple computational model, we conclude that under glide re-entry conditions for which N-atoms are formed in the shock layer, the influence of bimolecular N-atom exchange reactions within the boundary layer should be included in future predictions to avoid possible serious underestimates of the aerodynamic heating rate to radiation-cooled solids which catalytically recombine O-atoms. However, our high temperature γ_N experiments on siliconized RPP (cf. Fig. 2.3-3) and $F_{Dam,i}$-predictions for nose radii of the order of 1 ft. suggest that this effect will not be important for the present leading edge material.

5.4 The Disparity Between γ Inferred from Duct Reactor Tests and γ Inferred from Arc Jet Tests

Based on a series of air arc jet tests in which the brightness temperatures of coated and uncoated radiation cooled RPP specimens were compared under identical flow conditions it was concluded [LTV (1971, 1972)] that the inhibited RPP surface ran cooler because γ was of the order of only 10^{-2} at $T \approx 1900$-2100K. Inspection of Fig. 2.3-3 reveals that this inference conflicts sharply with our conclusion that the coated RPP surface is quite catalytic to O- and, especially, N-atom recombination at these temperatures. While the absolute accuracy of our γ determinations above 10^{-1} is compromised by the need to make appreciable diffusion corrections (see Section 2.2) the resulting uncertainty does not affect our basic conclusion that the RPP coating is an active recombination catalyst above about 1500K. Since arc jet testing plays such an important role in the aerospace materials screening/selection process, it is important that the causes of this disparity be investigated further. Of particular concern is the question of whether current arc jet test procedures might lead to overly optimistic conclusions regarding the behavior of such materials in nonequilibrium air environments. A detailed investigation of possible systematic errors and unaccounted for effects in available laboratory techniques is obviously necessary (cf. Section 6.2), and could lead to test methods and flight predictions of greatly increased reliability. For the present, we briefly considered the following assumptions implicit in the arc-jet inference of γ

1. The total and spectral emittance of bare and coated RPP are comparable (ca. 0.85)
2. Bare RPP in dissociated air achieves essentially the same surface temperature as a hypothetical perfect catalyst of the same total emittance.
3. The heat released per recombination event is the equilibrium heat of atom recombination at the prevailing surface temperature (see Section 5.3.1)

Assumption 1 is important since coated RPP could appear to run cooler (via optical pyrometry) merely because its spectral emittance is lower than assumed. Assumption 2 bears examination since coated RPP could appear to run cooler than bare RPP because of the highly exothermic surface combustion of bare RPP in dissociated oxygen[+]. Assumption 3 focuses attention on the fact that the arc-jet inference of γ is based on an energy transfer estimate rather than an atom balance. Since energy transfer is of ultimate interest this would appear to be an advantage, were it not for the fact that the energy transfer inference of γ is scale (size) dependent and apt to be non-conservative when applied to flight-scale hardware [Rosner and Feng (1973)].

Even introducing a spectral emittance 0.25 (for 2100K coated RPP at $\lambda = 6650\mathring{A}$) and a total emittance 0.6 (for 2100K coated RPP) [preliminary data of R. Wakefield (1973)] we calculated that the combined effects of assumptions 1 and 2 would raise the arc-jet inferred γ by no more than a factor of about 3 to 4-fold, leaving a considerable disparity between the arc jet and duct reactor γ-values. Moreover, our XPS data on arc jet and duct reactor exposed specimens suggest that this disparity cannot be attributed to significant differences in the <u>in situ</u> surface chemistry under the temperature conditions of our γ-measurements.

Assigning the cause of the disparity to assumption 3 is intriguing but would be premature in view of the lack of experimental data on "incomplete energy accomodation" on catalytic solids in N-atom atmospheres. Yet this phenomenon should be pursued further since minor changes in the present RPP coating (eg. elimination of, or substitution for, Al_2O_3) might lead to significant in-flight temperature reductions when materials of this type are applied in regions of large effective nose radius (eg. the fuselage nose-cap, or belly panels).

[+] This possibility has evidently been considered and rejected by J. Medford [LTV (1971)], whose unpublished calculations suggested that the heat of combustion is offset by the blowing effect on the transfer coefficient associated with the mass loss process.

6. CONCLUSIONS AND RECOMMENDATIONS

In the light of the contents of Sections 2-5, it may be said that our principal objectives have been achieved as a result of this one-year technical effort. These include:

a. development of a duct flow reactor technique to determine the atom recombination coefficients γ_O and γ_N above 1000K for flat, nonconducting thermal protection system materials with γ-values in the range of aerodynamic heating interest (Section 2.1,2.2)

b. demonstration of the applicability and utility of X-ray photoelectron spectroscopy (XPS) to chemically characterize the surface of candidate thermal protection system materials before and after exposure to dissociated oxygen and/or nitrogen (Section 4.1)

c. development of a rational, yet practical method to predict the aerodynamic heating consequences of laboratory measurements of atom recombination coefficients and the accompanying energy transfer (Section 5).

6.1 Conclusions

Specific important conclusions that have emerged from these laboratory and theoretical investigations are best itemized as follows:

A. Duct Flow Reactor γ-Measurements

*The surface of siliconized carbon carbon - reinforced pyrolyzed plastic(hereafter designated RPP) constitutes a surprisingly active catalyst for the recombination of O atoms and N atoms at surface temperatures above 1000K. γ-values computed from our experiments all exceed 2×10^{-2}, and at temperatures above 1370K, the atom recombination coefficient for O or N atoms on the surface exceeds 10^{-1}. As a corollary to this, in flight as in our duct, and especially for RPP, non-negligible atom concentration gradients (normal to the catalyst surface) will always exist at these temperatures. Thus, any high atom pressure (continuum)

RPP γ-measurements will require a "diffusion correction" limiting its absolute accuracy.

*In the 1030-1710K temperature range investigated, N and O atom loss by recombination on RPP coating exceeds the corresponding loss by chemical combination with the surface by more than 5-fold.

*Inferred N-atom recombination coefficients on RPP coating are larger than corresponding O-atom recombination coefficients by about 2-3 fold over most of this temperature range (1030-1710K)

*While γ_O and γ_N-values on the coating of the re-usable surface insulation material (RSI) below about 1000K are not very different from the corresponding values for RPP, in contrast to the latter, γ_O and γ_N appear to level off and pass through a shallow maximum ($< 10^{-1}$) near 1300K.

*In contrast to RPP, γ_O exceeds γ_N on RSI (by a factor of the order of two) in the temperature range 985 - 1460K. Thus, the fact that γ-values on RPP exceed those on RSI above about 1300K cannot be attributed to differences in roughness alone, and may be due to the Al_2O_3 content of the RPP coating.

B. RPP Mass Loss Experiments

*The mass loss behavior of RPP in oxygen (ca. 10^{-2} to 5×10^{-2} torr) is very different from that of pure, dense β-SiC. This is especially marked at temperatures below about 1900K, where the oxide formed on RPP is relatively nonprotective and easily removed by physical means. This difference is not exclusively due to the presence of Al_2O_3 in the RPP coating, since it persists after the surface layer containing Al_2O_3 is removed by the ablation process (cf. XPS evidence below)

*In contrast to pure, dense β-SiC the RPP ablation process below 2000K is not impeded in O + N mixtures (relative to the corresponding rates in O alone)

C. Chemical/Physical Characterization of Surface

*XPS investigation of RPP surfaces exposed to O or O_2 at moderate temperatures (in the range 1410 - 1620K) reveal that all of the surface silicon is present in the form of SiO_2(c). In addition, aluminum is present (as an oxide). This aluminum is lost during the initial states of reaction above 1700K by physical removal of the aluminum oxide phase. N-atoms are also effective in removing this finely divided carbon.

*Finely divided carbon (formed by the decomposition of SiC) exists on the surface of RPP during 10^{-2} torr O_2 exposure at T > 1800K. Under these conditions the ablation behavior of siliconized RPP is probably poorer than that of pure graphite.

* At temperatures below the Si_3N_4 or Si_2ON_2-loss threshold (1820 < T < 2030K) nitrogen is incorporated into the RPP surface upon exposure to gas containing ca. 10^{-2} torr of atomic nitrogen.

*Below 1500K all observable silicon on the RSI surface is in the form of SiO_2, indicating that the SiC content of the coating is "buried" or that SiC constitutes < 10 atom pct. of the surface layer.

*Arc jet exposed RSI surfaces frequently exhibit the contaminant element aluminum that very likely influence the catalytic nature of the surface.

*SEM studies of the RSI coating reveal that while the virgin surface is smooth and featureless, temperature cycling at 1100K gives rise to blistered surfaces, revealing high temperature gas evolution. Temperature cycling at 1600K leads to a very rough surface.

*SEM studies of RPP exposed to oxygen at high temperature reveal very rough surfaces from which the SiO_2(c) is easily removed mechanically.

CONCLUSIONS

D. Aerodynamic Heating of Hypersonic Glide Re-entry Vehicles

*If dissociation-equilibrium were achieved in the shock layer of hypersonic glide vehicles with a trajectory similar to that of the Space Shuttle Orbiter then the temperature reduction realized by the use of a noncatalytic ($\gamma_O \leq 10^{-3}$, $\gamma_N \leq 10^{-3}$) rather than a catalytic (γ_O, $\gamma_N > 3 \times 10^{-1}$) coating approaches 400K. Owing to the sensitivity of RPP-coating ablation rate to surface temperature even small changes in radiation equilibrium temperature will strongly influence the re-use capability (number of missions between refurbishment) of the materials system [cf. LTV (1972)].

*The kinetics of N_2 dissociation in the shock layer of the Orbiter vehicle are slow enough to significantly reduce the benefits of using low γ-materials on radiation-cooled vehicles, especially in regions of small stagnation point radius. The combined effects of small nose radius and sweepback should make γ_N for the wing leading edge material far less important than the corresponding values of $\gamma_N(T_w)$ for the nose cap and fuselage belly panels. Reduced temperatures of these locations would imply greatly increased re-use capability for fixed weight and coating thickness.

*For nose radii of the order of 1 foot only surface-catalyzed O atom recombination may be important, and the potential benefit of noncatalytic materials is some 60K. Larger benefits (> 200K reduction on radiation equilibrium temperature) are possible when $R_B > 1$ ft owing to the formation of N atoms in the stagnation region shock layer, however, these are not likely to be realized using the present RPP leading edge/nose cap material. Our γ-measurements suggest that, for $R_B = 2$ft, RPP would run only some 15-20K cooler than a "perfect" catalyst during about 60% of the re-entry heat pulse. This difference would ultimately vanish during the last 40% of the heat pulse (Section 5.2)

*A noncatalytic refractory coating used where R_B is sufficiently large would not only reduce peak wall temperatures by more than 200K - it would also have the effect of altering the <u>shape</u> of the $T_w(t)$ "pulse" from one which is very high and plateau-like, to one which first exhibits a "low temperature" plateau followed by a temperature rise (some 130 - 140K) accompanying N_2 dissociation limitations later in the re-entry (Section 5.2).

- The phenomenon of wall quenching is likely to annhilate any significant heat transfer reduction that would result from surface-catalyzed atom recombination to form excited (rather than ground state) molecules under re-entry conditions (Section 5.3.1). However, it is possible that the escape of excited N_2 molecules formed by surface catalyzed N-atom recombination could account for a significant portion of the surface temperature differences observed in a high enthalpy air arc jet when inhibited RPP is compared with bare RPP (Section 5.4). Thus, present arc jet test predictions of surface temperatures during re-entry, and hence re-use capability, may be overly optimistic.

- While 3-body reactions may be "frozen" within the boundary layer, under glide re-entry conditions for which N-atoms are formed in the shock layer, the influence of bimolecular N-atom exchange reactions within the boundary layer should be included to avoid underestimating the radiation equilibrium temperature of O-atom recombination catalysts (Section 5.3.2)

6.2 Recommendations

Potential reductions in radiation equilibrium temperature (>200K) due to reduced catalytic activity, and their implications with respect to extended re-use capability especially for the nose cap and possible fuselage belly panels, are large enough to justify further research on:

a. The phenomena causing large systematic differences between γ inferred from energy balance methods (e.g. in arc jets) and γ inferred from atom mass balance methods (cf. Section 5.4). Evaluation of the consequences for laboratory simulation of materials response in nonequilibrium dissociated air.

b. Since a truly non-catalytic (γ=0) coating is an unattainable ideal, and since the large observed differences between γ_0, γ_N for the RPP-coating and the RSI-coating may be due to to the Al_2O_3 content of the former, it would be useful to determine γ_0 and γ_N on pure SiO_2 at surface temperatures above 1500K (using a chemically compatible refractory substrate) in our duct flow reactor (cf. Section 2).

c. The causes of large activity for present generation coatings, including high temperature γ_0, γ_N measurements on important coating constituents (eg. $Al_2O_3(s)$), and a better definition of the role of surface topography (roughness).

d. High temperature measurements of γ_0 and γ_N on well-defined refractory ceramic materials likely to be useful in the future U.S. hypersonic vehicle development.

e. Measurements of the effects on γ_0, γ_N of small element additions to ceramic coatings (ie. "doping" effects on catalytic activity)*

f. The interacting effects of physical, chemical and aerodynamic phenomena in determining expected surface temperatures and ablation rates for radiation-cooled glide re-entry vehicles. Further development/exploitation of the predictive methods of Section 5.

g. Gas uptake-loss phenomena in temperature-cycled amorphous coatings; the causes, consequences and prevention of surface blistering.

---

* For example, doping the present RPP coating with B, Al or Ti to suppress crazing is under consideration [LTV (1973)].

To the largest extent possible, further research should be directed at obtaining a better basic understanding of the subtle chemical and physical factors governing the magnitude of γ and energy release on chemically and physically well-defined refractory surfaces. This will require increased attention to materials other than currently manufactured TPS coatings, a longer-range viewpoint and a more systematic approach. The goal should be to provide a scientific <u>foundation</u>† and set of applicable <u>techniques</u> to guide future design choices in the realm of hypersonic flight. Results of this type would also inevitably find application in many other technical areas in which dissociated gases interact with refractory solids.

---

† The extent to which our present program exploited results available from the author's previous long-range basic research is clear from the content of Sections 2-5. Without this background, the results reported here could not have been achieved in a one-year period, even at considerably greater cost.

7. REFERENCES

Anderson, L.A. (1973) AIAA J. 11, 649-656

Baer, Y. et al. (1970) Solid State Communication 8, 1479

Barber, M., Evans, E.L., Thomas, J.M. (1973) Chem. Phys. Lett. 18, 423

Bartlett, E.P. , Grose, R.D. (1969) Sandia Laboratories Report SC-CR-69-3207

Berkowitz-Mattuck, J.B. (1969) Paper No. 80 in The Structure and Chemistry of Solid Surfaces, J. Wiley, New York

Bird, R.B. et al. (1963) Transport Phenomena, J. Wiley, New York

Blottner, F.G. (1969) AIAA J. 7, 2281-2288

Boison, J.C., Curtiss, H.A. (1959) ARS J. 29, 130-135

Breen J. et al (1972) "Catalysis Study for Space Shuttle Vehicle Thermal Protection Systems" Tech. Prog. Report No. 1 to NASA Spacecraft Center, Houston, Texas

Breen J. et al. (1973) "Catalysis Study for Space Shuttle Vehicle Thermal Protection Systems" Tech. Prog. Report No. 2 to NASA Spacecraft Center, Houston, Texas

Brundle, C.R., Roberts, M.W. (1972) Proc. R. Soc. Lond. A331, 383-394

Busing, J.R. (1964) Proc. 5th Fluid Dynamics Transactions, 1, 143-159 MacMillan Co., New York

Carden, W.H. (1966) AIAA J. 4, 1704-1710

Carlson, T.A. (1972) Electron Spectroscopy, Northholland Pub. Co. Amsterdam

Cheng, H.K. (1963) Cornell Aeronautical Lab. Report AF-1285-A-10

Chung, P.M., Liu, S.W. (1963) AIAA J.1,#4, 929-931

Chung, P.M. (1961) NASA Technical Report R-109

Chung, P.M., Anderson, A.D. (1961) NASA TND-350

Chung, P.M. et al.(1968) AIAA J. 6, 2372-2379

Clyne, M.A.A., Thrush, B.A. (1962) Proc. Roy. Soc. 269, 404

Deriugin, V. et al. (1964) Boeing Co., Doc. No. D223253, DDC AD 442 005

Dickens, P.B., Sutcliffe, M.B. (1964) Trans. Faraday Soc. 60, 1272-1285

Dorrance, W.H. (1962) Viscous Hypersonic Flow, McGraw-Hill, New York

Drew, C.M. (1968) Proc. of the Symposium on Scanning Electron Microscope, Chicago

Fontijn, A., Meyer, C.B. and Schiff, H.I. (1964) J. Chem. Phys.40, 64

Fraser, W.A. Florio, J.V. Delgass, W.N. and Robertson, W.D. (1973) Surface Science 36, 661

Goldstein, H.E. et al (1972) NASA TMX 2570

Goulard R.J. (1958) Jet Propulsion 28, 737-745

Greaves, J.C., Linnett, J.W. (1959) Trans. Faraday Soc. 53, 1355-1361

REFERENCES (continued)

Hacker, D.S. et al (1961) J. Chem. Phys. 35, 1788-1792

Harteck, P. et al. (1960) Can. J. Chem. 38, 1648

Harteck, P., Reeves, R. (1964) Disc. Faraday Soc. 37, 82

Hartunian, R.A., Thompson, W.P. (1963) AIAA Preprint 63-464

Hayes, W.D , Probstein, R.F. (1958) Applied Mathematics and Mechanics, Vol. 5 Academic Press Inc. New York

Hercules, D.M. (1972) Anal. Chem. 44, 106R

Hildebrand, F.B. (1956) Introduction to Numerical Analysis, McGraw-Hill, New York

Hirschfelder, J.O., Curtiss, C.F., and Bird, R.B. (1954) Molecular Theory of Gases and Liquids, J. Wiley and Sons, New York

Inger, G.R (1966) Int. J. Heat Mass Transfer 9, 755-772

Levin, E.M., Robbins, C.R. and McMurdie, H.F. (1964) Phase Diagrams for Ceramists, American Chemical Scoiety, Columbus, Ohio

Kang, S.W. (1970) AIAA J. 8, 1263-1270

Kang, S.W., Dunn, M.G. (1972) AIAA J. 10, 1361-1362

Kaufman, F. (1958), J. Chem. Phys. 28, 352-353

Kaufman, F. (1961), Progress in Reactions Kinetics, 1, 1-39

Kays, W.M. (1966) Convective Heat and Mass Transfer, McGraw Hill, New York

Kim, K.S., Davis, R.E. (1972) J. Electron Spectrosc. 1, 251

Kistiakowsky, G.B., Volpi, G.G. (1957) J. Chem. Phys. 27, 1141-1149

Krongelb, S., Strandberg, M.W. (1959) J. Chem. Phys. 31, 1196-1210

Lewis, C.H., Burgess, E.G. (1965) AEDC Report TDR 6443, DDC AD 433-958

Li, C.P. (1973) Presented at AIAA 11th Aerospace Sciences Meeting, Washington, D.C. January 10-12

LTV (1971) VMSC Report T143-5R-00044 (Vought Missiles and Space Co.)

LTV (1972) VMSC Report T143-5R-00124 (Vought Missiles and Space Co.)

LTV (1973) VMSC Report T143-5R-30008 (Vought Missiles and Space Co.)

Madey, T.E., Yates J.T.,Jr. (1973) Chem Phys. Lett. 19, 487

Marshall, T.C. (1962) J. Chem. Phys. 37, 2501-2502

Melin, G.A., Madix, R.J. (1971) Trans. Faraday Sco. 67, #585,

Murr, L.E.(1970) Electron Optical Applications in Materials Science, McGraw-Hill Book Company, New York

Park, C. (1964) AIAA J. 2, 1202-1207

Pope, R.B. (1968) AIAA Paper No. 68-15

Prud'homme, R., Lequoy, C. (1969) Office National D'Etudes et de Recherches Aerospatiales, Technical Note No. 147, Chatillon, France

REFERENCES (continued)

Quinn, J.J. (1962) Phy. Rev. 126, 1453

Rosebury, F. (1965) Handbook of Electron Tube and Vacuum Techniques Addison-Wesley, Reading, Mass

Rosner, D.E. (1959) ARS J. 29, 215-216

Rosner, D.E. (1961) ARS J. 31, 1013-1015

Rosner, D.E. (1962a) ASME J. Heat Transfer, 84, #4, 386-394

Rosner, D.E. (1962b) Amer. Rocket Soc. J., 32, 1063-1073

Rosner, D.E. (1963) AIAA J. 1, #7, 1550-1555

Rosner, D.E. (1964a) Proc. 21st AGARD Combustion and Propulsion Panel Meeting, London, 439-483

Rosner, D.E. (1964b) AIAA J. 2, 945-948

Rosner, D.E. (1964c) Proc. Aerophysics of Entry Vehicles Seminar, Session VIII, Report SID 64-2218-8, North American Aviation Corp. Downey, Calif.

Rosner, D.E. (1964d) AIAA J. 2, 593-610

Rosner, D.E., Allendorf, H.D. (1967) J. Electrochem. Soc. 114, 305-314

Rosner, D.E., Allendorf, H.D. (1968) AIAA J. 6, 650-654

Rosner, D.E., Allendorf, H.D. (1970a) J. Phys. Chem. 74, 1829-1839

Rosner, D.E., Allendorf, H.D. (1970b) AIAA J. 8, 166-168

Rosner, D.E. (1972) Combustion Science and Technology (in press); ASME Paper 72 WA/HT-31, Winter Annual Conference, Session on Heat Transfer in Combustion, New York City, November 26-30

Rosner, D.E., Feng, H. (1973) Faraday Transactions I. Physical Chemistry (in press)

Rosner, D.E. "Falsification of Reaction Probability Data Due to Surface Roughness" (to be published)

Scala, S.M. (1958) Proc. 3rd U.S. National Congress of Applied Mechanics, ASME, 779-806

Shiff, H.I., "Neutral Ions Involving Oxygen and Nitrogen" Can. J. Chem. 47 1902 (1969)

Siegbahn, et al. (1967) No. Act. Reg. Soc. Sci. Upsalionsis, Ser. IV, Vol 20

Svehla, R.A. (1962) NASA TR R-132

Tong, H. (1965) AIAA J. 3, 773-774

Teuloukian, Y.S., DeWitt, D.P. (1972) Thermophysical Properties of Matter Vol. 8: Thermal Rediative Properties - Non-Metallic Solids; IFI/Plenum New York

Von Rosenberg D.U. (1969) Methods for the Numerical Solution of Partial Differential Equations, American Elsevier Publishing Comp. Inc. New York

References (continued)

Winkler, E.L. Griffin, R.N. (1961) NASA TN D-1146

Wise, h., Wood, B.J. (1967) Advances in Atomic and Molecular Physics 3, 291-353

Wood, B.J. et al. (1963) J. Phys. Chem. 67, 1462-1465

Youngblood, J.L. (1972) NASA - MSC Internal Communication

8. NOMENCLATURE

A	transverse flow area of duct reactor at prevailing axial station.
$\bar{c}$	mean thermal speed of atoms evaluate at catalyst surface.
$c_{p,b}$	mixture specific heat (per gm.)
$C_{p,i}$	molar heat capacity for chemical species i.
D_i	Fick diffusion coefficient for species i transport
d_{eff}	effective local duct diameter ≡ 4 x (area)/("wetted"perimeter)
F_{Re}	correction to heat transfer for departures from high Reynolds number boundary layer theory; see Section 5.1.
$F_{Dam,i}$	correction factor for finite molecule dissociation kinetics; Eq. (5.1-7)
$f(\ )$	function; Eq. (5.1-22)
f_D	Seider-Tate type function correcting the local mass transport coefficient for transverse property gradients
f_λ	Seider-Tate type function correcting the local heat transfer coefficient for transverse property gradients
f_ν	Seider-Tate type function correcting the local skin friction coefficient for transverse property gradients
$\mathcal{G}_A$	homogeneous sink term in atom mass balance equation; [Eqs.(A2.2-10)]
$\Delta H^{o}_{f,j}$	molar heat of formation of species j
$j''_{A,w}$	diffusion flux of atoms at the wall
$k_{R,j}$	homogeneous (3 body) atomic recombination rate constant (j=0,N)
k_w	heterogeneous recombination rate constant; $\gamma\bar{c}/4$

Le_i	Lewis number for atom i diffusion (i = 0,N); D_i-mix/[$\lambda/(\rho c_p)$]
L	length of one section of the reactor
M	molecular weight (gm/gm-mole)
m	atomic mass, M/N_A
$\dot{m}$	mass flow rate through duct reactor
n	value of $d\ln\tilde{\varepsilon}_w/d\ln T_w$ (see Section 5.3)
N_A	Avogadro's number (6.023 x 10^{23} molec/mole)
Nu	local Nusselt transfer coefficient
p	local static pressure
Pr	prevailing mixture Prandtl number $\frac{\mu_b\ c_{p,b}}{\lambda_b}$
$Q_{\underline{M}^*}$	energy of excited molecule $\underline{M}^*$ above ground electronic state
Q_A	recombination heat per unit mass of recombining atoms (A = 0,N)
$\dot{q}''_w$	energy flux at the wall
$\mathcal{Q}$	dimensionless homogeneous quenching parameter; Eqs.(5.3-6,5.3-7)
R	universal gas constant
Re	Reynolds Number ($U \cdot d_{eff}/\nu_{mix}$) for duct reactor
R_B	body radius of curvature at stagnation point or line
Sc_A	Schmidt number for atom transport, ν/D_{A-mix}
St_h	Stanton number for heat transfer; Eq.(5.1-3)
s*	selectivity for the heterogeneous production of electronically excited molecules per recombination event (cf. Section 5.3)

t_{dissoc}	characteristic dissociation time; Eq.(5.1-13)
t_{flow}	characteristic flow time; Eq.(5.1-13)
T	local gas temperature
U	average gas velocity in duct, or "free stream" velocity relative to vehicle
$\mathcal{W}_i$	dimensionless wall recombination parameter for atoms i ($i = O,N$); Eq. (5.1-5)
$W(\gamma)$	difference between computed and experimental value of $\omega_{A,e}(\gamma)$; Section 2.2
x_j	mole fraction of species j in mixture
z	longitudinal coordinate along the reactor
Z	altitude above sea level

Greek Symbols

μ	dynamic viscosity of gas mixture
σ	Stefan-Boltzmann radiation constant; Eq. (5.1-1)
ξ_D	argument for mass transfer Nusselt number
ξ_λ	argument of the Nusselt number for heat transfer
γ	atom recombination probability
λ	thermal conductivity of mixture
ρ	gas density
ν	mixture kinematic viscosity, μ/ρ
ω_j	species j mass fraction
$\omega_{A,max}$	quantity defined by Eq. (5.1-15)
λ_e	inelastic mean-free-path of emitted photoelectrons
α	angle of attack of Orbiter vehicle

ϵ	total hemispheric emittance of surface; Eq. (5.1-1)
$\rho_{\infty,max}$	quantity defined by Eq.(5.1-16)
δ	diffusion boundary layer thickness
δ_{chem}	chemical sublayer thickness; Eq. (5.3-9)
Δ	shock layer thickness
ϕ	"extent" of heterogeneous atom recombination; Eq.(5.1-4)
Φ	any property (ρ_s, ρ_∞, p_e,...) tabulated as a function of U,Z (cf. Eq. 5.1-8)

Subscripts

au	intermediate station in reactor Section I (see Fig. 2.2-1)
A	pertaining to atoms (either N or O atoms)
BL	pertaining to boundary layer theory; cf. Eq.(5.1-2)
b	"bulk"or "mixing cup average"
comp	computed value
chem	chemical contribution or part
e	outer edge of external boundary layer; Fig. 5.1-1
e	exit of the duct reactor; Fig. 2.2-1
eff	effective (equivalent) value
eq	pertaining to local thermochemical equilibrium (LTE)
exp	experimental value
f	chemically "frozen" (in absence of chemical change)
h	pertaining to heat transfer
i	inlet station of duct reactor (Fig. 2.1-1)
i,j	species index (either Ar , N_2 , N , O or O_2)
mix	pertaining to local gas mixture
wi	window; Eq. 3.1-1
nwi	no window; Eq. 3.1-1
br	brightness (Section 3.1)

max	maximum value (eg. $\Delta h_{chem,max} = \sum(\omega_{i,e} - \omega_{i,w;eq}) \cdot Q_i\{T_w\})$
q	pertaining to the quenching of excited molecules
s	immediately downstream of the normal shock wave
w	evaluated at the wall (gas/solid interface)
Z,U,ZU, etc.	partial derivative with respect to Z,U,Z and U etc., Eq. (5.1-8)
∞	at upstream infinity (with respect to body)
2,3	for homogeneous reactions 5.3-2 and 5.3-3, respectively
I,II,III	pertaining, respectively, to reactor Sections I,II, III

Superscripts

(r)	r^{th} approximation (r = 0,1,....)
0	evaluated in the ideal gas (Lim p → 0) state
1,2	pertaining to first and second "levels" of approximation to γ (written ${}^1\gamma$,${}^2\gamma$); see Section 2.2

Miscellaneous

$\Delta(\ )$	"change in" operator
${}^1\Sigma_g^+, {}^3\Sigma_u^+$	spectroscopic designations for electronically excited states of the O_2 molecule
6(1)26	from 6 to 26 in increments of 1, etc. (see Section 5.1.1)
TPS	thermal protection system
LTE	local thermochemical equilibrium
RPP	reinforced pyrolyzed plastic material (nose cap, wing leading edge)
RSI	re-usable surface insulation material
QPR	quarterly progress report (Contract NAS 9-13058)
ESCA	electron spectroscopy for chemical analysis (see XPS below)
LTV	Ling Temco Vought Aerospace Corporation
SEM	scanning electron microscope
XPS	X-ray photoelectron spectroscopy

(g)	gas
(s)	solid
(c)	condensed (liquid or solid)
(N),(O)	concentrations (number densities) of N, O; Section 2.1
pct	percent
1.18(-4)	1.18×10^{-4} (etc.)
$(\;)''$	per unit area
$(\;)'''$	per unit volume
3-dim	3 dimensional (axisymmetric)
2-dim	2 dimensional
A1,A2,..	Assumptions 1, 2, ...

Appendix 2.2 DETAILS OF DUCT REACTOR DATA REDUCTION PROCEDURE

This appendix includes explicit expressions for the individual terms appearing in the quasi-one dimensional duct reactor analysis outlined in Section 2.2.

For constant property Poiseuille flow through a straight circular duct of diameter d with constant wall temperature T_w for $z \geq 0$ the local heat flux at the duct wall is given by:

$$-\dot{q}''_w = \frac{\lambda}{d} \cdot \mathrm{Nu}(\xi_\lambda) \cdot [T_w - T_b(z)] \qquad \text{(A2.2-1)}$$

where

$$\xi_\lambda \equiv \frac{2}{\mathrm{Pr} \cdot \mathrm{Re}} \cdot \frac{z}{d} \qquad \text{(A2.2-2)}$$

The local Nusselt number $\mathrm{Nu}(\xi)$ appearing in Eq. (A2.2-1) is expressible in the form of an infinite series [Kays(1966)]. For variable property flow in our non-circular duct reactor the local heat flux is therefore approximated by:

$$-\dot{q}''_w = f_\lambda \cdot \frac{\lambda_b}{d_{eff}} \cdot \mathrm{Nu}(\xi_\lambda) \cdot [T_w - T_b(z)] \qquad \text{(A2.2-3)}$$

where $f_\lambda(T_w/T_b)$ is a variable property correction factor of the Seider-Tate type and

$$\xi_\lambda \equiv \frac{2}{\mathrm{Pr} \cdot \mathrm{Re}} \cdot \frac{(z-z_{au})}{d_{eff}} \quad \text{for} \quad z_{au} \leq z < z_u \qquad \text{(A2.2-4a)}$$

$$\xi_\lambda \equiv \frac{2}{\mathrm{Pr} \cdot \mathrm{Re}} \cdot \frac{(z-z_u)}{d_{eff}} \quad \text{for} \quad z_u \leq z < z_d \qquad \text{(A2.2-4b)}$$

$$\xi_\lambda \equiv \frac{2}{\mathrm{Pr} \cdot \mathrm{Re}} \cdot \frac{(z-z_d)}{d_{eff}} \quad \text{for} \quad z \geq z_d \qquad \text{(A2.2-4c)}$$

where the stations z_{au}, z_u and z_d are defined in Fig. 2.2-1. Of course $T_w(z)$ must be specified, especially outside reactor region II (where T_w is <u>measured</u>). For this purpose it was assumed[†] that T_w is at room temperature in the water cooled quartz section (cf. Fig. 2.1-1) and rises linearly in the uncooled quartz section to value half-way between $(T_w)_{II}$ and that of the water cooled section (cf. Fig. 2.2-1).

Similar expressions must be used for atom mass transfer to the walls, however, the situation for $j''_{A,w}$ is less direct since $\omega_{A,w}$ is not known. <u>a priori</u>, but is determined by a local balance between transverse atom diffusion and surface reaction [Rosner (1964d)]. This local transverse atom balance equation may be written:

$$f_D\left(\frac{T_w}{T_b}\right) Nu(\xi_D)\ (D_A \cdot \rho_b)\frac{\omega_{A,b} - \omega_{A,w}}{d_{eff}} = k_w(T_w)\rho_w\omega_{A,w} \qquad \text{(A2.2-5)}$$

where:

$$\xi_D \equiv \frac{2}{Sc \cdot Re} \cdot \frac{(z-z_u)}{d_{eff}} \equiv \frac{2(z-z_u) \cdot (D_A\rho)_b}{\dot{m}} \qquad \text{(A2.2-6)}$$

$$k_w(T_w) \equiv \frac{\gamma}{4} \cdot \left(\frac{8RT_w}{\pi M_A}\right)^{1/2} \qquad \text{(A2.2-7)}$$

$$\rho_w \equiv \frac{pM_w}{RT_w} \qquad \text{(A2.2-8)}$$

When Eq.(A2.2-5) is solved for $\omega_{A,w}$ we find:

$$j''_{A,w} = \frac{f_D Nu(\xi_D)(D_A\rho)_b\omega_{A,b}}{d_{eff}} \cdot \left[\frac{\dfrac{k_w\rho_w d_{eff}}{f_D(D_A\rho)_b \cdot Nu(\xi_D)}}{1 + \dfrac{k_w\rho_w d_{eff}}{f_D(D_A\rho)_b \cdot Nu(\xi_D)}}\right] \qquad \text{(A2.2-9)}$$

[†] Owing to the catalytic activity of quartz at these temperatures, our inferred γ-values for Section II can be sensitive to the value chosen for the peak quartz temperature. However, parametric studies indicate that this could at most account for about a factor of 2 in our present γ_i-estimates for the RPP material.

Since $\omega_{A,w}$ appears implicitly in ρ_w via the mean molecular weight of the gas mixture at the wall, an iterative solution of Eq.(A2.2-5) is, in general, necessary. Values of the correction factors f_ν, f_λ, f_D were estimated from "calibration" runs in which the exit pressure and bulk gas temperature were measured and compared with computed (predicted) values. These led, respectively, to $f_\nu = (T_w/T_b)^{2.65}$ and $f_\lambda = 1.0$. All ${}^2\gamma$ values reported herein were based upon these factors, together with the assumption $f_D = 1.0$.

For a three-body reaction the gas-phase recombination term $\mathcal{G}_A$ is given by:

$$\mathcal{G}_A = \begin{cases} \dfrac{k_{R,O}(T_b)\rho_b^{3}\ \omega_{O,b}\ \ \omega_{O_2b}}{m_{O_2} \cdot m_b} & \text{for O-atoms}^{+} \qquad \text{(A2.2-10a)} \\[2ex] \dfrac{k_{RN}(T_b)\rho_b^{3}\ \omega_{N,b}^{2}}{m_N \cdot m_b} & \text{for N-atoms} \qquad \text{(A2.2-10b)} \end{cases}$$

The homogeneous (3 body) recombination rate constants $k_{R,O}$ and $k_{R,N}$ appearing in Eq.(2.2-10) have been taken to be 0.817×10^{-33} and 1.49×10^{-32} cm^6 x molec^{-2} x sec^{-1}, respectively, within the reactor temperature range of interest [Schiff (1969)].

The corresponding energy release to the gas mixture Q_A''' is merely given by the product $\mathcal{G}_A Q_A$, where the Q_A ($A = O,N$) are the heats of recombination per unit mass.

[+] The appearance of only the first power of $\omega_{O,b}$, and the O_2 concentration in Eq. (A2.2-10a) reflects the predominance of the O_3-mechanism for O-atom recombination under these conditions [Kaufman, (1961)].

APPENDIX 2.3. ON THE USE OF Al_2O_3 ADDITIONS TO RPP COATINGS

Inasmuch as our recombination results and the comparison of RPP mass loss rates with those for pure dense pyrolytic SiC (Rosner and Allendorf, 1970a) indicate that the presence of Al_2O_3 in the RPP coating may enhance recombination and oxidation reactions we examined the evidence [LTV(1972)] that led to the decision to use Al_2O_3 in the RPP coating. Since we have not found a summary of this evidence, our summary of the data is given below.

The relevant data concerning the use of Al_2O_3 in RPP coatings are given in Sec. 4.3 and the appendix of LTV(1972). The basis for choice of a "best" coating system is stated (p. 144) to be that "tested specimens indicated acceptable low temperature oxidation resistance, good strength and plasma arc performance, and a projected ease of fabrication". Avoidance of crazing phenomena and cool down cracks during fabrication was also significant in choosing between different coating procedures although (p. 171) "The effect of crazing on system performance has not yet been proven detrimental since crazed parts have performed well in plasma arc test and air furnace test and have good flexure strength."

The quantitative results that bear on the choice of the $10Al_2O_3$ 60SiC, 30Si pack composition in the diffusion coating runs were test results from diffusion furnace runs M85B, M88, M95, M96, and M97 (p. 143). We have summarized these results in Figs. A2.3-1, -2, and -3. Figure A2.3-1 plots all the arc jet test results for the above samples versus temperature and also presents the correlation curve for the final arc jet results on the 10/60/30 material [LTV(1972), p. A63-64]. No significant difference is observed between the results for any of the pack formulas and the final 10/60/30 material. However, most of the 10/60/30 specimens achieved slightly lower temperatures* in the arc jet tests and therefore appear superior if one assumes that arc jet experiments faithfully reproduce the re-entry environment.

Flexure strength data from expts M95, M96 and M97 are presented as strength <u>vs</u> specimen percent weight gain during coating in Fig. A2.3-2. It is clear from this plot that strength decreases with weight gain during coating and with the temperature of the coating process but is not related to the composition of the pack.

Pereny furnace test data which measure weight loss during air exposure at 2300°F are plotted in Fig. A2.3-3 as percent weight change in the furnace test <u>versus</u> percent weight gain during the coating process. Again, pack composition is not significant. In Fig. A2.3-3 the bands for data on the 10/60/30 coating [LTV (1972), p.162] are shown.

Thus it appears that Al_2O_3 containing packs for the diffusion coating process produce coatings with equal arc jet, Pereny furnace, or strength performance to ~~[illegible]~~ coatings formed in the absence of Al_2O_3. The main reason for the choice of Al_2O_3 containing packs for the diffusion coating process is perhaps historical as evidenced by the statement (p. 141) "This good performance (in Phase I plasma arc tests) was in part due to the aluminum oxide content added in slurry form to the surface of the RPP prior to packing in a mix of silicon and silicon carbide. Specimens fabriacted without aluminum oxide did not perform as well." Also the statement on p. 148 "The 10% Al_2O_3 mix sinters and shrinks at a more predictable rate under the test conditions although at 3400°F an over-sintered condition prevailed" appears to be significant. Nevertheless the qualitative comparison of pack results containing different amounts of Al_2O_3 (p. 145-147) does not seem to favor the $10Al_2O_3$, 60SiC, 30Si composition over the $1Al_2O_3$, 69SiC, 30Si composition.

---

* The good correlation between weight loss and temperature indicates that no significant spectral emissivity differences exist for the different coatings.

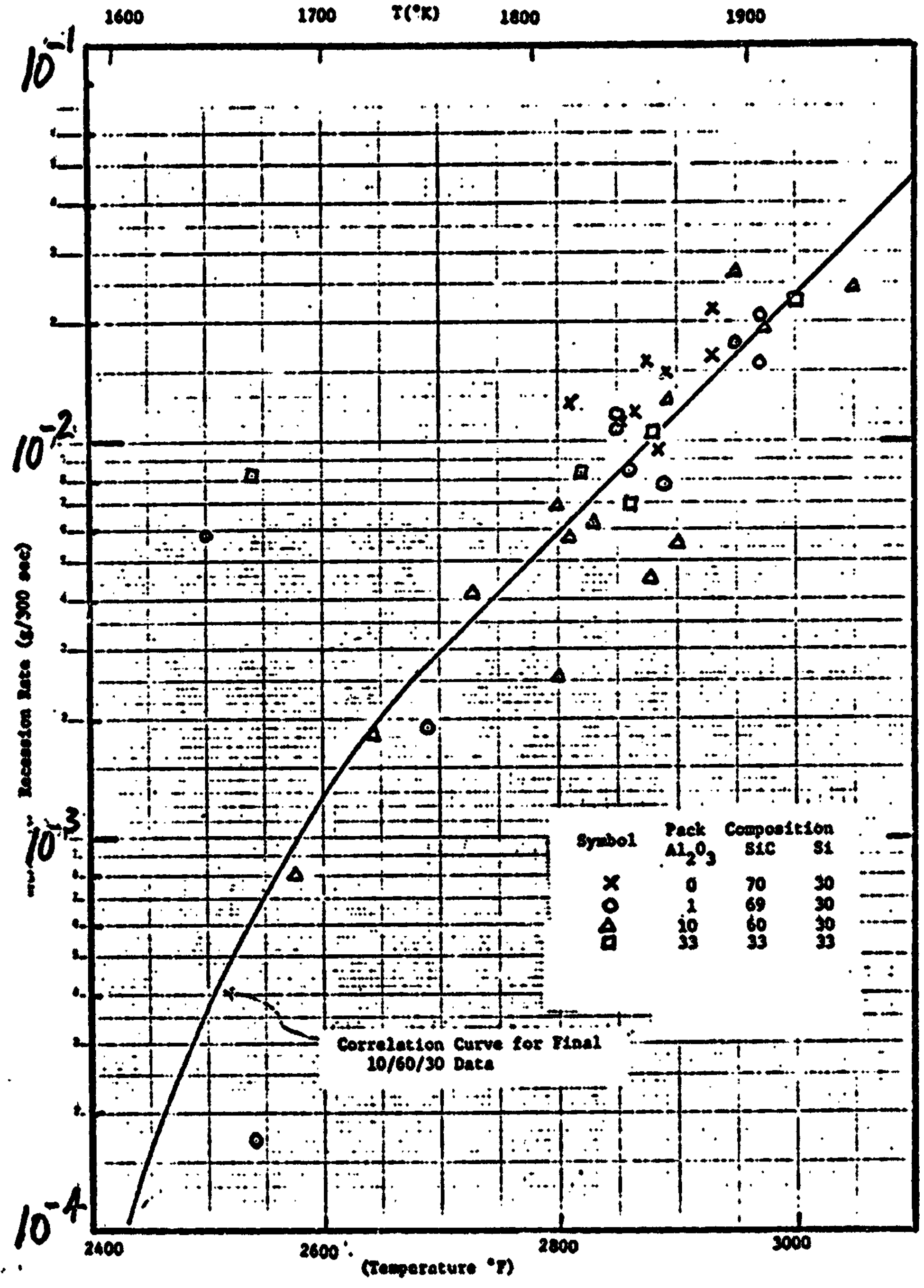

Fig. A2.3-1 Arc jet weight loss rates for various RPP coatings versus temperature

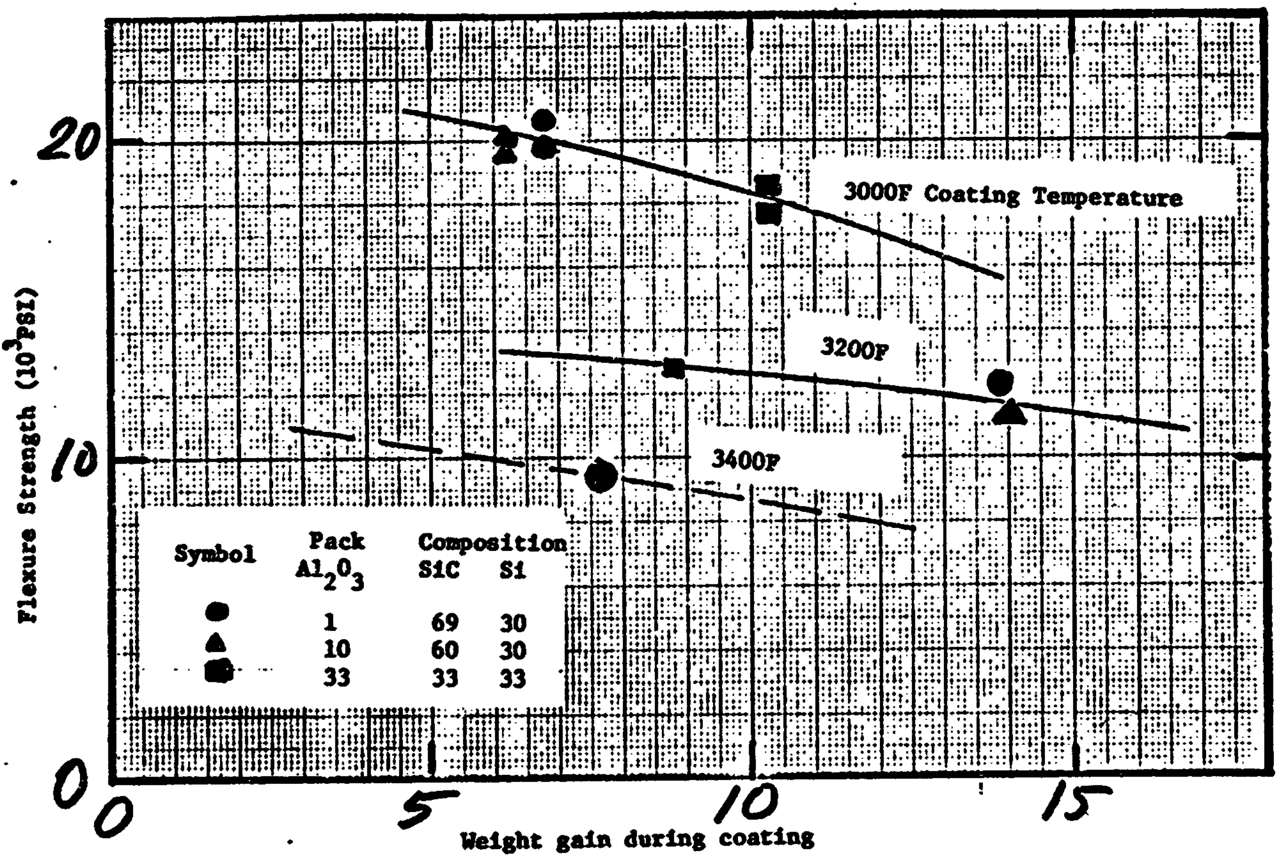

Fig. A2.3-2 Flexure strength versus weight gain during coating for various RPP coatings

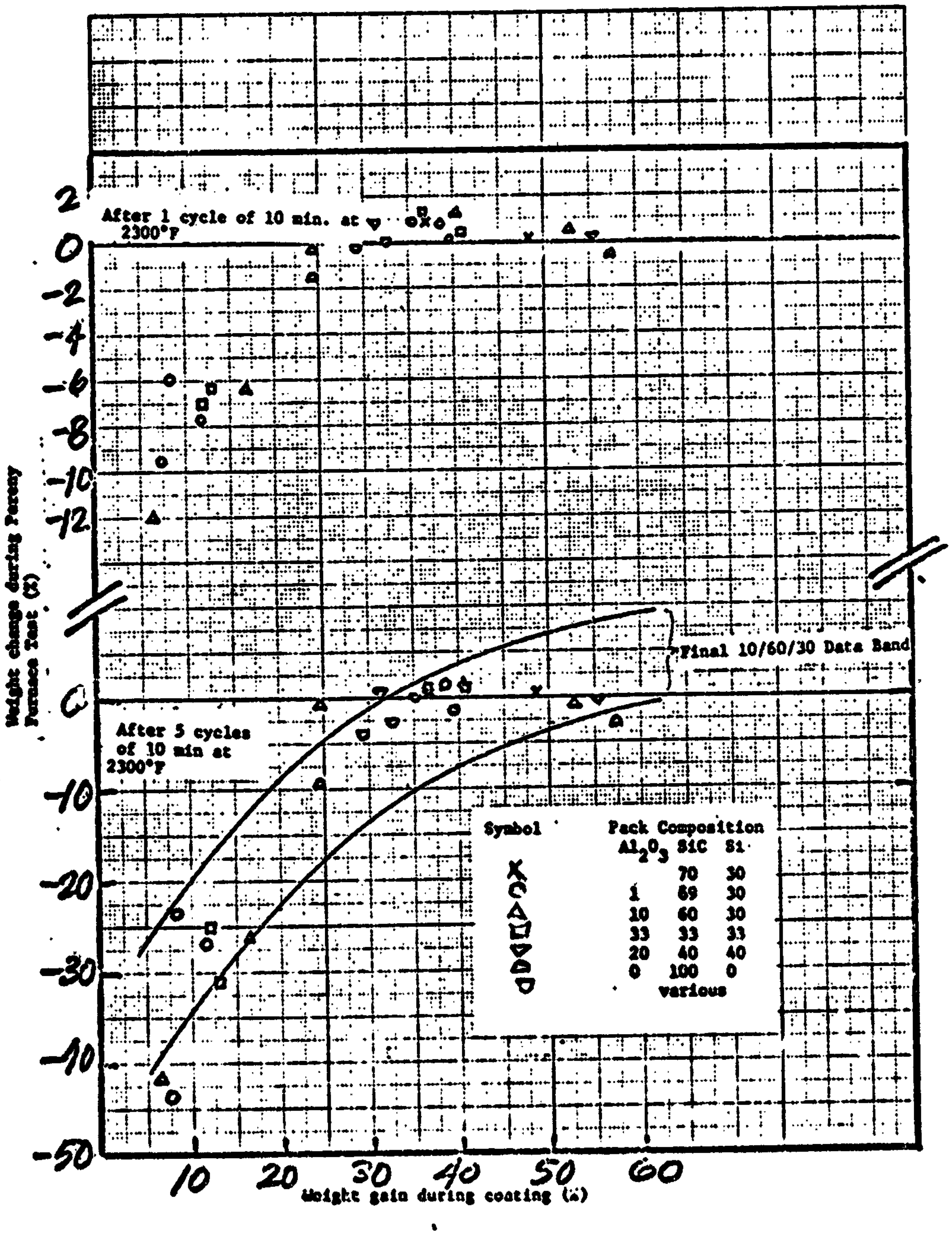

Fig. A2.3-3 Weight loss in Pereny furnace test versus weight gain during coating process for various RPP coatings.

APPENDIX 5.1 CONVERSION OF γ_i TO RECOMBINATION RATE CONSTANT ("VELOCITY")

Since all aerodynamic heating predictions involve the group

$$k_{w,i} \equiv \frac{1}{4} \cdot \left(\frac{8kT}{\pi M_i}\right)^{1/2} \cdot \gamma_i$$

it is useful to be able to rapidly convert from the dimensionless recombination probability $\gamma_i(T_w)$ to the corresponding recombination rate constant or "velocity" (expressed, say, in cm/sec). For this reason Table A5.1-1 is provided, giving the numerical value of the ratio[+] $10^{-4}\, k_{w,i}/\gamma_i$ for O atoms and N atoms in the temperature range 1000(100)2500K:

Table A5.1-1

Values of $10^{-4}\, k_w/\gamma$ for O and N-atom Recombination[a]

T_w(K)	Oxygen	Nitrogen
1000	2.8759	3.0737
1100	3.0163	3.2237
1200	3.1504	3.3670
1300	3.2790	3.5045
1400	3.4028	3.6368
1500	3.5222	3.7644
1600	3.6377	3.8879
1700	3.7497	4.0076
1800	3.8584	4.1237
1900	3.9641	4.2367
2000	4.0671	4.3468
2100	4.1675	4.4541
2200	4.2656	4.5590
2300	4.3615	4.6614
2400	4.4553	4.7617
2500	4.5472	4.8599

[+] the value of $k_{w,i}/\gamma_i$ may be identified with the maximum possible reaction velocity for atom recombination at the prevailing surface temperature.

[a] expressed in cm. sec^{-1}

☆ U.S. GOVERNMENT PRINTING OFFICE: 1973—778-210/1077